STUDY OF SPONTANEOUS FISSION OF ^{252}CF: STRUCTURE OF NEUTRON-RICH NUCLEI, GAMMA-RAY ANGULAR CORRELATION AND G-FACTOR MEASUREMENTS

By

Ke Li

Dissertation

Submitted to the Faculty of

the Graduate School of Vanderbilt University

in partial fulfillment of the requirements

for the degree of

DOCTOR OF PHILOSOPHY

in

Physics

May, 2008

Nashville, Tennessee

Approved:

Joseph H. Hamilton

Akunuri V. Ramayya

Charles F. Maguire

Ronald R. Price

Sait A. Umar

To my wife

Zhige Meng

ACKNOWLEDGEMENTS

First of all, I would like to acknowledge the wonderful environment provided by the Department of Physics and Astronomy, Vanderbilt University for making the time I spent in Vanderbilt a stimulating, enjoyable and memorable experience. This thesis would not have been possible without the invaluable assistance and support of my advisors, Professors Joseph Hamilton and Akunuri Ramayya. Being always patient and supportive, they guided me through this journey for the past five years. The rest of my committee members, Dr. Umar, Dr. Maguire and Dr. Price, have my deepest thanks for their encouragement and support.

Thanks must be extended to Dr. J.K. Hwang, Dr. A.V. Daniel, Dr. Y.X. Luo, Prof. S.J. Zhu, and Dr. N. J. Stone for providing very experienced and enthusiastic advice on my research. Also, I'd like to thank Carol Soren for providing a lot of assistance helping me get through my studies. During my graduate studies, I was able to spend part of my time at Oak Ridge National Laboratory to gain hands-on experience. I want to thank Dr. K. Rykaczewski for helping me with this. Other people at ORNL who were very helpful to me were J. Batchelder, R. Grzywacz, C. Mazzocchi among many others. Chris Goodin, has been a great friend, and I enjoyed the time we spent together on research.

Special thanks are due to my parents and brothers for their strong support and encouragement. Most importantly, my lovely wife, Zhige Meng has always been supportive. None of this could have been possible without all of them.

The work at Vanderbilt was supported in part by the U.S. Department of Energy under Grant No. DE-FG05-88ER40407. The Joint Institute for Heavy Ion Research at ORNL is supported by the University of Tennessee, Vanderbilt University, ORNL, and the U.S. DOE under Contract No. DE-FG05-87ER40311.

TABLE OF CONTENTS

LIST OF TABLES

LIST OF FIGURES

CHAPTER I

INTRODUCTION

With the development of more sophisticated facilities and experimental techniques, the research of nuclear structure have been moving towards more and more exotic regions, with a great excess of protons or neutrons than found in the stable isotopes. Today, around 115 different species of nuclei have been identified. Figure 1 shows all the known nuclei arranged according to their proton number Z and neutron number N. Most of the stable nuclei have unequal Z and N and exhibit a significant neutron excess, in order to compensate for the repulsive trend caused by the positive charges of the protons. Properties of nuclei can vary enormously from nucleus to nucleus. A special character, known as "Magic Numbers", is exhibited by nuclei with certain number of protons and neutrons.

For the study of neutron-rich nuclei, it is hard to produce them by using normal heavy-ion reactions. One practical method is to study the fission of heavy elements, such as induced fission or spontaneous fission. In a fission process, a heavy nucleus breaks apart, produces nuclei with much higher ratios of neutrons to protons than the stable isotopes in that mass region. Thus, studies of nuclei produced from fission provide a major source of information on the structure of neutron-rich nuclei. In this dissertation, experimental data from the spontaneous fission of ^{252}Cf will be investigated.

Spontaneous Fission of ^{252}Cf

Spontaneous fission is a process in which a single heavy nucleus splits into two or more smaller fragments without any external influence. The process occurs mainly in heavy nuclei and is the direct result of competition between the attractive nuclear force, which holds nucleons in the nuclei, and the Coulomb repulsion which drive the protons apart. For light nuclei, the strong nuclear force is easily able to overcome the Coulomb

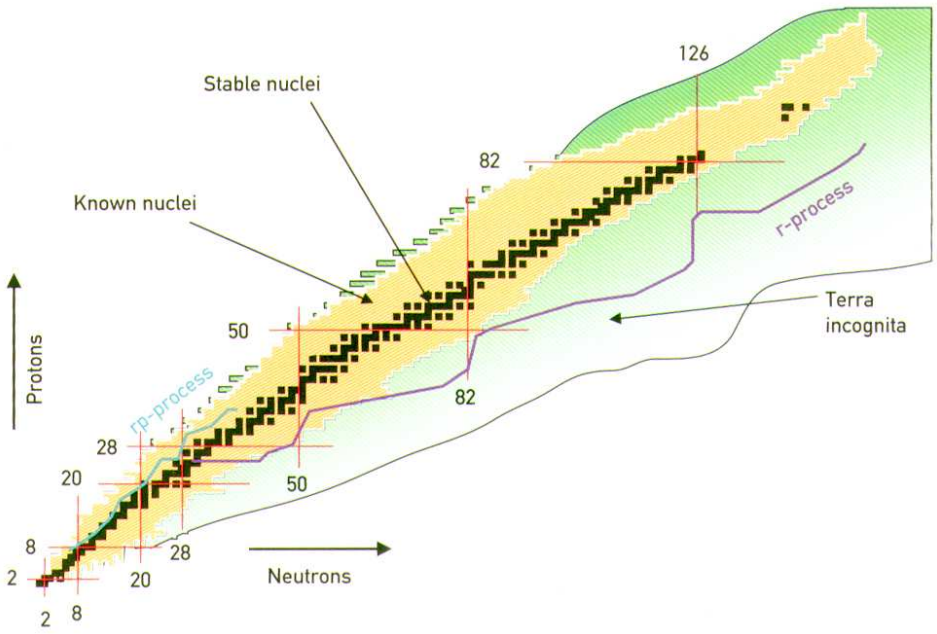

Figure 1: Nuclear landscape. Magic shell closures are highlighted in red. The green region is enclosed by proton and neutron drop lines. The yellow ones are known nuclei, while black dots are stable nuclei.

force. However, since the Coulomb force is repulsive, with more and more protons inside, the nucleus becomes more instable.

The energy to hold a $^{252}_{98}$Cf nucleus together, the *binding energy*, is approximately the difference between the measured mass of ^{252}Cf and the total mass of 98 protons and 154 neutrons, which is approximately 1800 MeV. The binary fission of ^{252}Cf is able to liberate $\sim$200 MeV of nuclear energy and is therefore an energetically feasible means of de-excitation. Despite spontaneous fission, α decay is the predominately-favored decay mechanism for most heavy nuclei. The α decay process liberates $\approx$ 6 MeV of internal energy. Alpha decay is favored because the Coulomb barrier opposing the binary fission of ^{252}Cf into two ^{126}In nuclei is around

$$V(SF) = \frac{1}{4\pi\epsilon_0}\frac{Z_1 Z_2 e^2}{(R_1 + R_2)} \approx 275 MeV \tag{1}$$

assuming that the nuclear radius $R = 1.25A^{1/3}$ fm, whereas the Coulomb barrier for the

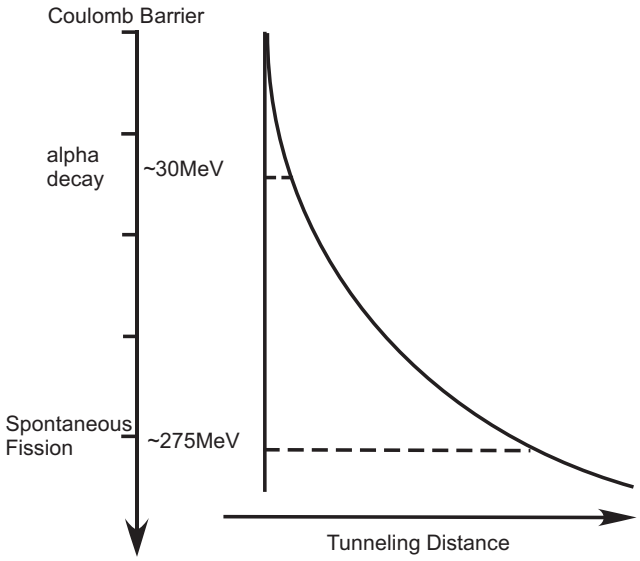

Figure 2: Relative, potential-energy barrier widths for the processes of spontaneous fission and α decay in ^{252}Cf.

production of an α particle and a ^{248}Cm nucleus is

$$V(\alpha) \approx 35MeV. \tag{2}$$

as shown in Figure 2. The preference for α decay over spontaneous fission manifests itself in the fact that the half-life for α decay of ^{252}Cf into ^{248}Cm is measured to be $\tau_{1/2}(\alpha)$ =2.645(8) yrs while the half-life for spontaneous fission is $\tau_{1/2}(SF)$ =82.89(33) yrs.

Right after the splitting of the parent nucleus, the primary fission fragments evaporate some number of neutrons, on the average of four for spontaneous fission of ^{252}Cf [TA97]. These secondary fragments are usually in very excited states and promptly emit γ-rays. The first two stages occur very quickly, with most neutrons evaporated in 10^{-20} to 10^{-15} seconds. When neutron emission becomes energetically impossible, the process of γ-ray decay takes over. At this stage, the fragments are referred to as secondary fragments and the γ rays which they emit are known as prompt γ rays. The emission of these prompt γ-rays eventually leads to a ground-state whose lifetime ($\sim$ second) is far greater than the time-scale of the fission process and is relatively considered to be stable. The radioactive

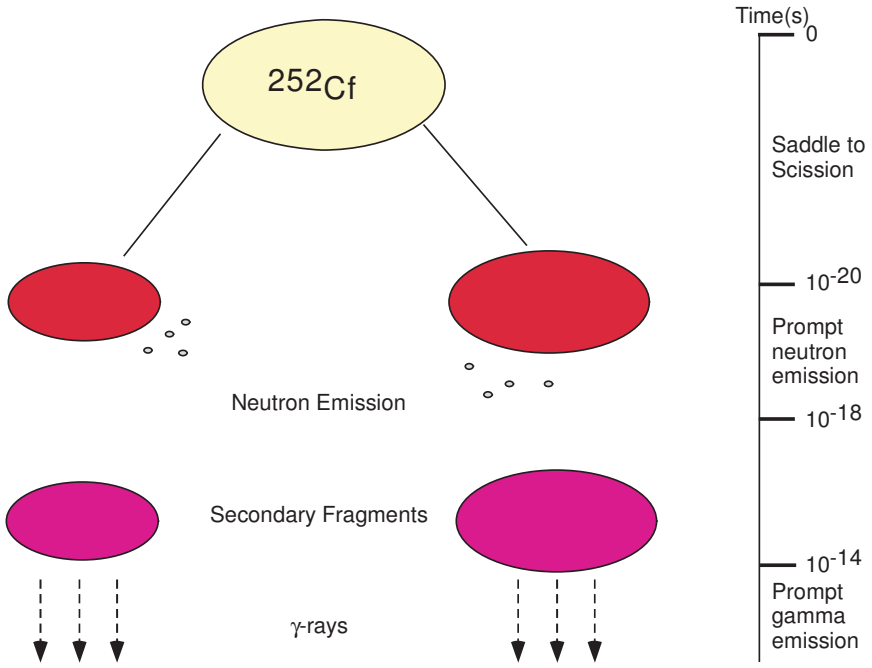

Figure 3: Spontaneous fission scheme of ^{252}Cf

secondary fragments subsequently undergo a series of β decays and these continue until the fragments transform themselves into more stable nuclei. A schematic of timescale in the spontaneous fission of ^{252}Cf is shown in Figure 3.

The production region of spontaneous fission consists of two distinct areas either side of the exceptional stable doubly-magic ^{132}Sn nucleus, as shown in Figure 4. Each binary fission event of ^{252}Cf therefore yield complimentary pairs of one heavy and one light fragment. Since individual protons are not emitted as fission fragments, the same pairs of isotopes are always produced together: $_{40}$Zr with $_{58}$Ce, $_{42}$Mo with $_{56}$Ba, $_{44}$Ru with $_{54}$Xe etc. Consequently, γ-rays emitted from each pair will be in coincidence with each other. As an example, Figure 5 shows a γ spectrum produced from one of our experiments on spontaneous fission of ^{252}Cf. The spectrum shows all γ rays recorded in coincidence with the two lowest energy (highest intensity) transitions in ^{102}Zr. As well as other transitions in ^{102}Zr, the spectrum exhibits γ rays from a wide range of fission fragments that are coincident with γ rays in ^{102}Zr. Studies of spontaneous fission have shown that the neutron

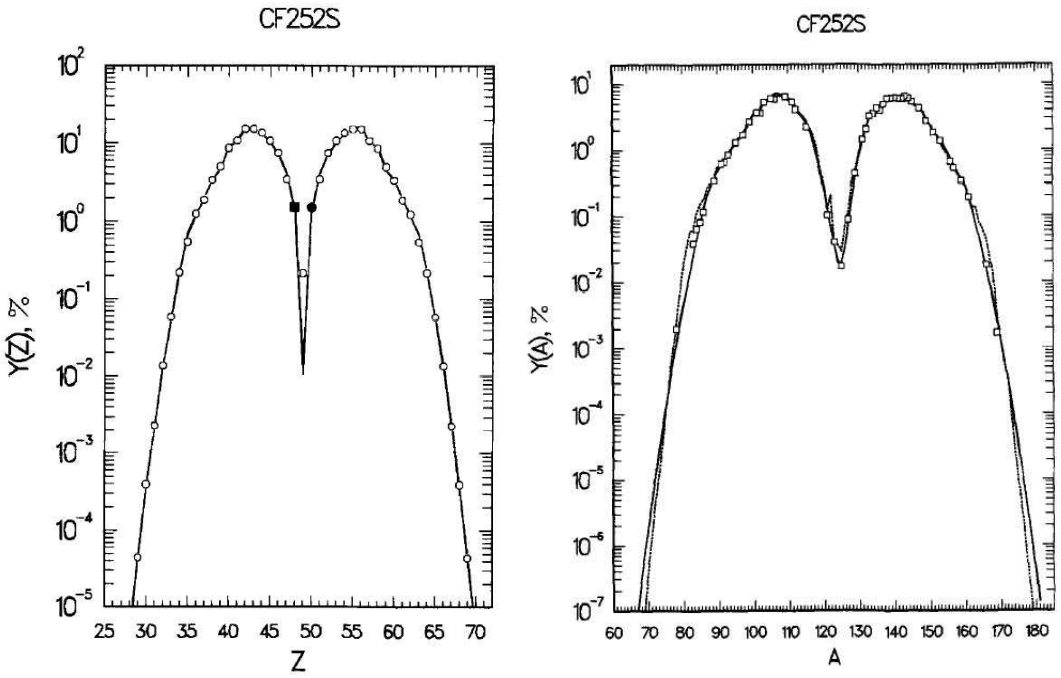

Figure 4: The relative yields of secondary fragments from the spontaneous fission of ^{252}Cf as a function of proton number Z and mass number A [Wah88].

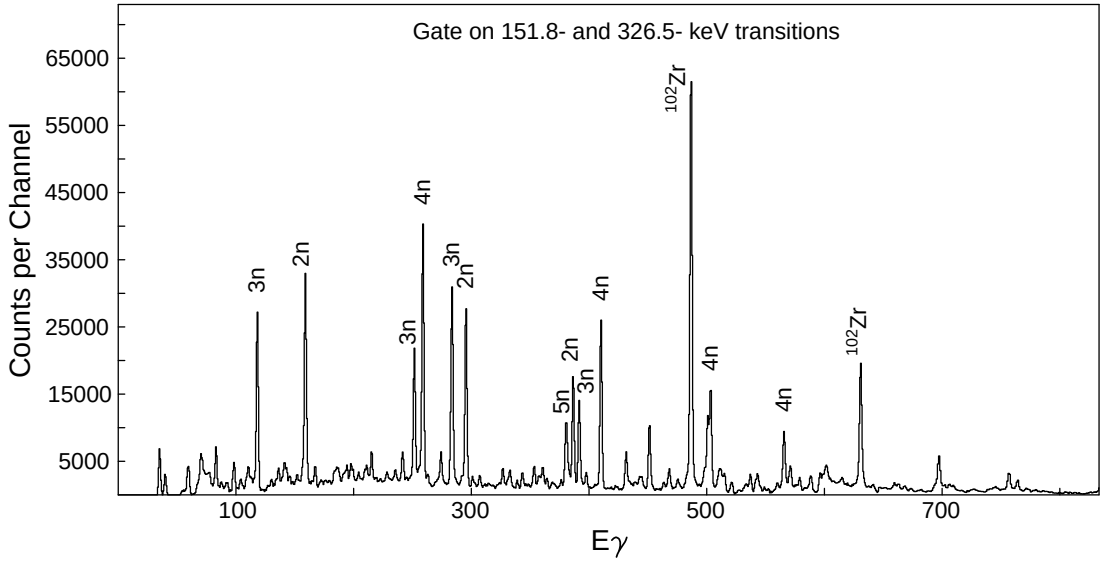

Figure 5: Spectrum produced from double-gating on 151.8- and 326.5-keV transitions in ^{102}Zr. Transitions are labeled by their neutron multiplicities for ^{102}Zr corresponding to the complementary fission fragments.

multiplicities could range from 0 (cold fission) to as high as 10 [TA97]. Other possibilities include ternary fission (0.38% of all spontaneous fission events) in which the parent nucleus splits into three particles [Fon06] [Goo06].

The disadvantage of using a spontaneous fission source is that many nuclei (> 100) are populated. Each of the 100 fragments can emit up to 100 γ-rays to give us overlapping energy signals that can obscure the signatures of any nucleus of interest. With the proper experimental facilities and data analysis techniques, we can sort the signals to identify the nuclei of interest. At the emergence of the first phase of the Gammasphere detector array, our 1995 experiment was performed [Ham95]. Five years later, with the second phase of the Gammasphere, our 2000 experimental run was performed, with 15 times more events collected [Luo01]. Also, with the new data set and a less compressed cube created, much information has been discovered. In this dissertation, some new results will be presented on the study of neutron-rich nuclei.

Nuclear Magnetic Moment

A single, static electric charge creates a static electric field in the space around it. Similarly, a moving electric charge creates a magnetic field and the magnetic properties of such a charge can be represented by a quantity referred to as the magnetic dipole moment, μ. This rule applies to the nucleus where the magnetic effects can be considered as having origins in both the orbital motion of charged particles as well as in the intrinsic spin that all nucleons possess. In the classical representation, a single charge, *e*, of mass *m*, orbiting at velocity of *v* in a uniform circle of radius *r* has a magnetic dipole moment given by

$$\mu = \frac{e}{2m}\boldsymbol{l} \tag{3}$$

where $\boldsymbol{l} = m\boldsymbol{v} \times \boldsymbol{r}$ is the classical angular momentum.

For protons and neutrons moving in nuclei, quantum mechanical considerations must be taken into account. First, the angular momentum is defined to be the expectation

value corresponding to the direction in which *l* has maximum projection (+*lh*). Second, it is necessary to include an additional term for the intrinsic spin magnetic moment, *s*, which each nucleon possesses. This intrinsic moment is due to the intrinsic spin of the particle. The expression for the magnetic moment becomes

$$\mu = (g_l l + g_s s)\frac{\mu_N}{\hbar} \tag{4}$$

where the proton mass, m_p, is used to define the nuclear magneton,

$$\mu_N = \frac{e\hbar}{2m_p} = 3.15245 \times 10^{-8} eV/T \tag{5}$$

The orbital and intrinsic-spin g-factors, g_l and g_s, are dimensionless quantities which quantify the extent of orbital and intrinsic contributions to the magnetic moment. The measured values of g_s for free protons (π) and neutrons (ν) are

$$\begin{aligned} g_s(\pi) &= +5.5856912(22) \\ g_s(\nu) &= -3.8260837(18) \end{aligned} \tag{6}$$

respectively. The difference from expected values of $g_s(\pi) = +2$ and $g_s(\nu) = 0$ is taken as a proof that neither protons nor neutrons are elementary particles.

Therefore, for a nucleus composed of $A = Z + N$ nucleons, any arbitrary state with a "spin" quantum number, I has a net angular momentum contributed from orbital and intrinsic of all the nucleons in the system. The spin, I, is defined as

$$I = \sum_{i=1}^{A} (l_i + s_i). \tag{7}$$

Hence, the magnetic moment of the state is the sum over all nucleons:

$$\mu = \sum_{i=1}^{A} (g_{l_i} l_i + g_{s_i} s_i)\frac{\mu_N}{\hbar}. \tag{8}$$

Equation 8 cannot be solved analytically for any arbitrary excited state in any arbitrary nucleus. Interactions between nucleons depend strongly on relative spin orientations. Therefore, individual intrinsic spins and orbital momenta are not constant but can take

on any values that are compatible with the overall spin, I. The solution of Equation 8 is no more than an estimate made using the most appropriate nuclear model/models for the specific nucleus under consideration.

The measurement of excited-state g-factors has long been of experimental significance, as they play an important role in the understanding of nuclear structure. Experimental g-factor measurements are used to verify the validity and suitability of various nuclear models. A wide variety of experimental techniques have been developed to measure excited-state g-factors. Most methods are accelerator-based and involve the use of a beam to produce excited states, implantation of products into a hyperfine magnetic field, and measurements of perturbed angular correlations. Measurements involving the use of fission fragments can be found, such as in [Smi99] and [Pat02], where g-factor measurements were made by put spontaneously fissioning source between ferromagnetic materials with an externally applied magnetic field.

The motivation for us to measure excited-state g-factors is a new technique to measure angular correlations perturbed by randomly oriented hyperfine fields [Dan07], by analyzing a high statistical dataset from our 2000 binary fission experiment with the Gammasphere array. The Gammasphere array has 110 Germanium detectors at full capacity and they cover 4π angle around the reaction chamber, and provides a large number (5995) of detector pairs, falling into 64 discrete angle bins, for us to perform angular correlation measurements. In our experiment, the spontaneously fissioning ^{252}Cf source was sandwiched between two iron (Fe) foils. Therefore, angular correlations of delayed γ-ray cascades were perturbed by the randomly-oriented hyperfine magnetic fields in the Fe foils. The perturbation is reflected in the attenuation of angular correlation coefficients, which are related to the lifetimes and g-factors of the intermediate states. While for prompt cascades, the perturbation effects are negligible, which enabled us to extract information on the spins and parities of the energy levels and the multipole mixing ratios of the transitions.

CHAPTER II

EXPERIMENTAL TECHNIQUES

The fission experiments described in this dissertation utilized one of the most advanced experimental nuclear facilities, Gammasphere, which has high energy resolutions and efficiencies and enables us to probe more exotic nuclei and discover more detailed information. Triple coincident technique has been developed and is the key to increase our ability to identify weak transitions in the nuclei of interest. In this chapter, we will introduce γ-ray detection techniques, and the Gammasphere array. The triple coincident technique will be detailed. The details of several fission experiments will be presented as well.

Gamma-Ray Detection systems

Gamma-ray Detection Principles

Generally, two physical processes lie behind most γ-ray detection devices. One process is the interaction between the incident γ-ray radiation and the atoms of the detecting material, which free a large number of atomic electrons from their orbits. The other process is the collection of the liberated charges and transformation into a measurable electrical voltage with a magnitude proportional to the incident γ-ray energy.

Therefore, such a detector device must satisfy two criteria: the detective material must be able to withstand a sufficiently-large-enough electric field to gather the radiation-liberated electrons without collecting random thermal electrons present in the sample, and at the same time, the material must also be capable of allowing the incident radiation to liberate large numbers of atomic electron and to allow these liberated electrons to travel freely so that they may be counted. The first criterion clearly suggests insulating material

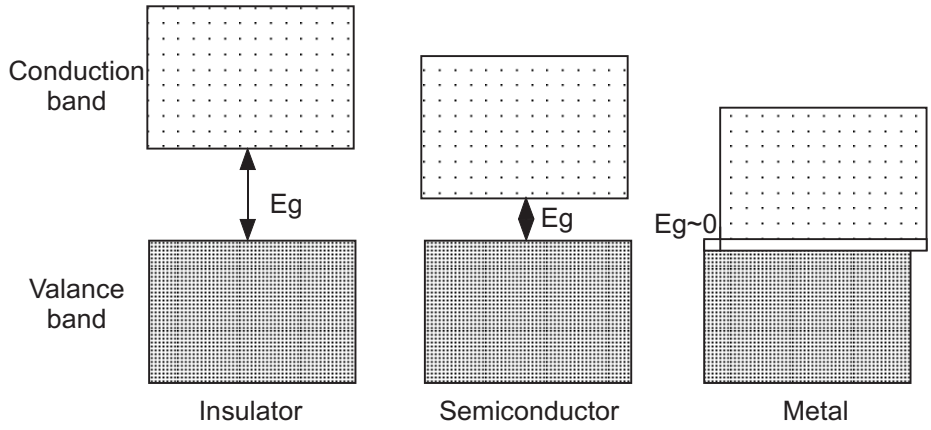

Figure 6: Schematic band diagrams for an insulator, a semiconductor, and a metal.

and the second seems to support the use of a conductor. Semiconducting materials, like Ge, satisfy these requirements, in a way best described by the concept of bands.

The electrical properties of a material are defined by the quality and the extent of its regular and periodic lattice structure, which established allowed energy bands for electrons that exist within that solid. In simple terms, the lower band, called the *valence band*, hosts those electrons confined to specific lattice sites, while the higher-lying *conduction band* contains those electrons which are free to migrate through the crystal. The two bands are separated by a finite *band gap*, the size of which effectively determines whether the material is classified as a semi-conductor or as an insulator. For insulators, the band gap energy is usually 5 eV or more, whereas for semiconductors considerably less, approximately 1 eV. In the absence of any excitations, in both materials the valence band is completely filled by the electrons bound to their specific lattice sites. Schematic band diagrams for different materials are shown in Figure 6.

At any nonzero temperature, electrons in the valence band can gain sufficient energy to cross the band gap and emigrate into the conduction band, leaving a vacancy (called a hole) in the valence band. The electron-hole pair becomes then free to move from its point of origin. The Ge detectors are cooled and operated at liquid Nitrogen temperature, 77K, to minimize this random thermal motion.

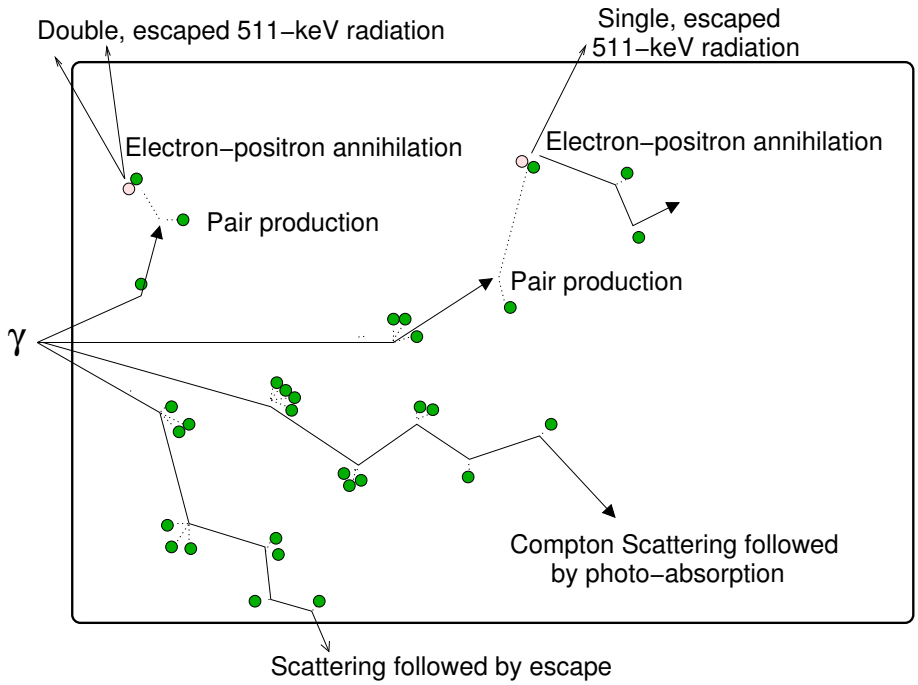

Figure 7: A scheme of possible modes of interaction between the incident γ radiation and the detector crystal.

Without thermal excitations, electrons are only liberated by the energy deposited by the incident radiation. With the application of an electric field to the semiconductor material, the liberated electrons and holes are forced to move in directions anti-parallel and parallel to the field, usually to be captured by an electrode at either end of the sample and detected as an electric signal, which is proportional to the incident γ-ray energy.

High Purity Germanium Detectors and BGO suppression

High purity germanium (HPGe) crystals are generally the semiconductor of choice for γ-ray studies. Their advantage include excellent energy resolution and detection efficiency. Energy resolution is particularly important for experiments which have many γ-rays emitted with similar energies, as in the case in fission. The energy resolution of a HPGe crystal, measured by the full width at half maximum (FWHM) of a 1.33-MeV γ-ray, is about 2 keV. The detection efficiency of a 3"$\times$3" HPGe crystal is about 80$\%$ that of a

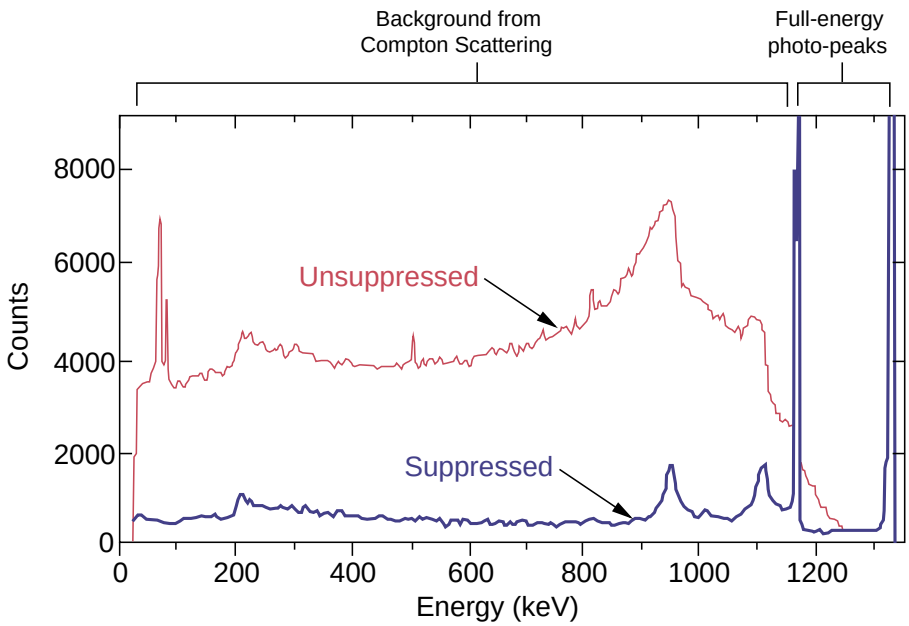

Figure 8: A spectrum which shows the reduction in Compton scattering background from shielding a HPGe detector with BGO crystals. The spectrum originates from ^{60}Co decay which releases gamma-rays at 1.173 MeV and 1.332 MeV.

similarly sized and positioned NaI scintillator.

Practically, for the HPGe crystal, several different interaction processes can occur that create false energy signals and these are shown in Figure 7. Multiple scattering by the incident γ ray releases electrons which are collected as part of the energy signal. The γ ray can escape from the crystal before imparting all of its energy leaving behind only a partial energy signal. The random nature of each escape means the partial energy signal is also random, the result of the Compton continuum. For incident γ-ray energies greater than 1022 keV, electron-positron pair production can occur followed by positron-annihilation. If one or both of the annihilation γ rays subsequently escapes, the net result is removal of exactly 511 or 1022 keV from the energy signal resulting in the corresponding escape peaks in the energy spectrum.

Any event in which the incident radiation escapes the Ge crystal is undesirable as the energy reported by the Ge crystal is then false. Such events can be ignored by the

use of suppression shields which detect the escaped radiations and thus allow the control system to deliberately ignore any Ge energy signal that they produce. A material often used as a suppression shields is the inorganic crystal Bismuth Germanite($Bi_4Ge_3O_{12}$), which is more commonly knows as BGO. The technique is to shield the 5 sides of the HPGe detector that are not facing the source with a scintillator that has a very high stopping power. The photons that escape from the HPGe then have a high probability of being detected by the surrounding scintillator and events where this occurs are rejected. Since the scintillator is used only to veto events, it need not have good energy resolution.

The Compton-suppression technique results in an improvement in the peak-to-total (P/T) ratio for a 1.3-MeV γ ray from about 0.25 for the bare crystal to about 0.6 when suppressed, as shown in Figure 8. This is an enormously important signal to background gain, without which high-fold coincidence measurements would not be practical.

The Gammasphere Array

The array of detectors used in our ^{252}Cf experiments is called Gammasphere, which was commissioned in 1995 at the Lawrence Berkeley National Laboratory [Lee97]. It consists of 110 high purity Ge detectors, spreading out spherically around the source chamber. Each detector is surrounded with a BGO suppression shield. The Ge detectors are kept cool with an automated liquid nitrogen delivery system, providing energy resolution of less than 3 keV at 1 MeV. Photopeak efficiency is around 10% at 1 MeV which is quite good for γ-ray detection. A picture of Gammasphere is shown in Figure 9.

A schematic diagram of a Gammasphere detector module is shown Figure 10. The Ge crystal was housed within a BGO suppression system comprised of a set of shields and a backing plug, with a purpose of acting as a detector of escaped radiations. The liquid nitrogen dewars for each detector was mounted, as usual, on the spherical, outer support hemisphere of the array. The tapered, heavy-metal collimators on the front face of every detector exposed a Ge solid angle of 0.418% each, meaning that, with $\approx$ 100 detectors

Figure 9: Gammasphere closed and ready for beam. The array is split vertically down the middle so that the system can be pulled apart for access to the source chamber at the center of the sphere.

operating, the total Ge coverage is approximately 42% of the complete sphere surrounding the γ-ray source.

The design of Gammasphere allows for the use of a wide variety of auxiliary detectors. These include external devices, such as a fragment mass analyzer, as well as devices designed to be placed inside the chamber. In our 2005 Experiment, a ΔE-E detector array was used to identify fragments from binary fission and ternary fission.

Gammasphere Calibration

In order to find out exact energies and relative intensities of γ-ray transitions, we have to calibrate the response of the Ge detectors. Some standard sources, ^{56}Co, ^{133}Ba and ^{152}Eu sources were used to measure detector energy calibration and efficiency curves. A γ-ray spectrum from the ^{152}Eu detected in detector 95 is shown in Figure 11. A detailed list of energies and intensities of γ-rays in those standard sources can be found in [Fir96].

Figure 10: A schematic diagram of a Gammasphere detector module showing the Ge crystal (∼10cm long), the BGO/photomultiplier suppression system, the housing for the electronic control system and also the liquid-nitrogen dewars used to cool the Ge crystal in order to suppress random thermal signals.

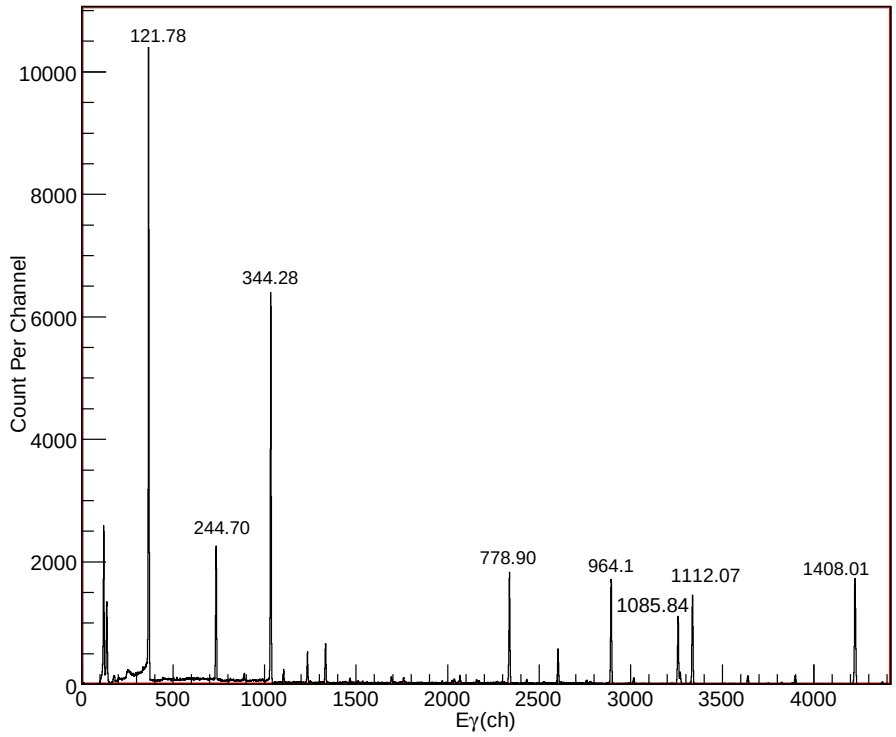

Figure 11: Calibration spectrum in detector 95 for ^{152}Eu source measurement.

The energy calibration for the detector array was fit to a third order polynomial,

$$E = a + bx + cx^2 + dx^3 \tag{1}$$

where *E* is the energy in keV, *x* is the channel number. The fitted coefficients are tabulated in Table 1.

The efficiency calibration of the Ge detectors was fit to the following equation:

$$eff = exp[(A + Bx + Cx^2)^{-G} + (D + Ey + Fy^2)^{-G}]^{-1/G} \tag{2}$$

where $x = log(E/100)$, $y = log(E/1000)$ and E is in keV. The quantity eff is a dimensionless multiplicative constant and E is energy in keV. The fit curve is shown in Figure 12. The calculated fit parameters are listed in Table 2.

Table 1: Fit coefficients for the 3rd order polynomial energy calibration of the Ge detectors from ADC channel space to energy in keV.

Fit Coefficient	Fit Value
a	-6.2734 $\times 10^{-1}$
b	3.3370 $\times 10^{-1}$
c	-9.0093 $\times 10^{-8}$
d	4.7999 $\times 10^{-12}$

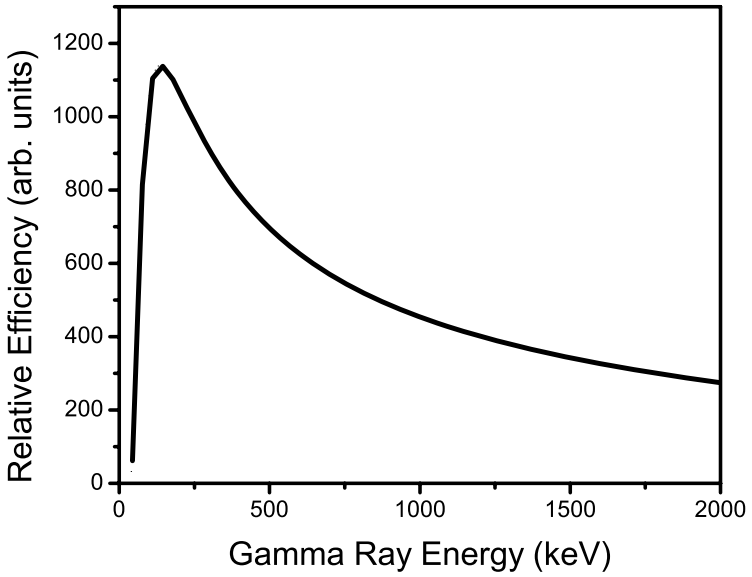

Figure 12: Gammasphere efficiency curve in arbitrary units.

Table 2: Fit coefficients of efficiency calibration of Gammasphere array.

Fit Coefficient	Fit Value	Fit Coefficient	Fit Value
A	14.1597	B	9.18559
C	-2.7907	D	6.36297
E	-0.65056	F	0.0
G	2.09765		

Triple coincident γ-ray measurements

Triple coincident technique

In the spontaneous fission of ^{252}Cf, more than 100 nuclei species are populated, with more than 3000 γ-rays emitted. Thus, the spectra are very complicated and in any single γ gate, one see not only the transitions in coincidence with this γ in this nucleus, but also the transitions from its five to ten different partners, and many other random coincident γ transitions. To eliminate most of the γ rays not belonging to a particular isotope of interest and one partner, the triple-coincidence technique was employed. Triple coincident events are processed to construct a cube, with energy of each of the three γ-rays is placed along an axis of the cube. For example, three γ-rays of energies E_1, E_2 and E_3 are detected within the time window. In the coincidence cube, the count at (E_1,E_2,E_3) is added by 1. Since each axis is constructed symmetrically, so we have

$$N(E_1, E_2, E_3) = N(E_2, E_1, E_3) = N(E_3, E_2, E_1)$$
$$= N(E_1, E_3, E_2) = N(E_2, E_3, E_1) = N(E_3, E_1, E_2) \quad (3)$$

and so on. Higher-fold events are unfolded into triple coincidences during this process.

The analysis of the cube data was performed by the Radware software package [Rad95]. This package provides programs to sort experimental data into histogram matrices and cubes. Programs to analyze cubes are provided as well, to create coincidence spectra with given gating γ-ray energies. During the processing of our 2000 experimental data, we set the time window to 200 ns to include most prompt coincidences, while filtering out a vast majority of random events.

To show the effect of the triple coincidence technique, let us look at one example. A partial ground state band cascade in ^{102}Zr is shown in Figure 13. All of these transitions should be in prompt coincidence, as a nucleus created in a 10^+ state will cascade through each of these levels in a very short period of time, emitting γ transitions down to the ground. Figure 14(a) is the full projection of the cube onto one axis. There are many strong peaks,

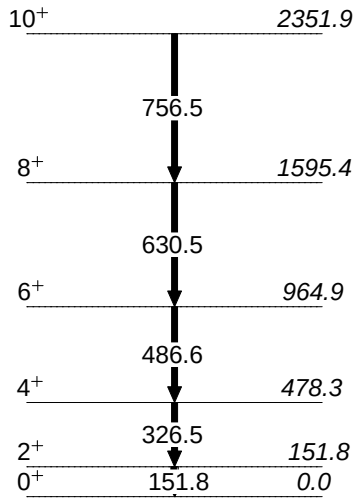

Figure 13: Partial ground state band of ^{102}Zr. Energies are in keV.

as well as a high level of background. Stronger peaks can be evaluated, but the weaker peaks are obscured. Figure 14(b) is with a single γ-ray gate of 151.8 keV in ^{102}Zr. The counts become lower, with a few peaks more clear and less background. When we apply a double gate using 151.8- and 326.5- keV gates, as shown in Figure 14(c), the background has been reduced to very low level. The peaks belonging to ^{102}Zr (486.6, 630.5, 756.5 keV) are clearly identified. The transitions from Ce partner isotopes are also clearly present (^{146,147,148}Ce). With this technique, we are able to resolve weak peaks from the background.

Level Scheme Construction

Using the triple coincidence technique, we are able to identify transitions which belong to the nucleus of interest. Once the transitions are ordered with respect to one another, we can identify important band structures and understand the behavior of the nucleus in terms of nuclear models.

If we have previous known γ-rays in a nucleus, such as from β^- decay, we can set gates on these transitions and look for a self-consistent set of new transitions that appear in coincidence with these and each other. The other way to identify new isotopes or new transitions is to rely on their fission partner. The corresponding fission partner is created in coincidence with the fragment of interest. In a spectrum gated on transitions in one

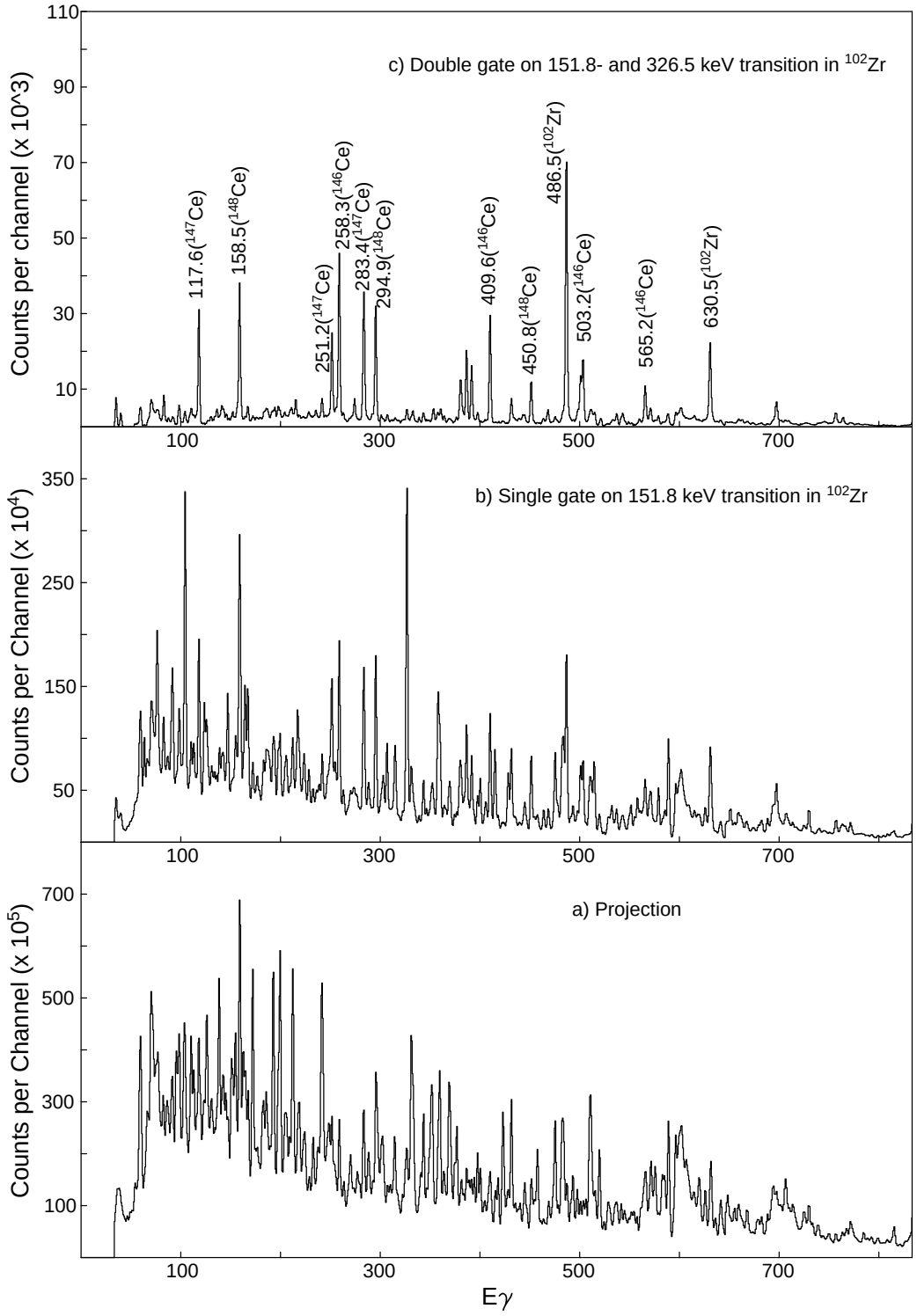

Figure 14: Triple coincidence gating series in ^{102}Zr

nucleus, the transitions from the partner nuclei will be visible as well. As shown in Figure 14(c), when we gate on 151.8 and 326.5 keV transitions, we can see various Cerium partner transitions. By cross-checking the coincidence relationships, we can check the assignment of transitions to a particular isotope.

The relative intensities of γ-rays provide us important information about their locations in the level scheme. As an example, in the above-mentioned ^{102}Zr gates, transitions out of higher spin states in the ground-band of ^{146}Ce appear less intense than the ones near the ground state. This is due to the fact that a nucleus populated with high spin will transition through all the low spin states on the way to ground. So every nucleus created will go through the bottom transitions, but only the ones statistically created with high spin will emit transitions from higher levels.

Assigning J^{π} to nuclear levels is often a difficult process. Ground state spins and parities are deduced by using shell structures and regional systematics. From direct measurements of electron conversion coefficients, the multipole nature of nuclear transitions can be determined. The multipolarity of an electromagnetic transition reflect the spin and parity of the nuclear levels involved in the transition. The intrinsic spin of the photon is one, and thus the angular momentum change for a γ-ray transition must be integral. Between an initial state with a spin J_i and a final state with a spin J_f, the transition must carry an angular momentum L where L obeys the *selection rule*:

$$|J_i - J_f| \leq L \leq |J_i + J_f|. \tag{4}$$

This angular momentum transfer defines the multipole order of the transition, which are called dipole, quadrupole, octupole, ... moments.

If we also examine the parity of the nuclear levels, we can determine the multipole type. For a parity change of $(-1)^L$, the nuclear couples to the electric field of the photon, and it is an electric transition. For a parity change of $-(-1)^L$, the nucleus couples to the magnetic field of the photon, and it is a magnetic transition. For a given pair of nuclear levels, the lowest order multipole almost always dominates, making the contribution of

higher orders very small. For example, consider a transition between a state with a J^π of 4^+ and a state with a J^π of 2^+, the allowed range of L for the photon is between 2 and 6. Since there is no parity change, the possible multipole transitions are E2, M3, E4, M5, and E6. However, since the transitions probabilities of higher order transitions will be so small, in practice, this will usually be an E2 transition with a possible minor contribution from an M3. There is one common exception to this rule. In the case of $\Delta I = 1$ to 3, eg. $2^+ \rightarrow 2^+$, where M1, E2, M3, E4 are allowed. Collective effect can enhance the E2 over the M1 multipole. There are also a few cases that E3 can compete with E1 multipolarities because of collective effect.

Experimental Details

1995 Binary Fission

In 1995, a binary fission experiment was performed at Lawrence Berkeley National Laboratory. A 28μ Ci source was sandwiched between two foils of Ni with thickness 11.3 mg/cm^2 on either side. In addition, a 13.7 mg/cm^2 Al foil was added on both sides. Gammasphere consisted of 72 Ge detectors. There were 9.8×10^9 triple or higher fold events recorded.

2000 Binary Fission

In 2000, a binary fission experiment was performed at Lawrence Berkeley National Laboratory. A 62μCi source, sandwiched between two Fe foils with thickness 10 mg/cm^2 and encased in a 7.62 cm polyethylene ball, was used. This experiment resulted in 5.7×10^{11} triple-fold $\gamma-\gamma-\gamma$ events. This is the largest data set recorded, and was used for most triple-coincidence studies. A $\gamma-\gamma-\gamma$ coincident cube was constructed with minimal compression to maximize the energy resolution in our analysis spectra. 101 detectors were functional in this experiment. Raw experimental data were copied onto a RAID disk array

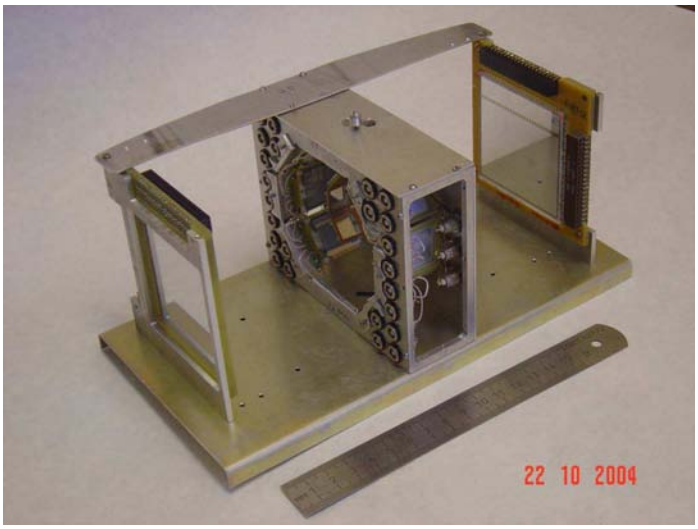

Figure 15: E-ΔE detector array used in Jan. 2005 ANL experiment

for angular correlation and g-factor measurements.

2005 Binary and Ternary Fission

In 2005, another fission experiment was performed at ANL. This experiment was focused on detecting the primary fission fragments directly. Correspondingly, the source was left barely covered. The ^{252}Cf had a strength of 35 μCi deposited on a 1.5 μm Ti foil and covered with another thin 1.5 μm layer of Ti. Two double-sided silicon strip detectors (DSSDs) were placed on either side of the source. The DSSD was 1.85 mm thick, with an area of 60 $\times$ 60 mm^2 split into 32 strips on each side. In addition, 6 ΔE-E telescopes were arranged in a ring perpendicular to the source-DSSD axis. The ΔE detectors were about 10 μm thick. The E detectors had a thickness of 1 mm with an area of 20 $\times$ 20 mm^2 split into 4 square sectors for increased granularity. A picture of the detector array is shown in Figure 15. The two DSSDs can be seen flanking the ring array of ΔE-E detectors. The source was placed in the center of the array, so fission fragments travel towards the DSSDs and the LCPs are ejected orthogonally, towards the ΔE-E detectors. The data were recorded with fragment-fragment-γ-γ coincidence for binary fission and fragment-fragment-LCP-γ coincidence for ternary fission.

CHAPTER III

STUDY OF STRUCTURE OF NEUTRON-RICH NUCLEI

With sophisticated experimental equipments and analytical techniques developed, we are able to study neutron-rich nuclei produced from the spontaneous fission of ^{252}Cf with greater details. The data used to study the structure of several neutron-rich nuclei were collected in the 2000 ^{252}Cf binary fission experiment. The data were sorted into a less compressed cube for analysis. All four- and higher-fold events were unfolded down to triple fold events. The Radware software package [Rad95] was used to analyzed the data.

Neutron-rich nuclei in the A$\sim$100 region, where the valence nucleons begin to fill the $g_{9/2}$ proton and $h_{11/2}$ neutron orbitals, exhibit several interesting features. For the Sr ($Z = 38$) and Zr ($Z = 40$) nuclei, a sudden shape transition from spherical to strongly deformed ground states ($\beta_2 \sim 0.40$) at $N = 60$ has been reported [Urb01] [Lhe01]. The emerging γ degree of freedom in the Mo-Ru region and the predicted prolate-to-oblate shape transition in the Pd isotopes have been identified [Che70] [Hot91] [Ham95] [Luo05]. The structures of nuclei in this region are suitable for various theoretical models [Mol95]. We have studied $^{88-94}$Kr, ^{102}Zr, and ^{114}Ru in this region. A number of new transitions, states, and band structures have been identified. Spin/parity configurations were assigned by following regional systematics and angular correlation measurements.

Studies of neutron-rich nuclei near the $N = 82$ closed shell with a few protons beyond the $Z = 50$ closed shell are of interest to test nuclear shell model calculations that utilize effective interactions. Two neutron-rich Cs isotopes, ^{137}Cs and ^{138}Cs, have been investigated in this work. Being adjacent to the doubly magic nucleus ^{132}Sn, the structure of these nuclei could provide additional understandings of the proton-neutron and proton-proton interactions and of the similarities of the structures of nuclei around ^{132}Sn and ^{208}Pb [Fir96].

$^{88-94}$Kr

The even-even $^{88-94}$Kr nuclei lie close to the $N = 50$ closed shell. Studies of high spin states in these neutron-rich nuclei can provide new insights into both collective and quasi-particle excitations in this mass region. Prior to this work, they have been investigated through β-decay [Fir96], spontaneous fission of ^{248}Cm [RU00] (shown in Figure 16), and spontaneous fission of ^{252}Cf [Zha01]. But there are some disagreements between the ^{248}Cm work [RU00] and the ^{252}Cf work [Zha01]. It's interesting to investigate these isotopes, by analyzing our high statistics data from 2000 experiment. The fission partner of Kr isotopes are Sm isotopes. By cross-checking coincident relationships and relative intensities, we have identified new transitions in $^{88-94}$Kr isotopes and expanded their level schemes.

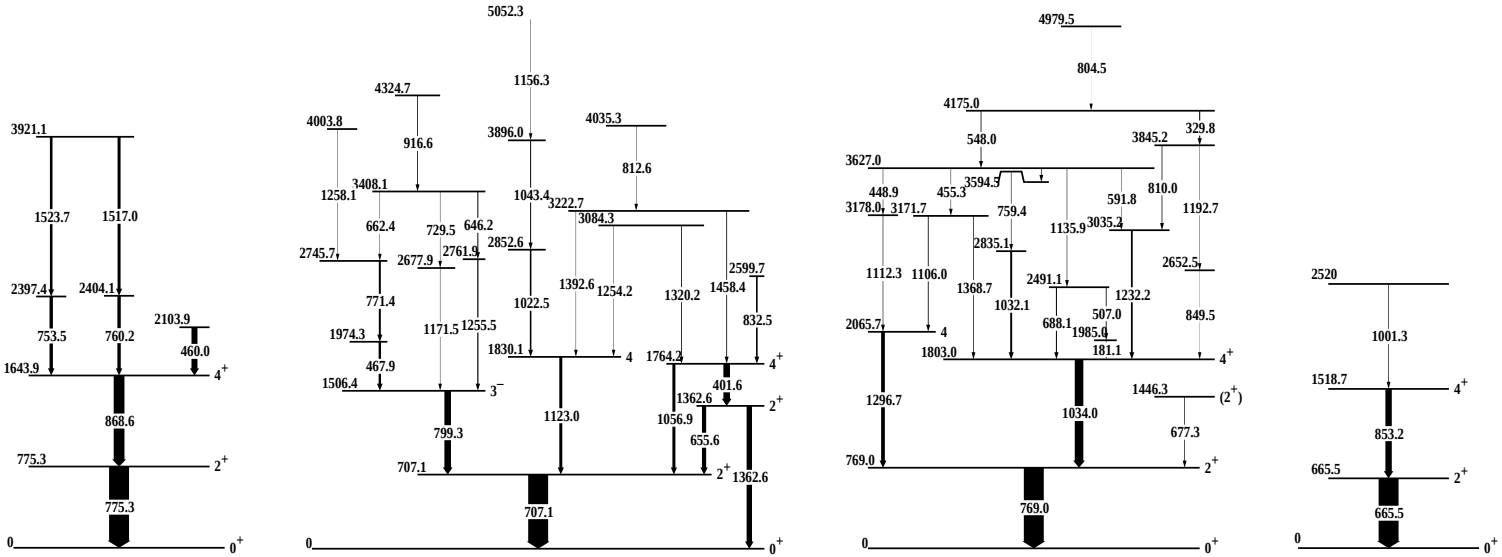

$^{88}_{36}Kr_{52}$ $^{90}_{36}Kr_{54}$ $^{92}_{36}Kr_{56}$ $^{94}_{36}Kr_{58}$

Figure 16: Level Schemes of $^{88-94}$Kr reported in [RU00].

^{88}Kr

The level scheme of ^{88}Kr built in this work is shown in Figure 17. Transitions identified in from previous work [RU00] has been confirmed. The level scheme has been extended up to a 7169.4-keV state, with ten new transitions and eight new states identified. The sequence of 1517.2- and 760.4-, 1523.7- and 753.9-keV transitions have been firmly rearranged, by measuring relative intensities. A spectrum double-gating on the 775.5- and 868.6-keV transitions is shown in Figure 18. Transitions identified in high and low energy regions, including some partner transitions, are clearly identified.

For the spin and parity assignments, we compared ^{88}Kr with its neighboring $N = 52$ isotones, ^{86}Se and ^{90}Sr. The level scheme of ^{86}Se was reported from spontaneous fission of ^{252}Cf work [Jon06]. The structure of ^{90}Sr was studied through ^{82}Se(^{11}B, $p2n$) reaction and shell-model calculations [Ste01]. We have noticed an extraordinary similarity in level structure between these $N = 52$ isotones, as shown in Figure 19. Note here the level scheme of ^{86}Se has been expanded and the 2073-keV level is assigned as 3^-, compared with recent work in [Jon06]. We assigned spins and parities by following the systematics, with level schemes of neighboring nuclei shown in Figure 19. The 775.5- and 1644.1-keV states are vibrational 2^+ and 4^+ states of a near-spherical nucleus. And 3^-, 4^-, 5^-, and 6^- were assigned to the 2104.2-, 2856.5-, 3296.7-, and 3906.2-keV states. Spins and parities of 5^- and 7^- were assigned to the 3161.3- and 3921.7-keV states. Spins and parities of 6^+, 8^+, 10^+, and 12^+ were assigned to the 3167.8-, 5194.0-, 6232.9-, and 7169.4-keV states.

^{90}Kr

The level scheme of ^{90}Kr identified in this work is shown in Figure 20. Most transitions and levels in [RU00] are confirmed. The 1075.8-, 319.9-, 1245.3-, 811.7-, 1200.0-, 673.0-, and 1099.0-keV transitions are newly identified.

We can see a somewhat similar pattern of level schemes for ^{90}Kr and ^{88}Kr, as well as for ^{90}Kr and ^{92}Sr [Ste02]. From the similarities, the 707.6- and 1506.7-keV states are

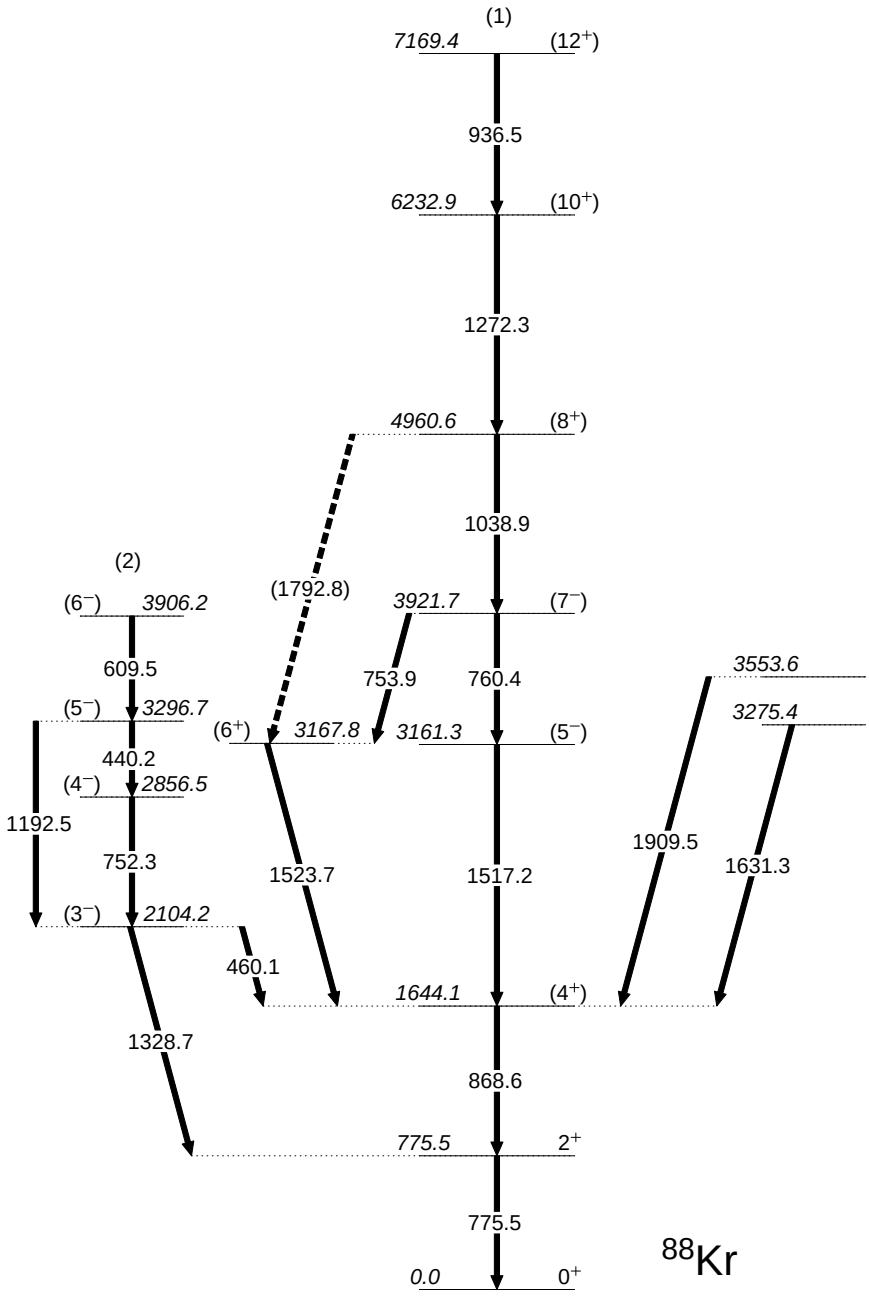

Figure 17: Level Scheme of ^{88}Kr. Energies are in keV.

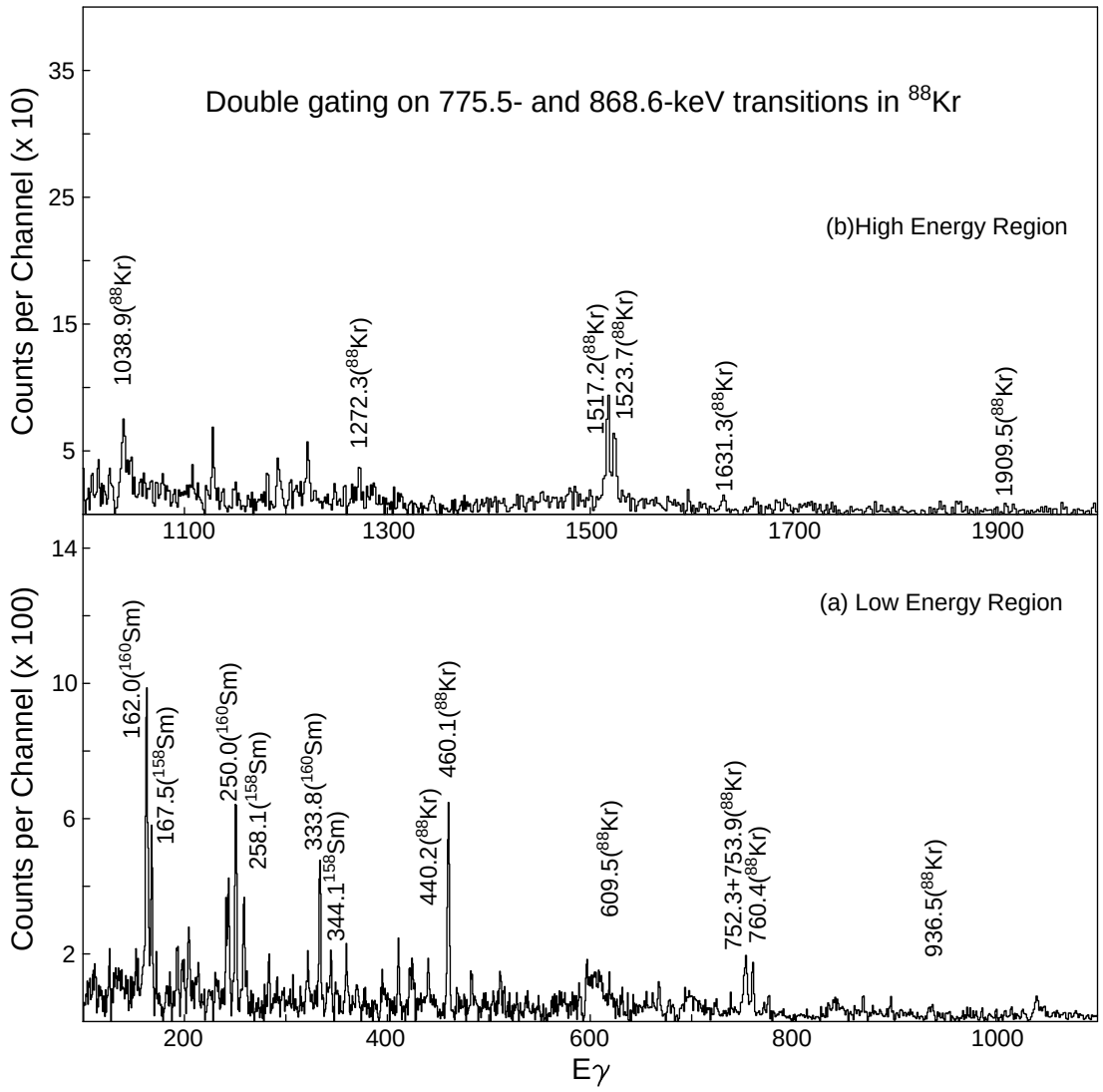

Figure 18: A spectrum double-gating on 775.5- and 868.6-keV transitions in ^{88}Kr. Low energy and high energy transitions are shown in (a) and (b).

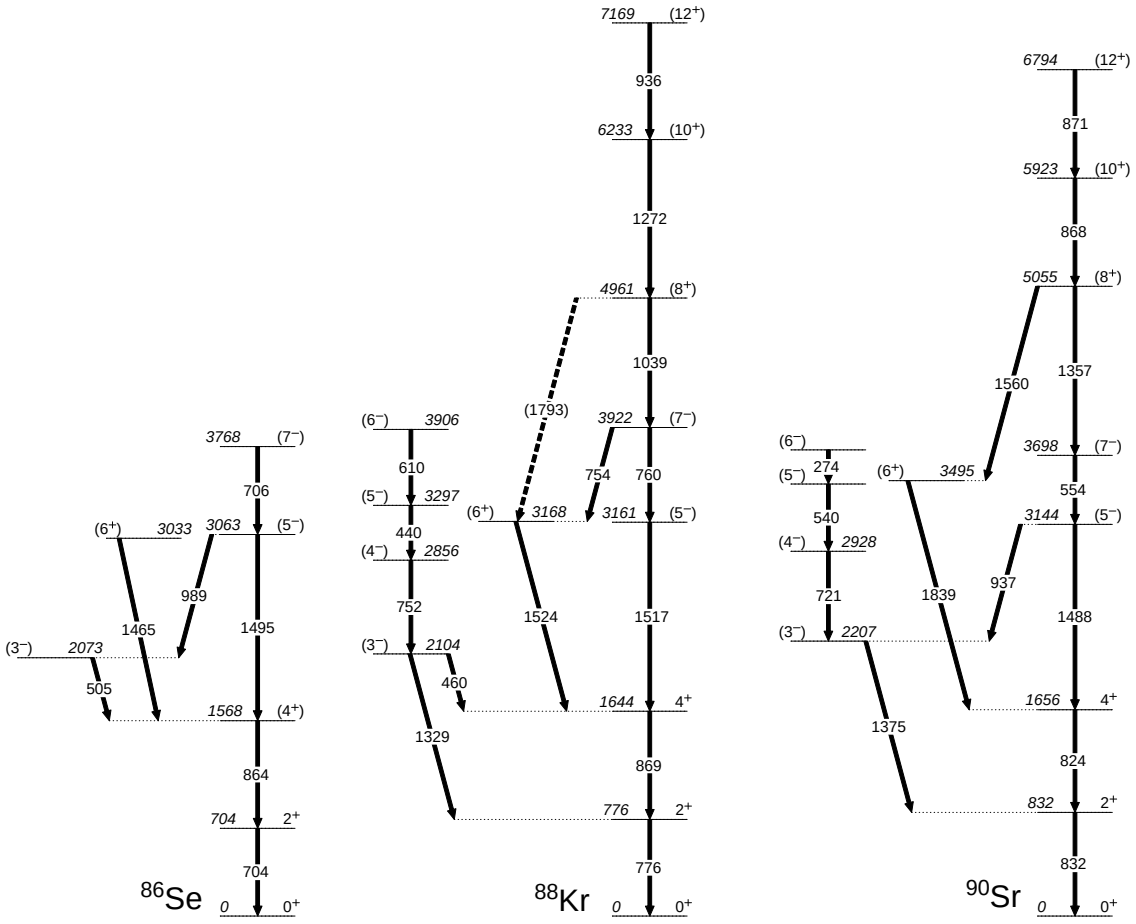

Figure 19: A comparison of level structures of $N = 52$ isotopes, ^{86}Se [Jon06], ^{88}Kr, and ^{90}Sr [Ste01]. Three new levels and four new transitions have been identified in ^{86}Se in this work and now 3^- is assigned to the 2073-keV level.

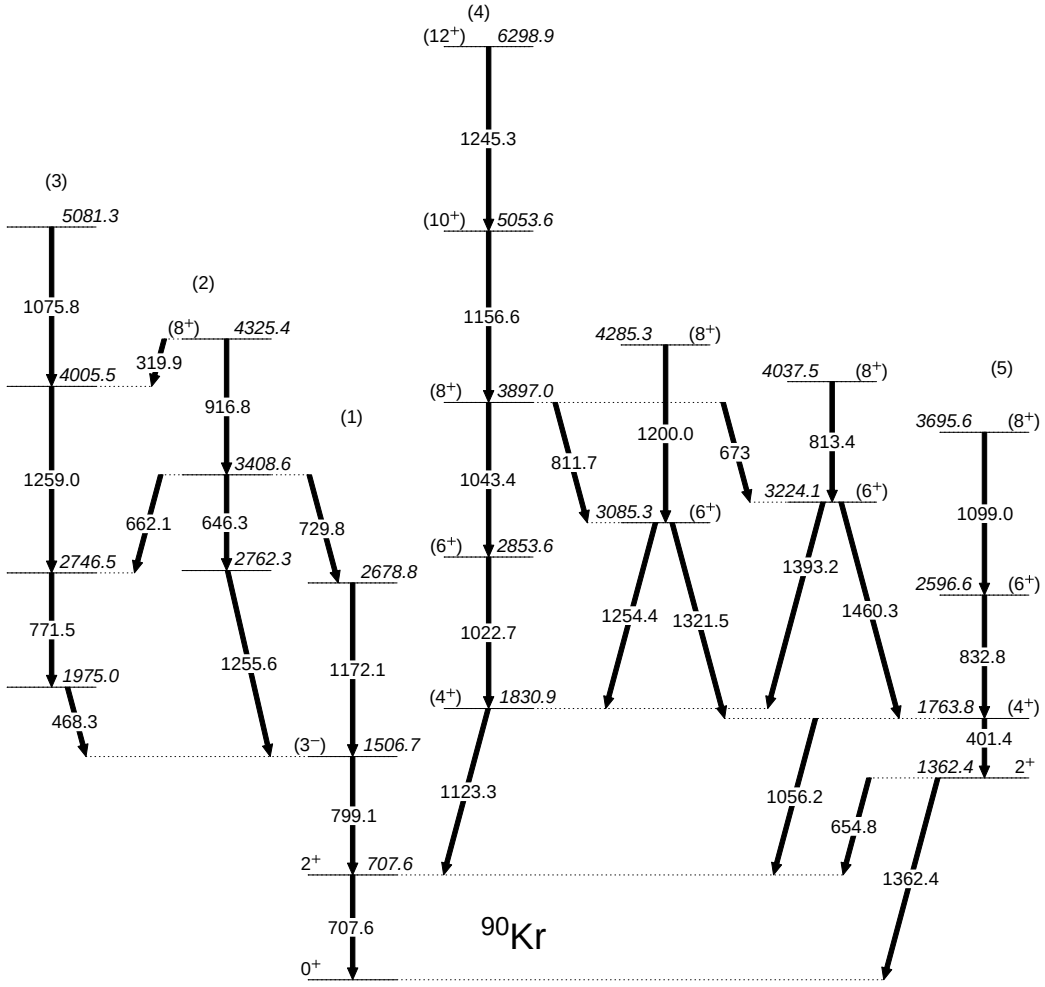

Figure 20: Level Scheme of ^{90}Kr. Energies are in keV.

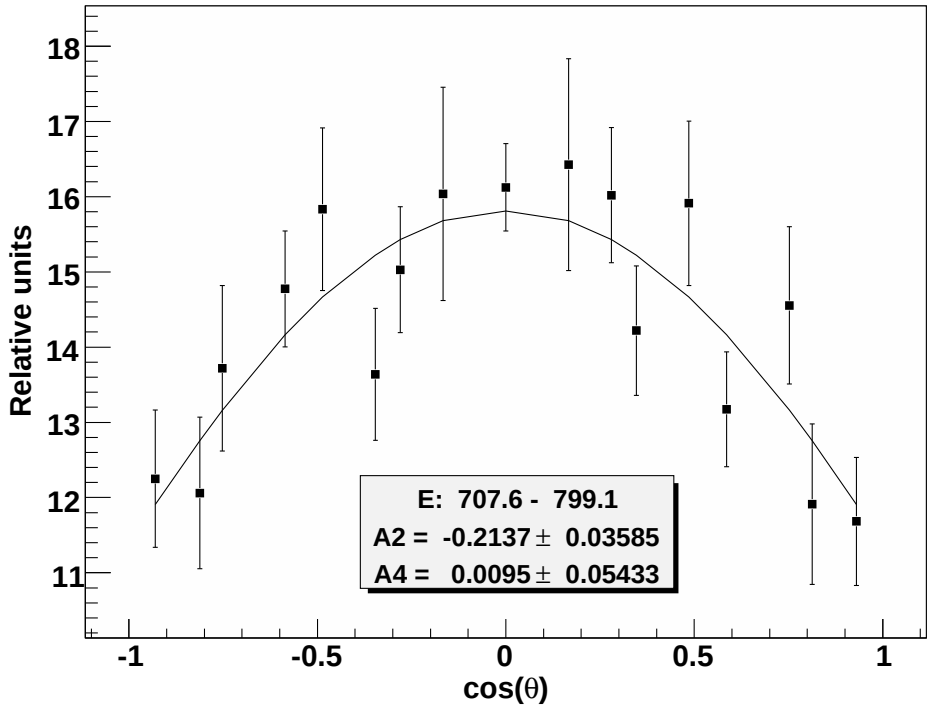

Figure 21: Angular correlation measurement of 707.6-799.1 keV cascade in ^{90}Kr.

likely to be 2^+ and 4^+ vibrational states, as given in [Zha01]. However, in [RU00], the 1506.7-keV state was assigned spin of 3^-, by angular correlation measurements. In this work, we carried out angular correlation measurements of the 707.6-799.1 keV cascade, using a technique developed recently [Dan07], which will be discussed in the next chapter. The measurement of angular correlation between the 707.6- and 799.1- keV transitions is shown in Figure 21, with $A_2^{exp} = -0.21(4)$, $A_4^{exp} = 0.01(5)$. These values are consistent with the values in [RU00], and agree with theoretical prediction for a 3^-(D)2^+(Q)0^+ cascade [Tay71]. For a $4^+ - 2^+ - 0^+$ cascade, the A_2^{the} is 0.102. The result supports the assignment of 3^- to the 1506.7 keV state. Therefore, we have confirmed that the 799.1-keV transition is a dipole transition with primarily an E1 character. So for $N = 54$ isotones, the level systematics are broken, when we compare the 3^- state energy in ^{90}Kr with its neighboring isotones. Band (4) and (5) are assigned with positive parities tentatively, which is in agreement with [RU00] and [Zha01]. However, band (5) built on the 1362.4-keV level is significantly different from band (2) in [Zha01] built on the same level.

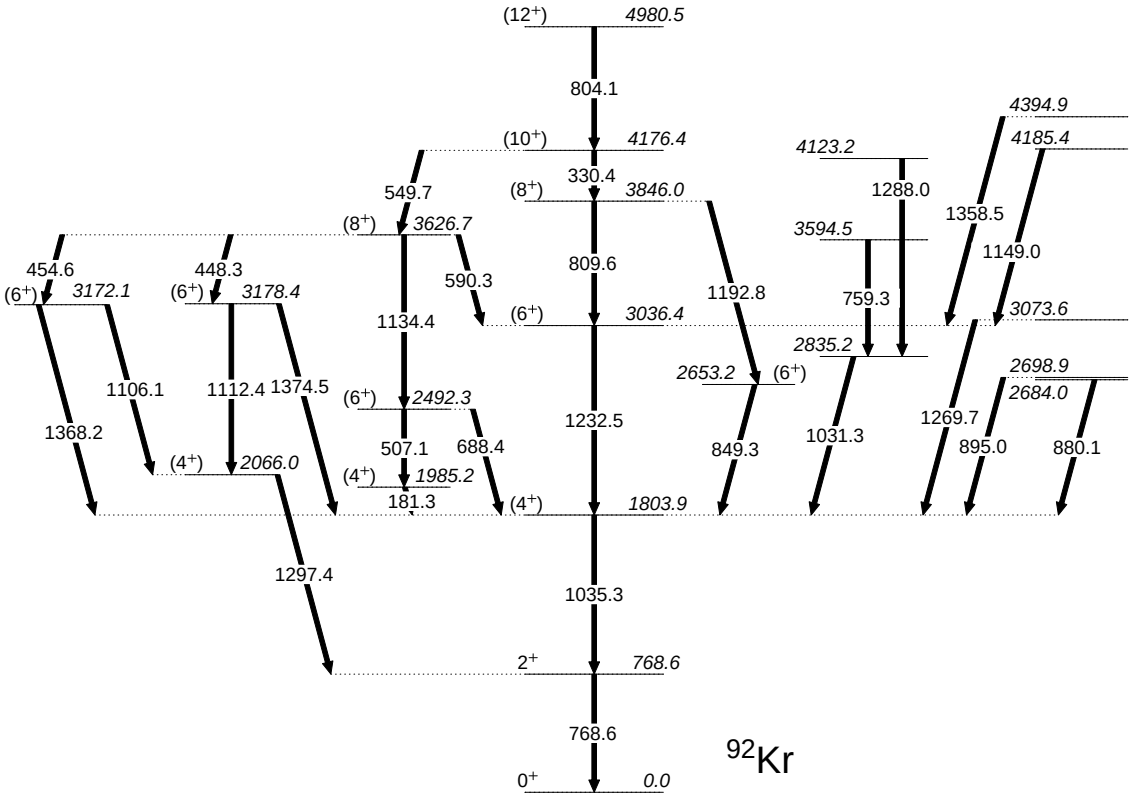

Figure 22: Level Scheme of ^{92}Kr. Energies are in keV.

^{92}Kr

The level scheme of ^{92}Kr built in this work is shown in Figure 22. Compared to work in [Zha01] and [RU00], the 1374.5-, 1288.0-, 880.1-, 895.0-, 1269.7-, 1149.0-, and 1358.5-keV transitions are identified, with six new excited states added to the level scheme of ^{92}Kr. Spins and parities are assigned tentatively, with agreement of assignments in [RU00].

^{94}Kr

The level scheme of ^{94}Kr reported in [RU00] and [Zha01] has been confirmed, as shown in Figure 23. Due to its low yield, we did not observe any new transitions and states.

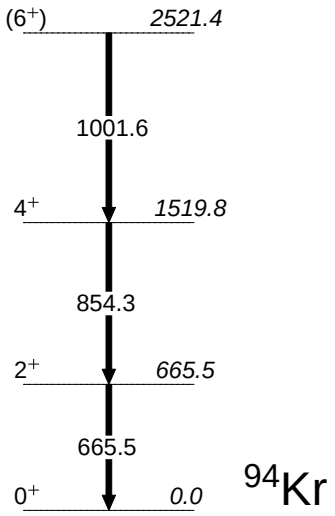

Figure 23: Level Scheme of ^{94}Kr. Energies are in keV.

Discussion

In Figure 24, energies of 2^+ state in ground bands of even-even Kr, Sr, and Zr isotopes are shown. In Zr isotopes, we can see a well-known subshell closure at $N = 56$. But in Kr and Sr, the 2^+ state energies are not significantly higher than their neighboring isotopes. The first 3^- excitation state energies in even-even Kr, Sr, and Zr isotopes are given in Figure 25. We have observed a similar trend in Sr and Zr. But for Kr, an extraordinarily low energy 3^- state is observed. This was interpreted as due to the $\nu(d_{5/2}h_{11/2})_{3^-}$ contribution to the octupole phonon [RU00]. Detailed theoretical analysis is required to explain the above-mentioned results, and to find out the contributions of $\pi p_{3/2}$, $\pi f_{5/2}$, $\nu d_{5/2}$, $\nu f_{7/2}$ orbitals and corresponding to particle-hole excitations, as discussed in [Ste01], [Ste02] and [RU00].

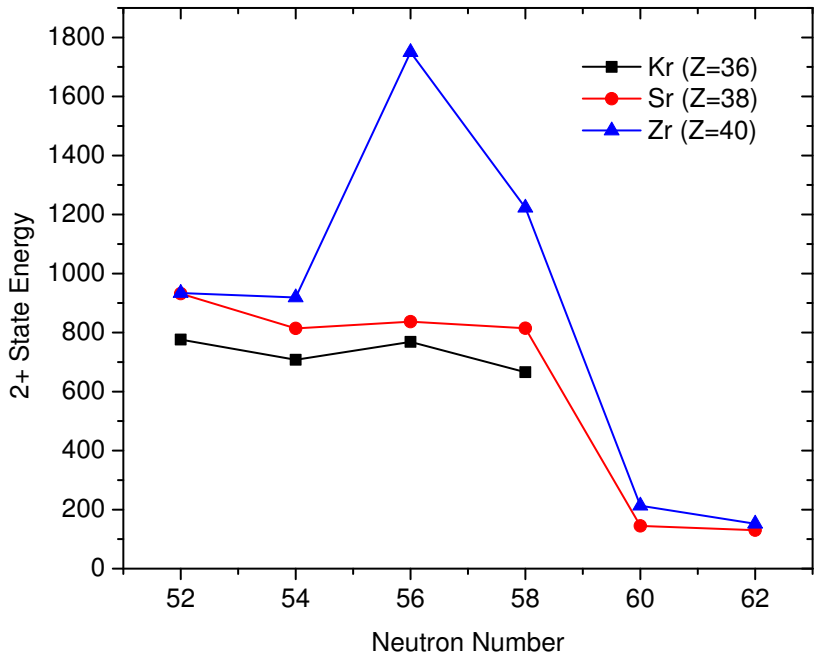

Figure 24: Energies of 2^+ state in ground bands of even-even Kr, Sr, and Zr isotopes.

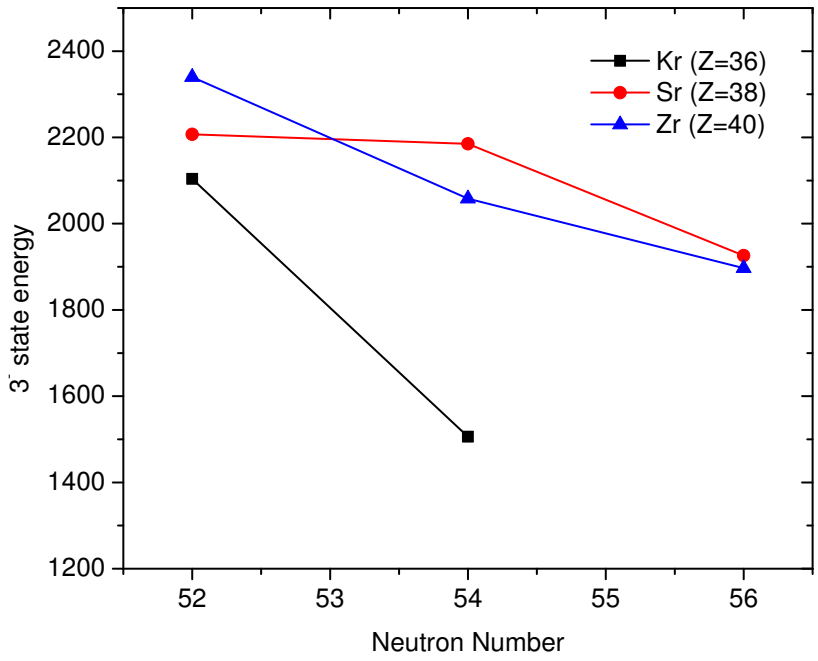

Figure 25: Energies of first 3^- state in even-even Kr, Sr, and Zr isotopes.

^{102}Zr

Studies of the neutron-rich Zr nuclei have shown that in the even-even Zr nuclei, the deformation parameters increase gradually from $\beta_2 \sim 0.1$ at $N = 56$, through $\beta_2 \sim 0.2$ at $N = 58$ to $\beta_2 \sim 0.4$ at $N = 64$ [Urb01]. B(E_2) value measurements and lifetime measurements indicate that in ^{98}Sr and ^{100}Zr, their different shape coexisting bands are weakly admixed [Hwa06b] [Hwa06a]. The lifetime measurements also indicates that ^{104}Zr has the most deformed 2^+ state among medium and heavy even-even nuclei, except for ^{102}Sr [Hwa06a]. For ^{102}Zr, the transition from 2^+ state to 0^+ state in ground band was first reported by Cheifetz *et al.* from spontaneous fission of ^{252}Cf [Che70]. Transitions from the ground-band states were observed up to the 8^+ level and a large deformation was deduced. In a β-decay work [Hil91], two more postulated 0_2^+ and 2_2^+ states were identified. From spontaneous fission of ^{248}Cm by Durell *et al.* [Dur95], the ground band was extended up to 12^+. A new two-quasi-particle state was identified and the pair strengths in neutron-rich Zr isotopes were calculated. At the same time, from the 1995 experimental data of our group [Ham95], Durell's work was confirmed, with one more band identified. In the recent ^{238}U(α, f) fusion-fission reaction work [Hua04], the deformed ground band has been firmly established up to 20^+, with more states identified in the two rotational bands built on two-quasi-particle states. With our high statistical data from our 2000 binary fission experiment, we are going to identify new transitions, states and band structures.

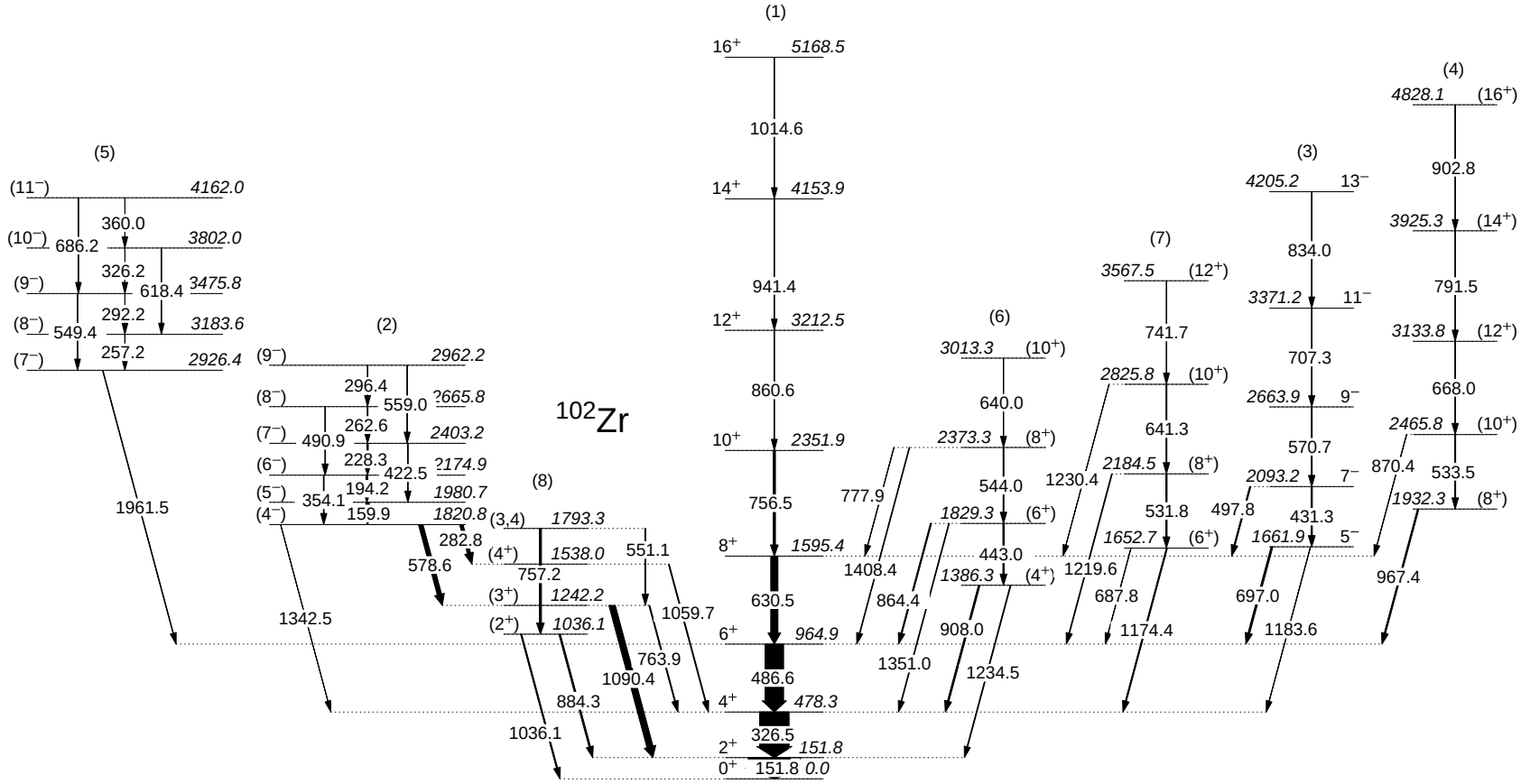

Figure 26: Level Scheme of ^{102}Zr constructed in this work. Energies are in keV. The 27.5-keV transition from the 1820.8- to the 1793.3-keV state is not drawn.

Experimental results

The fission partner of Zr are Ce isotopes. Double-gating on the known γ-ray transitions in ^{102}Zr and the Ce partner isotopes, new transitions and excited states have been identified. The scheme of ^{102}Zr has been considerably extended and expanded, as shown in Figure 26. Note that there is a 27.5-keV transition from the 1820.8-keV state to the 1793.3-keV state. The relative intensities of γ-ray transitions in ^{102}Zr from this work are listed in Table 3.

The ground band was confirmed up to the 14^+ state. We did not observe the 1098.1- and 1184.6-keV transitions in the ground band, the 331.5- and 628.4-keV transitions in band (2), nor the 955.5 keV transitions in band (3), which were reported in [Hua04]. They had advantage of correction for Doppler smearing of these transitions, particularly at high spins, since they measured and corrected for Doppler shift of the fragments in flight. This enabled them to observe high spin transitions with much lower intensities. In Figure 27, two spectra are shown, one with double gating on the 151.8- and 326.5-keV transitions, and the other with double gating on the 326.5- and 486.6-keV transitions. The crossing feeding transitions from side bands to ground bands are shown. The 908.0-, 1174.4-, 1183.6-keV transitions are clearly seen in the 151.8- and 326.5-keV gate. The crossing 864.4-, 697.0-, 967.4-, and 1219.6-keV transitions are clearly seen in the 326.5- and 486.6-keV gate.

The two-quasi-particle band, labeled as (2), was reported in [Dur95] [Ham95] [Hua04]. We confirmed this band, as well as band (3) and band (4). We also confirmed the states listed in band (8), which were reported in [Dur95].

A new rotational band, labeled as (5), has been identified for the first time. By gating on the 326.5- and 486.5-keV transitions in ^{102}Zr, we identified a 1961.5 keV transition which belongs to ^{102}Zr, as shown in figure 27(b). Figure 28(a) shows a spectrum double gating on the 486.5- and 1961.5-keV transitions. In this spectrum, we can see the 257.2-, 292.2-, 326.2-, and 360.0- keV transitions of high lying band (5). In Figure 28(b), a spectrum gating on 1961.5 and 257.2 keV transitions is shown. The transitions in this band and

Table 3: Relative intensities (I_γ) of γ-ray transitions (keV) in ^{102}Zr. Intensity errors range between 5% for the strong transitions and 30% for the weak transitions.

E_γ(keV)	I_γ(%)	E_i(keV)	E_γ(keV)	I_γ(%)	E_i(keV)	E_γ(keV)	I_γ(%)	E_i(keV)
151.8	100	151.8	159.9	7.7	1980.7	194.2	4.2	2174.9
228.3	3.3	2403.2	257.2	0.9	3183.6	262.6	1.8	2665.8
282.8	8.0	1820.8	292.2	0.9	3475.8	296.4	0.9	2962.2
326.2	0.4	3802.2	326.5	69	478.3	354.1	1.6	2174.9
360.4	0.2	4162.0	422.5	1.5	2403.2	431.3	3.3	2093.2
443.0	3.2	1829.3	486.6	44	964.9	490.9	1.3	2665.8
497.8	2.8	2093.2	531.8	3.1	2184.5	533.5	2.2	2465.8
544.0	2.1	2373.3	549.4	0.6	3475.8	551.1	0.2	1793.3
559.0	1.0	2692.2	570.7	2.1	2663.9	578.6	10.5	1820.8
618.4	0.1	3802.2	630.5	17	1595.4	640.0	1.0	3013.3
641.3	2.0	2825.8	668.0	1.8	3133.8	686.2	0.1	4162.0
687.8	0.9	1652.7	697.0	4.2	1661.9	707.3	1.5	3371.2
741.7	0.9	3567.5	756.5	5.2	2351.9	757.2	3.7	1793.3
763.9	2.2	1242.2	777.9	1.0	2373.3	791.5	1.0	3925.3
834.0	0.8	4205.2	860.6	0.9	3212.5	864.4	2.7	1829.3
870.4	0.9	2465.8	884.3	3.6	1036.1	902.8	0.8	4828.1
908.0	3.7	1386.3	941.4	0.5	4153.9	967.4	3.3	1932.3
1014.6	0.3	5168.5	1036.1	2.8	1036.1	1059.7	2.0	1538.0
1090.4	15	1242.2	1174.4	2.7	1652.7	1183.6	0.7	1661.9
1219.6	1.7	2184.5	1230.4	0.6	2825.8	1234.5	1.6	1386.3
1342.5	0.6	1820.8	1351.0	1.4	1829.3	1408.4	1.1	2373.3
1961.5	1.3	2926.4						

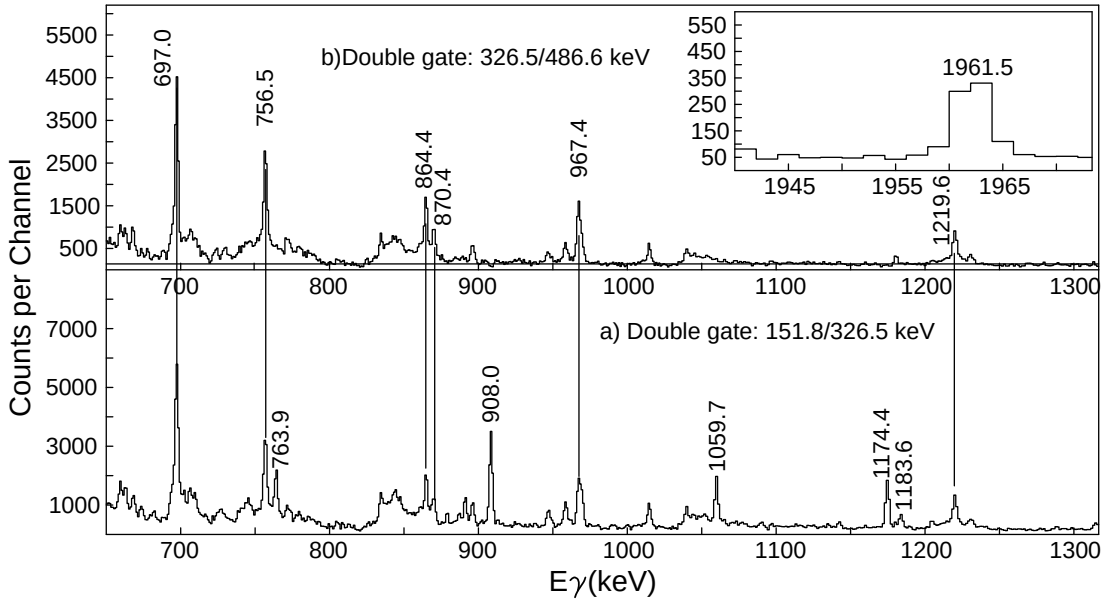

Figure 27: Coincidence spectra with double gates set on (a) 151.8- and 326.5-keV transitions and (b) 326.5- and 486.6-keV transitions in ^{102}Zr.

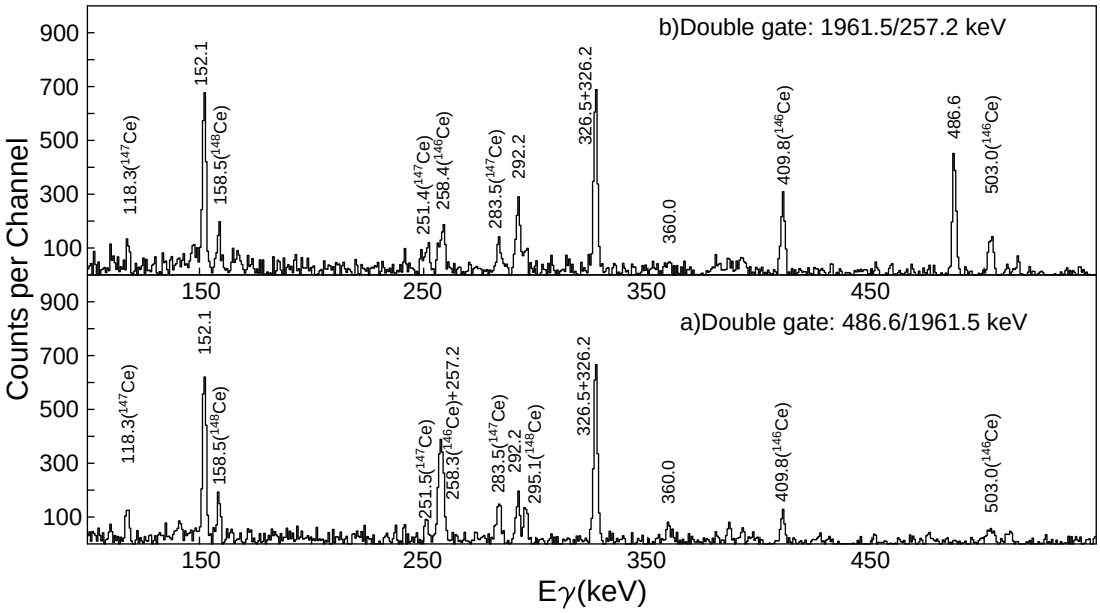

Figure 28: Coincidence spectra with double gates set on (a) 486.6- and 1961.5-keV and (b) 1961.5- and 257.2-keV transitions in ^{102}Zr.

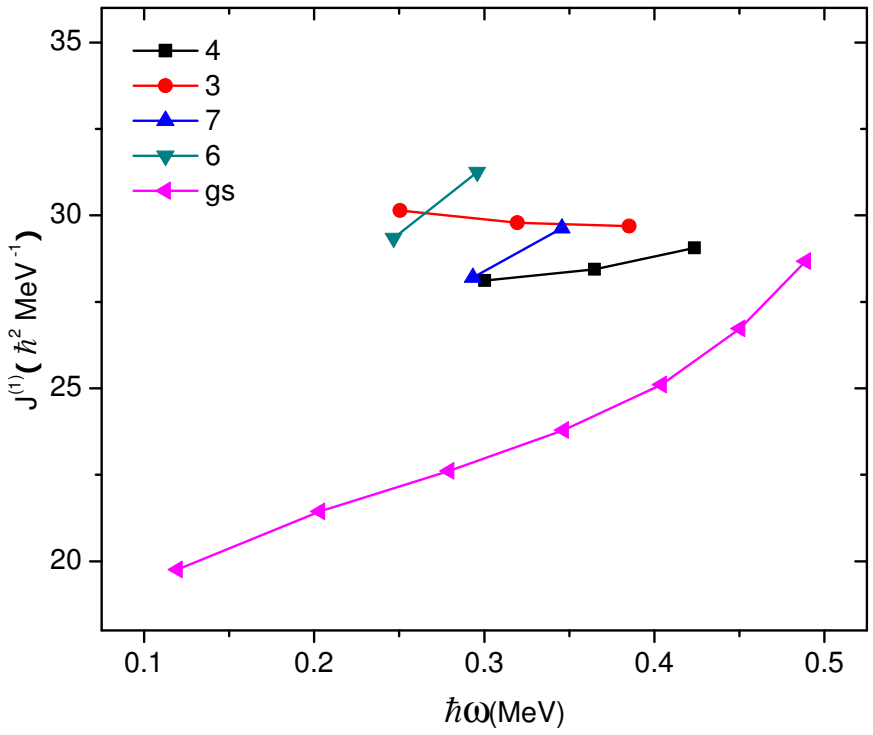

Figure 29: Plot of $J^{(1)}$ vs rotational frequencies for rotational bands in ^{102}Zr.

transitions from Ce partner isotopes are clearly identified. More detailed examination lead to the identification of the 549.4-, 618.4- and 686.2-keV transitions in this band.

Two other rotational bands, labeled as (6) and (7), are observed for the first time as well. The transitions are put in these bands according to their energy relationships and relative intensities. Several previously discovered states [Dur95], arranged into band (8), have been confirmed as well.

Discussion

The properties of the ground-state band was discussed in [Hua04] in very details. Here we present a plot of first kinetic moment of inertia as a function of rotational frequencies of the rotational bands in ^{102}Zr, as shown in Figure 29. The upbending behavior is in agreement with [Hua04], which emerges at about 0.40 MeV. This was explained by alignment of two $h_{11/2}$ neutrons. Band (2) was proposed as built on two-quasi-particle states

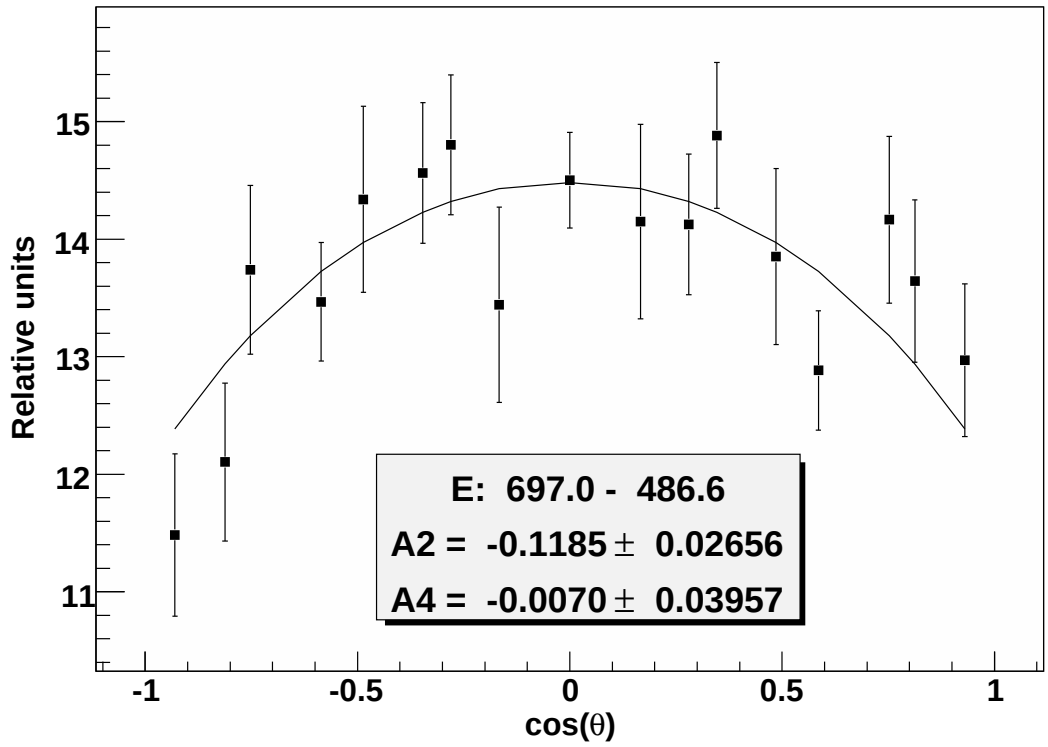

Figure 30: Angular correlation of the 697.0-486.6 keV cascade in ^{102}Zr.

with a configuration of $\nu 5/2^-[532] \otimes \nu 3/2^+[411]$ in [Dur95] and confirmed in [Hua04].

Band (3) was assigned with 5^- to the band-head, 1661.9-keV state in [Dur95] and [Hua04]. This spin/parity assignment is supported by angular correlation measurements from this work. We measured the angular correlation between the 697.0- and 486.6-keV transitions, as shown in Figure 30. The measured angular correlation coefficients are $A_2^{exp} = -0.12(3)$ and $A_4^{exp} = -0.00(3)$. This agrees nicely with a spin configuration of 5(D)6(Q)4, with $A_2^{the} = -0.11$ and $A_4^{the} = 0.0$ at mixing ratio of 0.0. This indicates that the 697.0-keV transition is a pure dipole transition. Therefore, we assign 5^- to the 1661.9-keV state. A similar band is also observed in the neighboring ^{104}Mo nucleus. This assignment agrees with previous work.

For band (4), the angular correlation of the 967.4- and 486.6-keV cascade was measured, as shown in Figure 31. The measured coefficients, $A_2^{exp} = 0.12(4)$ and $A_4^{exp} = 0.03(6)$, suggests that this is a quadrupole-quadrupole cascade. However, in [Hua04], the band head was assigned as 6^-. If the 1932.3 state has a spin of 6^-, we should be able

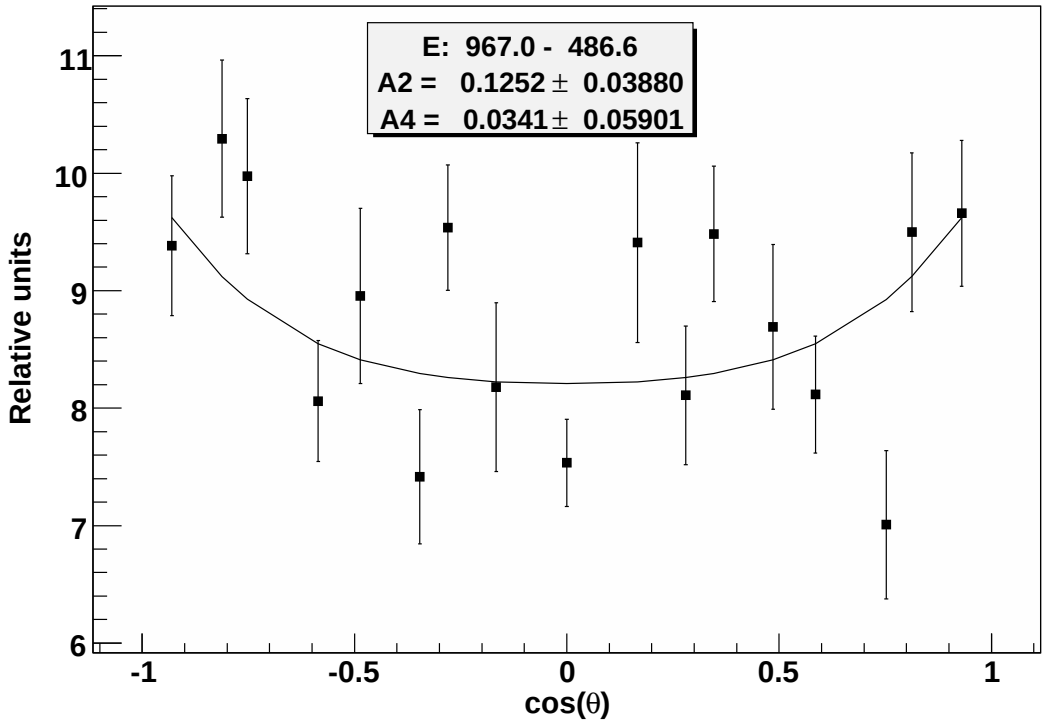

Figure 31: Angular correlation of the 967.4-486.6 keV cascade in ^{102}Zr.

to observe an E1 character for the 967.4 keV transition. From the experimental angular coefficients measured in this work, we propose a spin assignment of 8^+ to the band head state.

For band (6), we measured the angular correlation of the 908.0-326.5 keV cascade, as shown in Figure 32. The measured angular correlation coefficients are: $A_2^{exp} = -0.073(26)$ and $A_4^{exp} = 0.15(4)$. These values agree with a spin configuration of 4(1,2)4(2) at $\delta = -7.0$. Therefore, we assigned 4^+ to the 1386.3-keV state.

Angular correlations of other strong cascades were measured as well. The results is shown in Figure 33, with $A_2^{exp} = -0.075(16)$ and $A_4^{exp} = 0.035(24)$. Note that the 151.8 keV state has a lifetime of 2.76 ns. What we measured is an attenuated correlation. More discussion will be given in the following chapter. The 326.5-151.8 keV cascade was measured with an attenuation factor of 0.54. So for the 1090.4-151.8 keV cascade, an attenuation correction is required for the measured angular correlation coefficients. The corrected experimental angular correlation coefficients are calculated to be

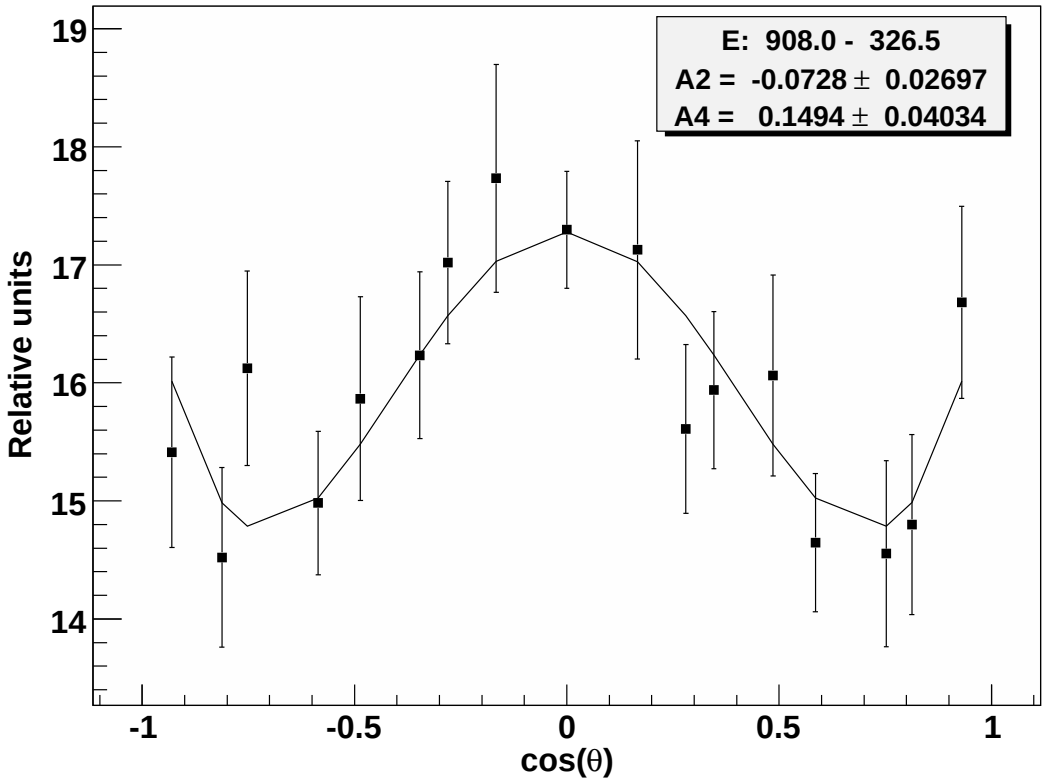

Figure 32: Angular correlation of the 908.0-326.5 keV cascade in ^{102}Zr.

$A_2^{exp}(corrected) = -0.139(30)$ and $A_4^{exp}(corrected) = -0.065(44)$. These values agrees with a spin configuration of 3-2-0 at mixing ratio $\delta \approx 10.0$. We assigned 3^+ to the 1242.2-keV state. The measured angular correlation of the 1090.4-578.6 keV cascade is shown in Figure 34. The experimental angular correlation coefficients, $A_2^{exp} = -0.016(11)$ and $A_4^{exp} = -0.034(16)$, agrees with spin configuration of 4(1,2)3(2)2.

Band (5) is identified for the first time, with one crossing transition to the ground state band. It has similar energy spacing with band (2). A similar band was also identified in the neighboring ^{100}Zr [Hwa06b]. Therefore, we assume that this band is also a two-quasi-particle rotational band, by exciting two neutrons. Only one 1961.5 keV crossing transition is observed. We propose it as an E1 transition and the band head state is assigned 7^-. Band (6) and (7) are assigned with positive parities tentatively, because similar bands have been identified in neighboring even-even Mo nuclei.

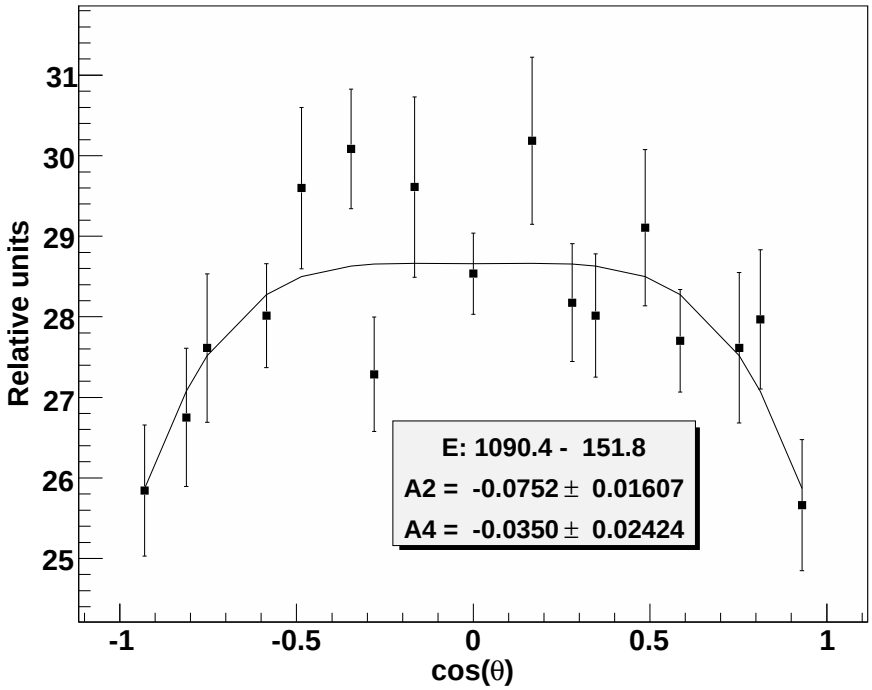

Figure 33: Angular correlation of the 1090.4-151.8 keV cascade in ^{102}Zr.

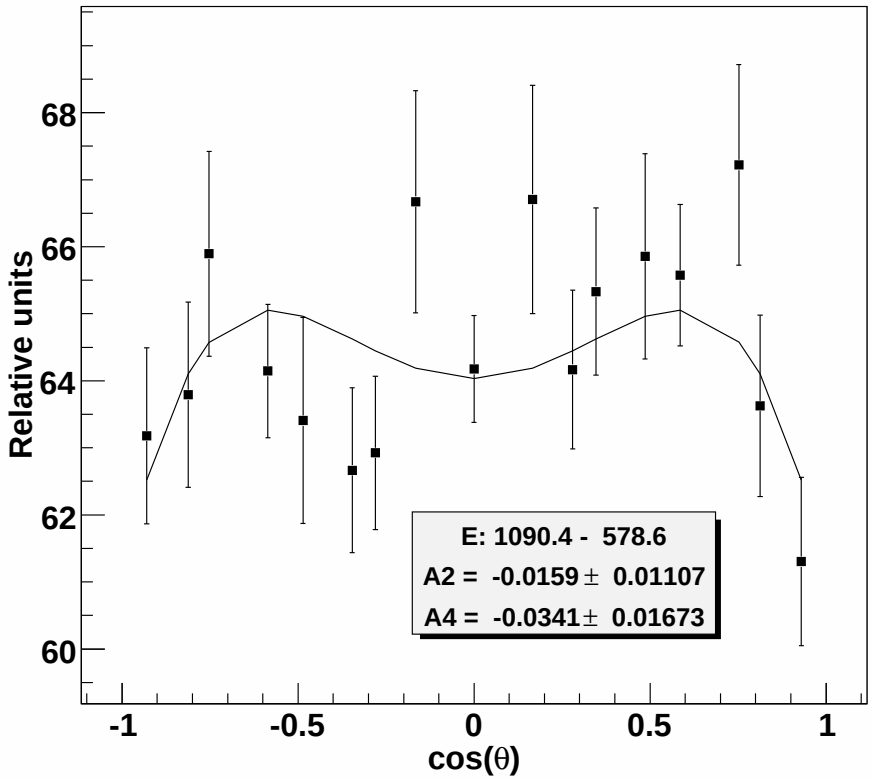

Figure 34: Angular correlation of the 1090.4-578.6 keV cascade in ^{102}Zr.

^{114}Ru

Neutron-rich ^{114}Ru lies between well-deformed double-magic Sr and Zr nuclei ($Z = 38, 40$; $N = 60, 62$) [Ham89] and spherical double-magic ^{132}Sn. Systematic study of the level structures of the nuclei in this region can provide important insight into the nuclear structure characteristics, such as the systematic behavior of nuclear deformation, the deformation driving effects, and the location and characteristics of the $h_{11/2}$ unique-parity intruder configuration. Prior to this work, collective band structures of even-A ^{108,110,112}Ru have been reported [Sha94] [Ham95] [Jia03] [Che04] [Che06] [Zhu08] [Luo08]. The level scheme of ^{114}Ru was first reported by Shannon *et al.* [Sha94], from spontaneous fission of ^{248}Cm. By carrying out variation-after-projection calculations, R. Devi and S. K. Khosa gave a good description of ^{114}Ru up to the 10^+ energy state in the ground band [Dev96]. Here, we report on the observation of new high spin states in ^{114}Ru. The ground-state and the one phonon γ-vibration band have been significantly extended. A two-phonon γ-vibration band is now proposed in ^{114}Ru. Cranked shell model calculation has been performed to describe the properties of these excited states.

Experimental Results

The fission partner of Ru isotopes are Xe. By carefully examining the coincidence relationships and the transition relative intensities, a new level scheme of ^{114}Ru has been constructed, as shown in Figure 35. All transitions reported in [Sha94] were confirmed except the 563.3 keV, $(2^+) \rightarrow 0^+$ transition, placed in parenthesis because it is not seen in the 530.5-631.4 keV gate. The yrast band, labeled (1), is observed with spin up to $14\hbar$, which confirms the previous result reported up to $10\hbar$ in [Sha94]. The band (2) based on the 563.3-keV state was reported as a γ-vibrational band in [Sha94]. Five new transitions were identified in band (2), which defined 5 new levels, assigned (4^+), (6^+), (7^+), (8^+), (9^+), respectively. Figure 36 shows some spectra double-gated on (a) the 443.2- and 709.3-keV transitions, (b) the 265.2-and 298.1-keV transitions, and (c) the 265.2- and 530.5-keV

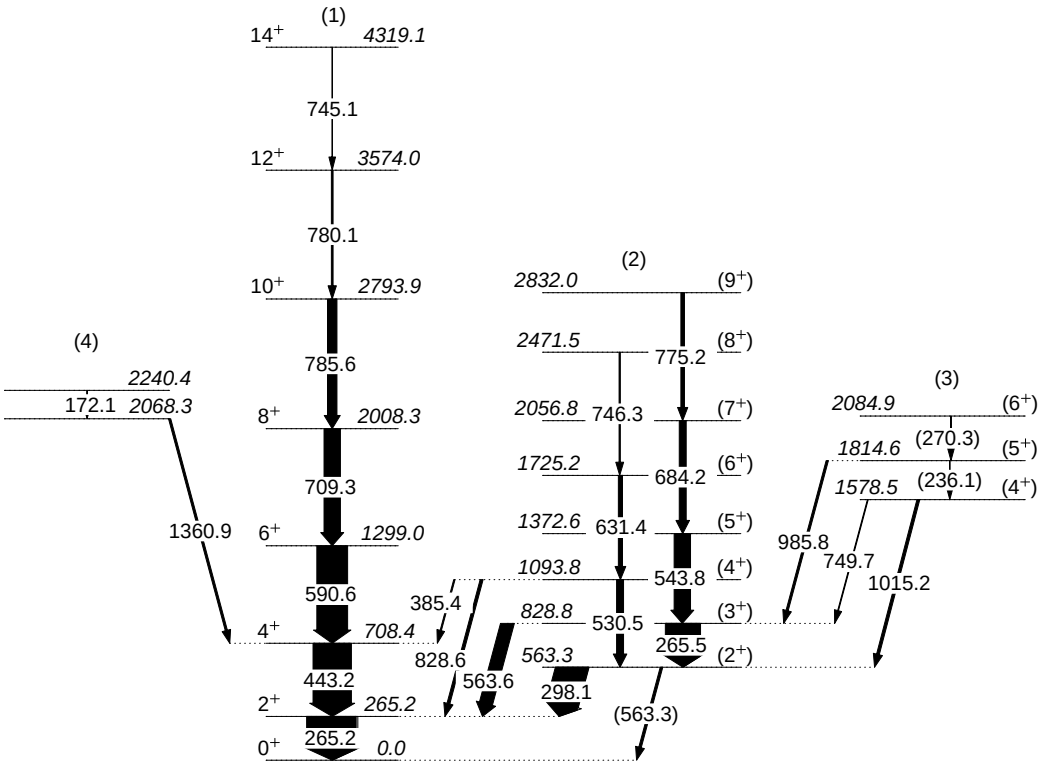

Figure 35: Level Scheme of ^{114}Ru. Energies are in keV.

transitions. The newly identified 785.6-, 780.1-, 745.1-, 530.5-, 631.4-, 746.3-, 684.2-, and 775.2-keV transitions are shown.

Band (3), a possible two-phonon γ-band, has been identified for the first time. Two transitions, 236.1 and 270.3 keV transition are identified in this band. Three crossing transitions from this band to band (2), 1015.2, 749.7, and 985.8 keV transitions are identified. In addition, two excited states, 2068.3 and 2240.4 keV states in band (4), and two crossing transitions, 1360.9 and 172.1 keV transitions are identified. Careful cross-checking in different double gates and measurements of relative intensities lead to the placement of these transitions. The relative intensities of transitions in ^{114}Ru are listed in Table 4.

Discussion

A plot of the kinetic moment of inertia $J^{(1)}$ vs rotational frequency $\hbar\omega$ for band(1) is shown in Figure 37. The backbending (band crossing) observed here for the first time

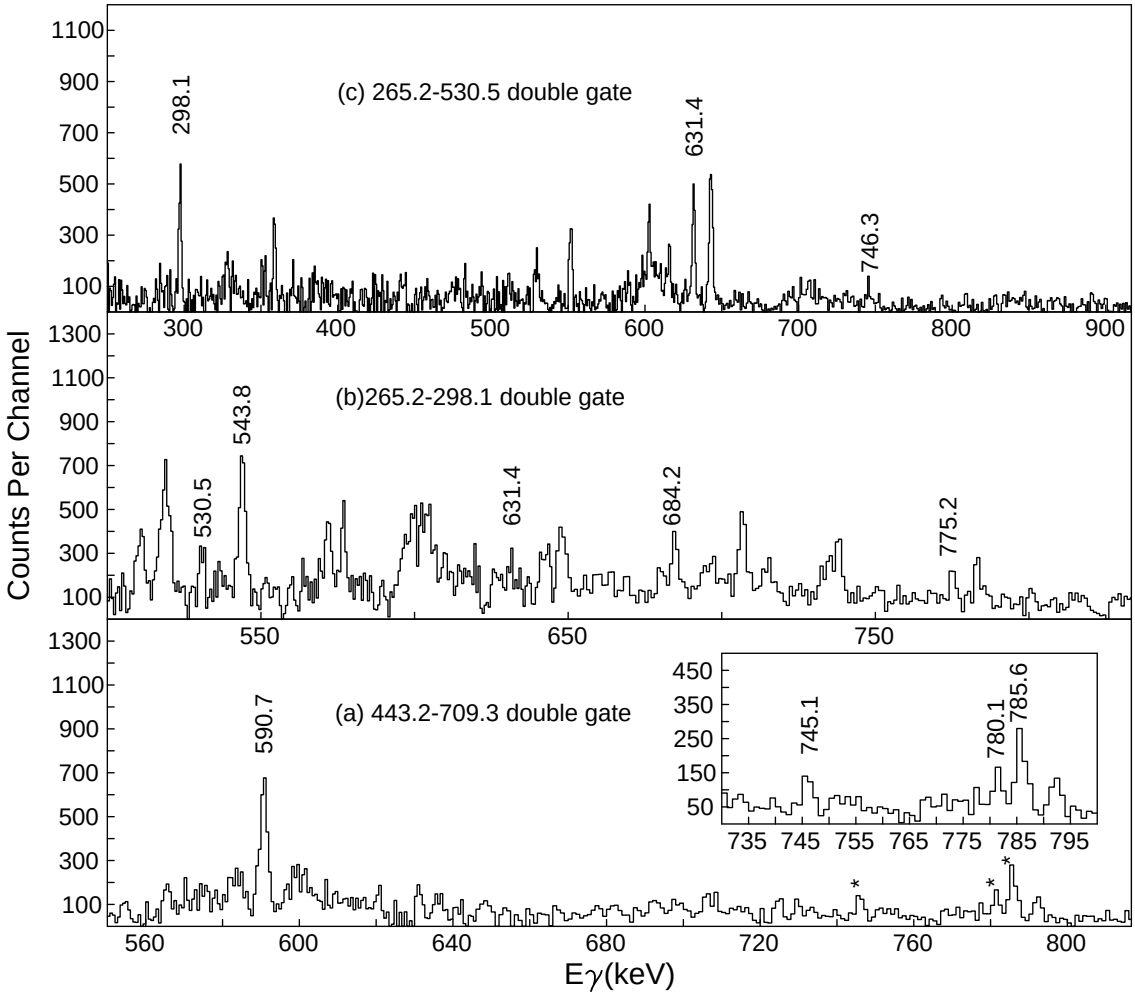

Figure 36: Spectrum double gated on (a) 443.2- and 709.3-keV transitions, (b) 265.2- and 298.1-keV transitions, and (c) 265.2- and 530.5-keV transitions in ^{114}Ru.

Table 4: Relative intensities of γ-rays in ^{114}Ru. The doublet 265.2- and 265.5-keV transitions are estimated with error of 20%.

E_γ (keV)	I_γ (%)	Band	E_i (keV)
172.1	4.6	4	2240.4
236.1	3.2	3	1575.8
265.2	(150)	1	265.2
265.5	(25)	2	828.8
270.3	2.0	3	1814.6
298.1	36.9	2-1	563.3
385.4	2.5	2-1	1093.8
443.2	100	1	708.4
530.5	11.2	2	1093.8
543.8	43.3	2	1372.6
563.6	32.6	2-1	828.8
590.7	68	1	1299.0
631.4	8.4	2	1725.2
684.2	15.9	2	2056.8
709.3	39	1	2008.3
745.1	2.5	1	4319.1
746.3	2.2	2	2471.5
749.7	2.8	3-2	1814.6
775.2	13.0	2	2832.0
780.1	6.8	1	3574.0
785.6	17.5	1	2793.9
828.6	3.1	2-1	1093.8
985.8	8.2	3-2	2084.9
1015.2	6.7	3-2	1578.5
1360.9	6.9	4	2068.3

occurs at a rotational frequency $\hbar\omega \approx 0.4$MeV. This follows the behavior of ^{108}Ru and ^{110}Ru, but differs from ^{112}Ru, which has only a smooth upbending. We performed CSM (Cranked Shell Model) calculation to interpret band structures in ^{114}Ru. The calculated results are presented in Figure 38, where the minima in the total Routhian surfaces (TRS) are found, corresponding to β_2=0.23, γ = -59.4°, β_4 = -0.049 at $\hbar\omega$ = 0.0 MeV, β_2 = 0.24, γ = -49.1°, β_4 = -0.041 at $\hbar\omega$ = 0.3 MeV, and β_2 = 0.23, γ = -52.9°, β_4 = -0.035 at $\hbar\omega$ = 0.5 MeV. The β_2 is nearly constant across the band crossing while γ and β_4 are different. The average values of β_2 and γ are close to 0.23 and -55.0°. This indicates that the ^{114}Ru has oblate deformation in the ground state, and possesses triaxial deformation with increasing rotational frequency. The quasi-particle energies (Routhians) were calculated for ^{114}Ru by using CSM and taking the above calculated β_2 and γ parameters. The Routhians for ^{114}Ru are shown in Figure 39(a) for protons and Figure 39(b) for neutrons, respectively. The calculations predict a band crossing caused by the alignment of two $g_{9/2}$ protons at $\hbar\omega \approx 0.40$MeV, which is in excellent agreement with the experimental data. The band crossing related to the alignment of two $h_{11/2}$ neutrons emerges at $\hbar\omega \approx 0.28$ MeV or $\hbar\omega \approx 0.48$ MeV. Therefore, we believe that the $g_{9/2}$ protons are responsible for the backbending of the ground state band in ^{114}Ru. Note, that in ^{108,110,112}Ru, the backbending in the ground bands are from alignment of two $h_{11/2}$ neutrons. The different contributions of protons and neutrons in $^{108-114}$Ru provide new insights into nuclear structure in this region. More theoretical analysis is required.

Band (2) belongs to a one-phonon γ-vibration band. The 4^+, 6^+, 8^+ and 9^+ levels are added to this band. A plot of ΔE vs. lower energy level spin is shown in Figure 40, as well as those in ^{108,110,112}Ru. The ^{114}Ru staggering is similar to ^{112}Ru. Theoretical calculations [Che04] [Jia03] [Che06] have shown that the staggering of γ-bands in even-even Ru isotopes are from a rigid triaxial shape. This indicates that this may be caused by triaxial deformation for ^{114}Ru. A detailed discussion and comparison can be found in [Zhu08] and [Luo08].

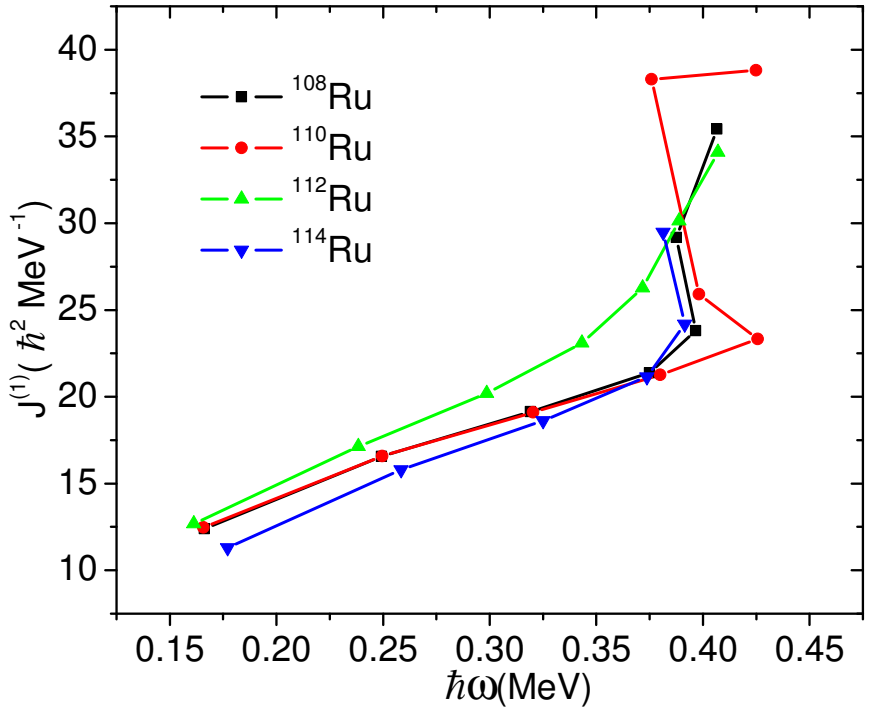

Figure 37: Plot of $J^{(1)}$ vs rotational frequencies for ground-state bands in ^{108,110,112,114}Ru.

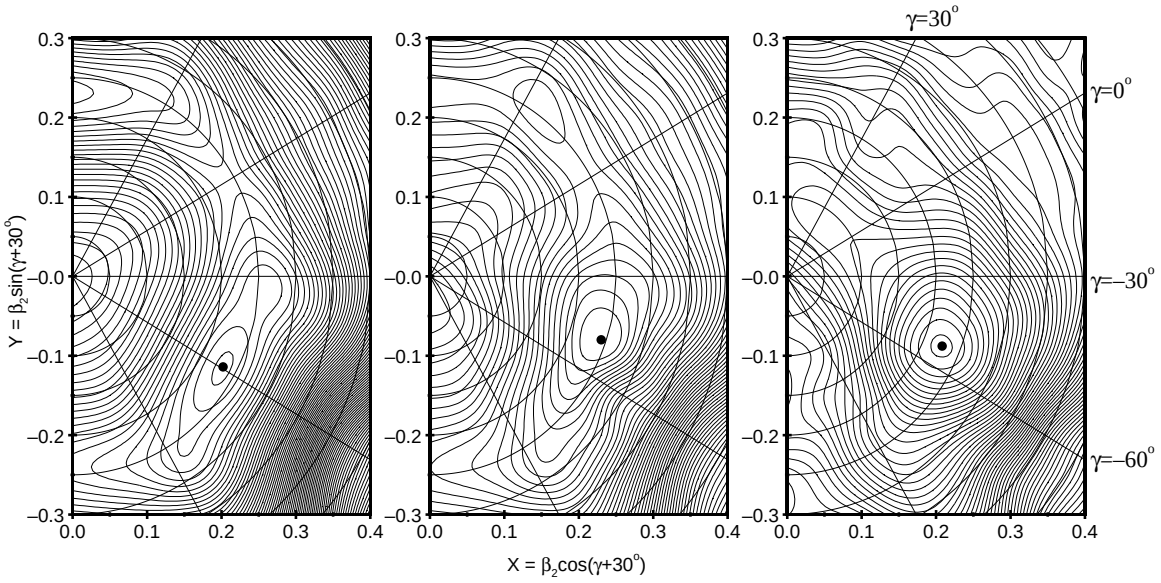

Figure 38: Polar coordinate plots of total Routhian surface (TRS) calculated for ^{114}Ru: (a) $\hbar\omega$ = 0.0 MeV, β_2 = 0.23, γ = -59.4°, β_4= -0.049, (b) $\hbar\omega$ = 0.3 MeV, β_2 = 0.24, γ = -49.1°, β_4 = -0.041, (c) $\hbar\omega$ = 0.5 MeV, β_2 = 0.23, γ = -52.9°, β_4 = -0.035.

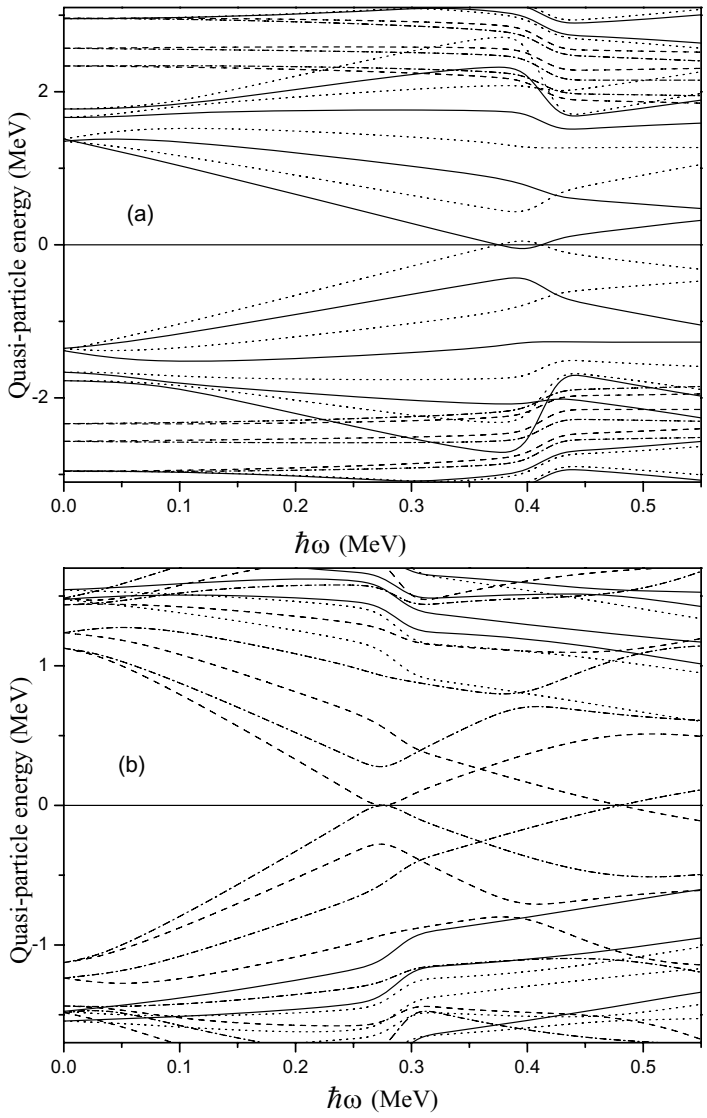

Figure 39: The calculated Routhians for quasi-protons(a) and quasi-neutrons(b) vs rotational frequency $\hbar\omega$ in ^{114}Ru. Solid line: (+,+); Dotted lines: (+,-); Dot-dash lines: (-,+); Dash lines: (-,-).

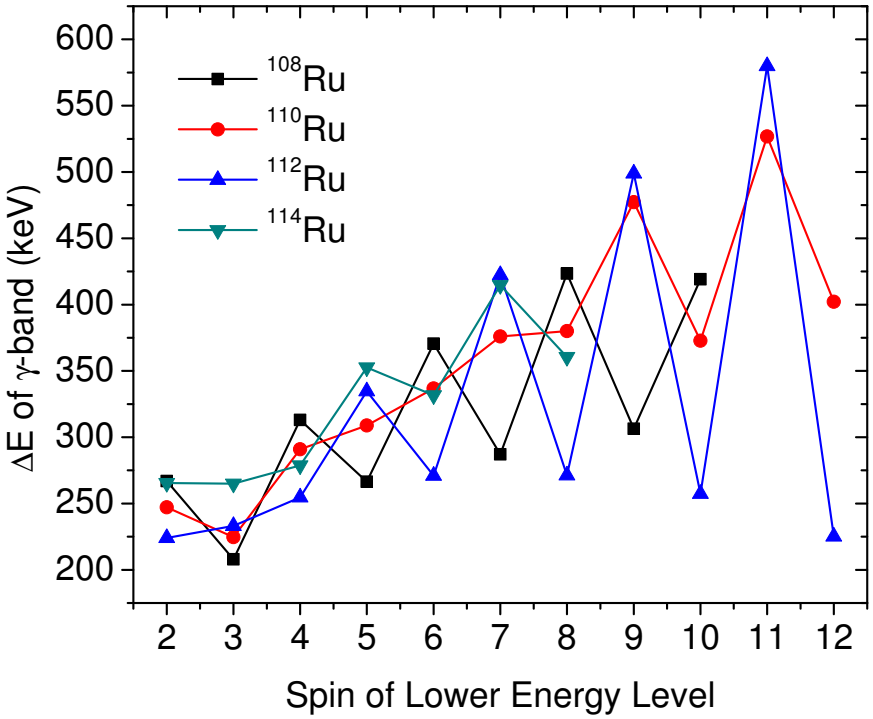

Figure 40: Plot of ΔE vs spin of lower energy level for γ-bands in ^{108,110,112,114}Ru.

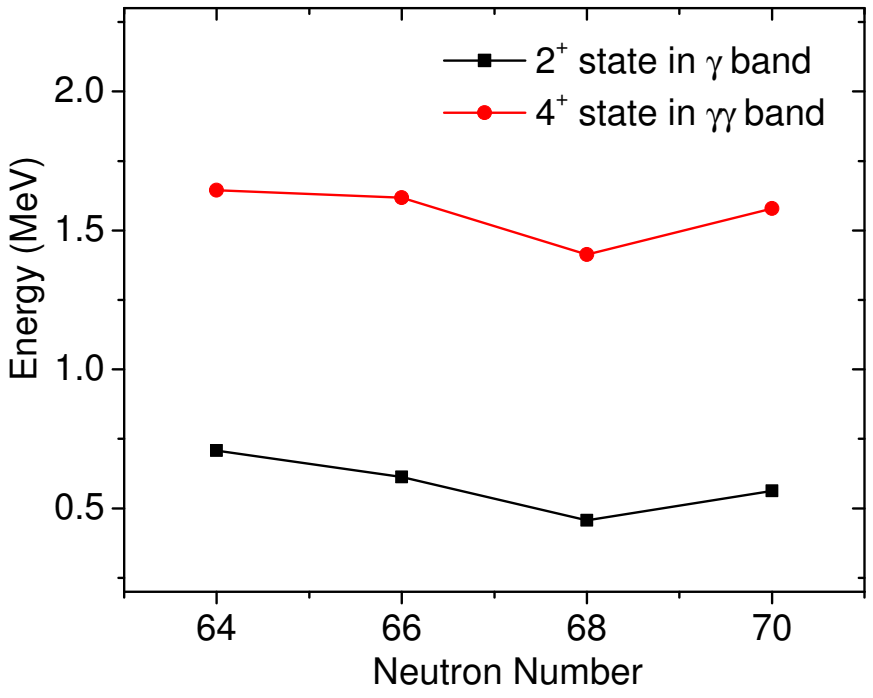

Figure 41: Plot of first excited state energies of one-phonon γ-bands and two-phonon γ-bands in ^{108,110,112,114}Ru.

Band (3) is identified for the first time. In Figure 41 the band head energies in the one-phonon γ bands and two-phonon γ bands in $^{108-112}$Ru are shown, as well as bands (2) and (3) in ^{114}Ru. Band (3) fits nicely as a two-phonon γ-vibration band, with a tentatively assigned 4^+ to the band head level at 1578.5 keV. More theoretical work is required to explain the properties of the ground-state band, γ-band and two-phonon γ-band in ^{114}Ru.

^{137,138}Cs

Beta-decay, (d, p) and (α, xn) reactions [Pra87], thermal neutron capture, and fission have been used to populate the $N = 83$ isotones. Detailed exploration of the high-spin yrast and near-yrast spectroscopy in this region were not realized until the advent of large gamma-detector arrays used in fission experiments [Ham95] [Zha96]. Before the present work, some progress was made at Gammasphere and Eurogam II on the $N = 83$ isotones ^{134}Sb($Z = 51$) [Bha97], ^{135}Te ($Z = 52$) [Bha97] [For01] [Luo01], ^{136}I ($Z = 53$) [Bha97] [Urb06] , ^{137}Xe ($Z = 54$) [Dal99], and ^{139}Ba ($Z = 56$) [Luo01]. The ground state and a number of low-spin states [Car74] and a 6^- isomeric state [LCC71] in ^{138}Cs were reported from β-decay work. However, nothing has been reported for the high-spin states of ^{138}Cs ($Z = 55$). The fission partners of ^{138}Cs are ^{109}Tc ($5n$), ^{110}Tc ($4n$) and ^{111}Tc ($3n$). The level schemes of ^{109,110,111}Tc were reported by Y.X. Luo *et al.* [Luo04] [Luo06] and by W. Urban *et al.* [Urb05].

Identification of Transitions in ^{137,138}Cs

With the above-mentioned Tc identifications achieved, we searched for high-spin states and transitions in ^{138}Cs. By gating on known transitions in ^{109,110,111}Tc isotopes, we identified one 1156.9-keV transition which we assigned to ^{138}Cs. In ^{109,110,111}Tc gates, the yield ratios of the 1156.9-keV transition in ^{138}Cs and the 1184.7-keV transition in ^{137}Cs were measured to be 2.2, 1.1 and 0.3, as shown in Figure 42. The variations of these ratios follow those of ^{144}Ba and ^{143}Ba in ^{103,104,105}Mo gates [TA97], to support that the 1156.9-

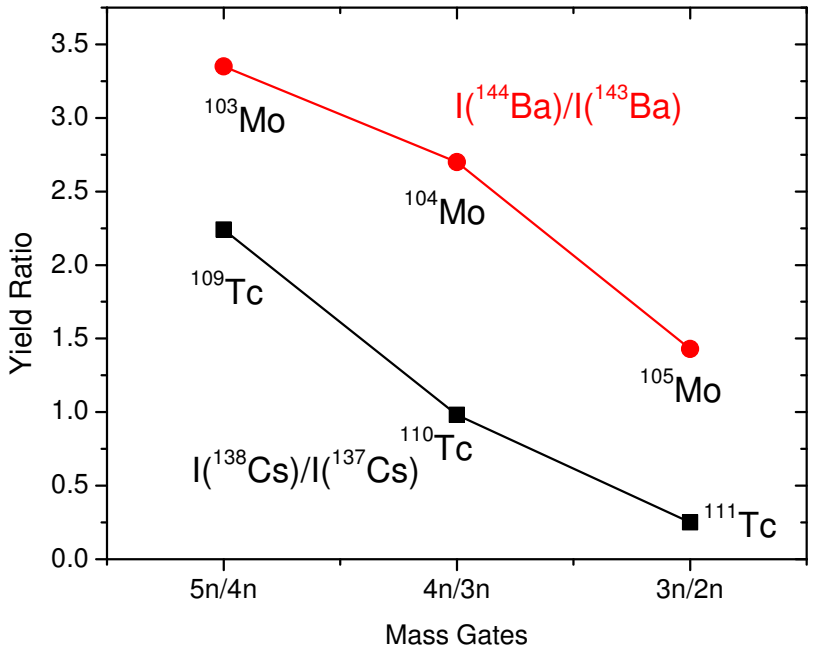

Figure 42: Fission yield ratios of ^{138}Cs and ^{137}Cs in ^{109,110,111}Tc gates, ^{144}Ba and ^{143}Ba in ^{103,104,105}Mo gates [TA97].

keV transition belongs to ^{138}Cs. The fact that the ratios are smaller than those observed in Ba-Mo pairs also suggests that the 1156.9-keV transition is not directly feeding the isomeric state nor the ground state.

In order to show how we identified other transitions in ^{138}Cs, several triple-coincidence spectra were generated by gating on the 1156.9-keV transition in ^{138}Cs and transitions in its partner Tc isotopes. A spectrum double gating on the 1156.9-keV transition in ^{138}Cs and the 137.3-keV transition in ^{109}Tc is shown in Figure 43(a). The coincident γ-ray transitions in both ^{138}Cs and ^{109}Tc were clearly identified. In Figure 43(b), a spectrum double gating on the 1156.9- and 174.5-keV transitions in ^{138}Cs is shown. The coincident transitions of ^{138}Cs and its Tc partners are indicated. Extensive cross-checking with many other triple-coincidence spectra led to identifications and placements of the transitions in ^{138}Cs. We have observed a total of fifteen new transitions and placed them into the level scheme with thirteen new levels, as shown in Figure 44.

The level scheme of ^{138}Cs established is shown in Figure 44. Excited levels are

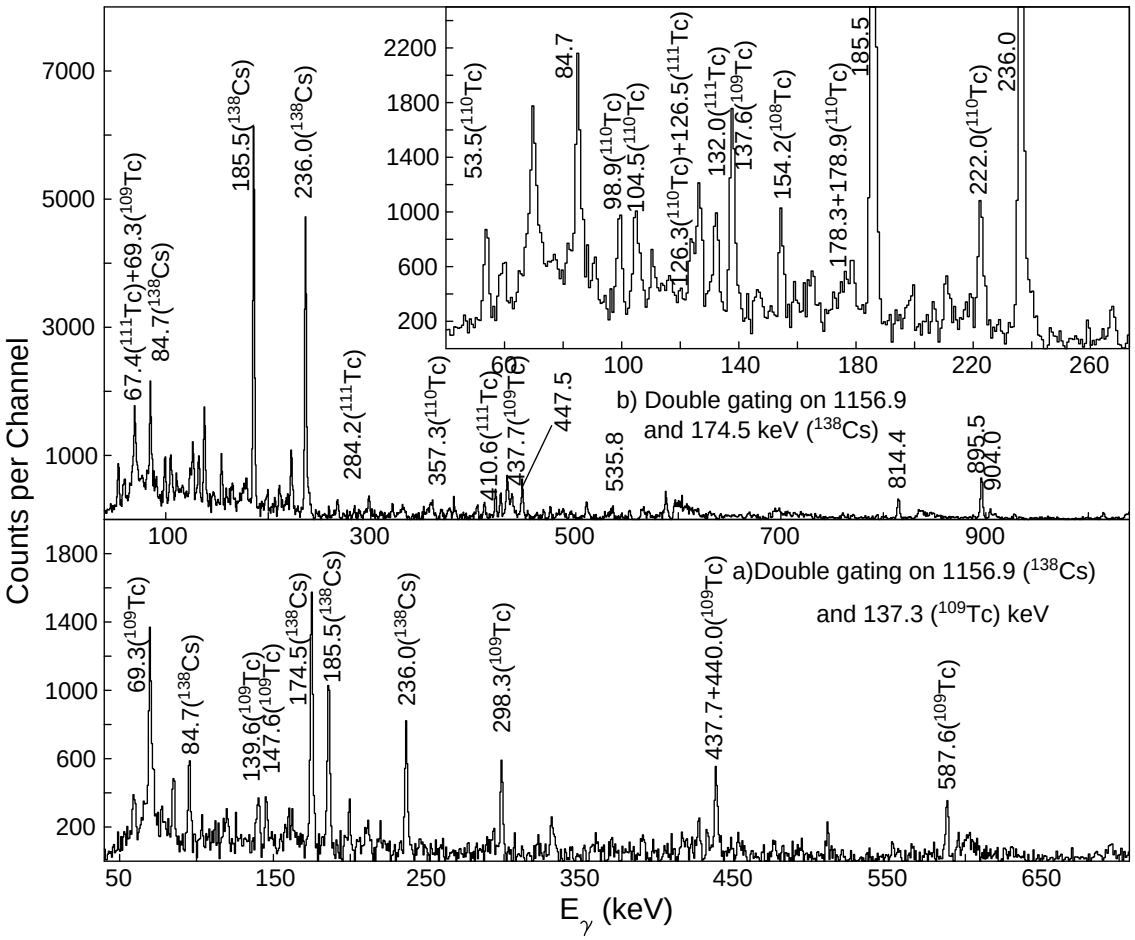

Figure 43: (a) Spectrum gating on the 1156.9-keV transition in ^{138}Cs and the 137.3-keV transition in ^{109}Tc, (b) spectrum gating on the 1156.9- and 174.5-keV transitions in ^{138}Cs.

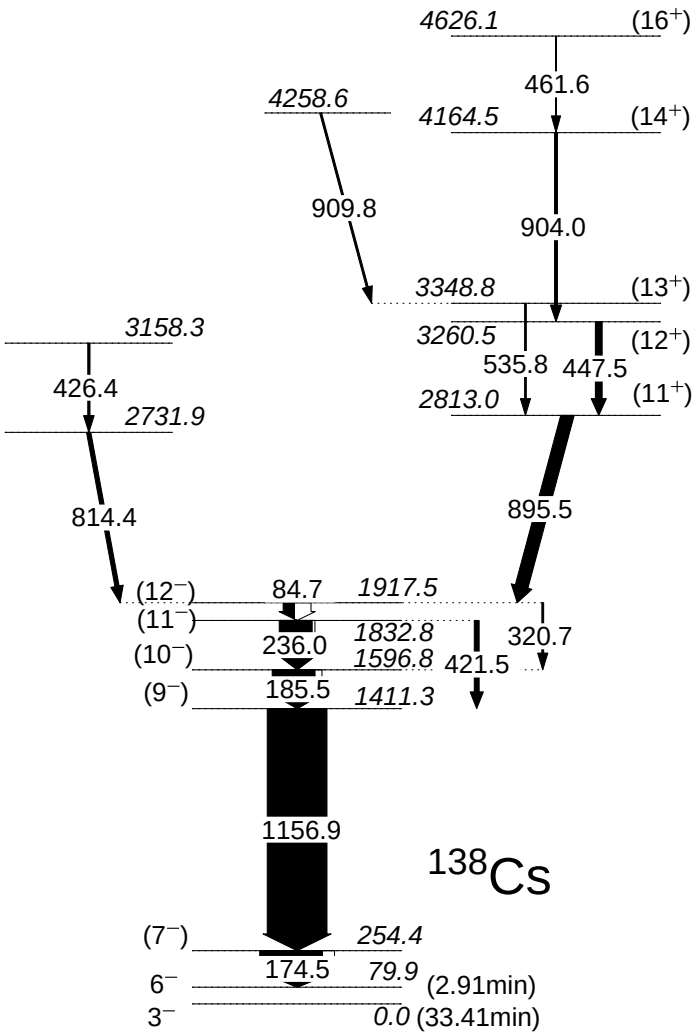

Figure 44: Level Scheme of ^{138}Cs. Energies are in keV.

observed to be populated up to ≈4.63 MeV in ^{138}Cs. The ground state and the 6^- isomeric state in ^{138}Cs were reported in references [Car74] and [LCC71], respectively. For the neighboring $N = 83$ isotone, ^{136}I ($Z = 53$), W. Urban *et al.* reported the 1^- ground state and a 6^- isomeric state [Urb06]. Compared with the level scheme of ^{136}I, it is most likely that the observed yrast cascade of ^{138}Cs in the present work is built on the 79.9 keV 6^- isomeric state. This is supported by the fact that spontaneous fission populates high spin states. Based on the decay patterns, the levels are arranged into different bands.

Total internal conversion coefficients (α_{total}) were measured to determine the multipolarities of the low-energy transitions. The α_{total} of low-energy transitions can be deter-

mined from the intensity balance in and out of a state by double gating on two transitions in the same cascade. The total internal conversion of two low-energy transitions, 185.5- and 84.7- keV were measured. For the 185.5-keV transition, the α_{total} was measured by double gating on the 1156.9- and 84.7- keV transitions. In this gate, the difference in relative γ-ray intensities of the 185.5- and 236.0-keV transitions is equal to the conversion electron intensity. The α_{total} of the 84.7-keV transitions was measured by double gating on 185.5- and 895.5-keV transitions. Their total internal conversion coefficients were determined as: $\alpha_{total}(84.7keV) = 1.39 \pm 0.22$ and $\alpha_{total}(185.5keV) = 0.18 \pm 0.04$. The theoretical values were calculated as $\alpha_{(total,E_2)}(185.5keV) = 0.22$, $\alpha_{(total,M_1)}(185.5keV) = 0.16$, $\alpha_{(total,E_2)}(84.7keV) = 3.42$, and $\alpha_{(total,M_1)}(84.7keV) = 1.48$. Comparing with the theoretical values, their multipolarities were deduced as pure M1 for the 84.7-keV transition, M1 and/or E2 for the 185.5-keV transition.

The level scheme of ^{137}Cs was reported by R. Broda *et al*. [Bro99] from a deep inelastic one-proton-transfer reaction. From our fission data, we confirmed the level scheme of ^{137}Cs with more transitions and levels identified. We observed seven new transitions and placed them into the level scheme with five new levels. An example of the coincidence spectrum for ^{137}Cs obtained by double gating on 1184.7- and 487.1-keV transitions is shown in Figure 45. The transitions in ^{137}Cs and its fission partners can be clearly identified. The level scheme of ^{137}Cs constructed in the present work is shown in Figure 46.

Shell-model calculations

The spin, parity and configuration assignments for ^{137}Cs and ^{138}Cs are essentially based on comparisons of the experimental level energies and that of shell-model calculations. The shell-model calculations were performed by Prof. Covello's group. In these calculations, it is assumed that ^{132}Sn is a closed core and the valence protons occupy the five single-particle (SP) orbits of the 50-82 shell, while for the neutrons the model space included the six orbits of the 82-126 shell. A shell-model Hamiltonian was employed with

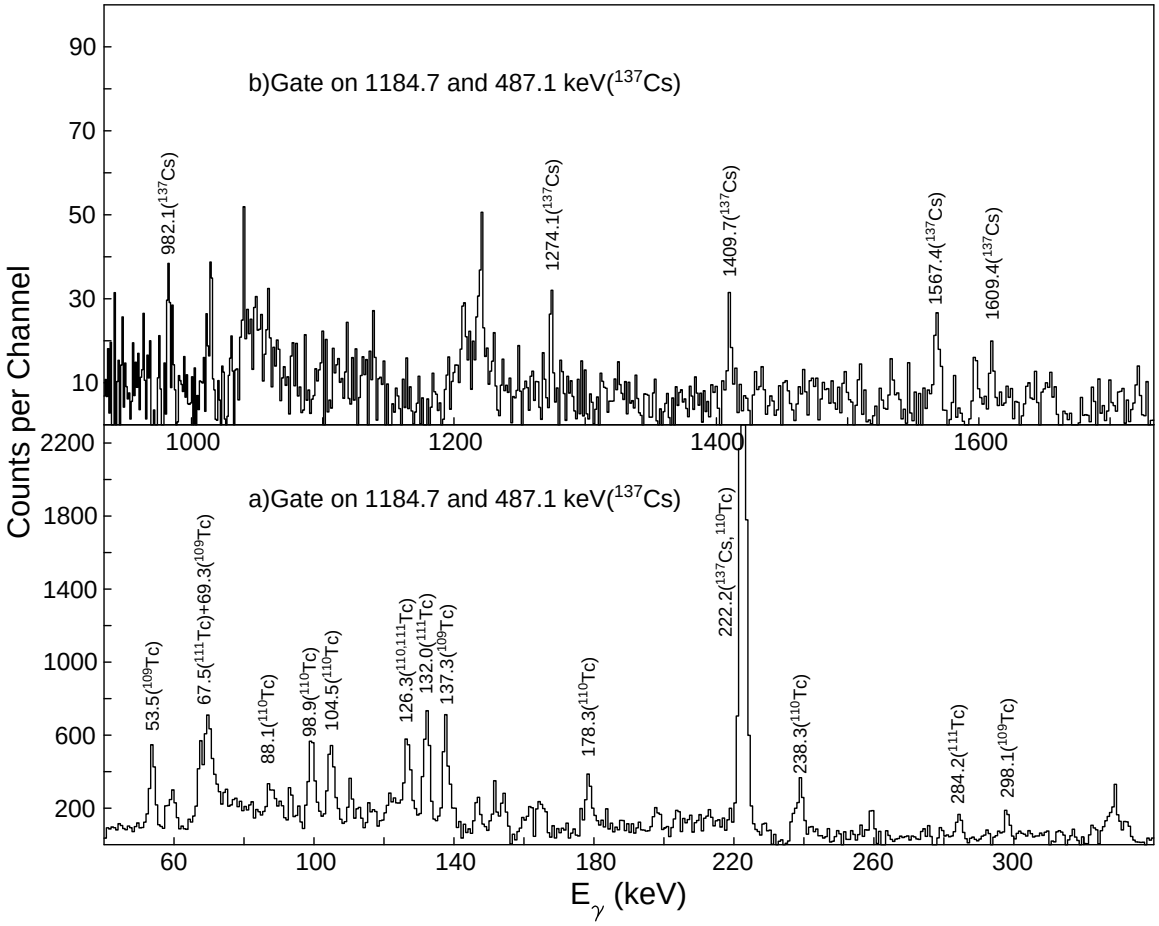

Figure 45: Spectra gating on the 1184.7 keV and 487.1 keV transitions in ^{137}Cs (a) the low energy region, (b) the high energy region.

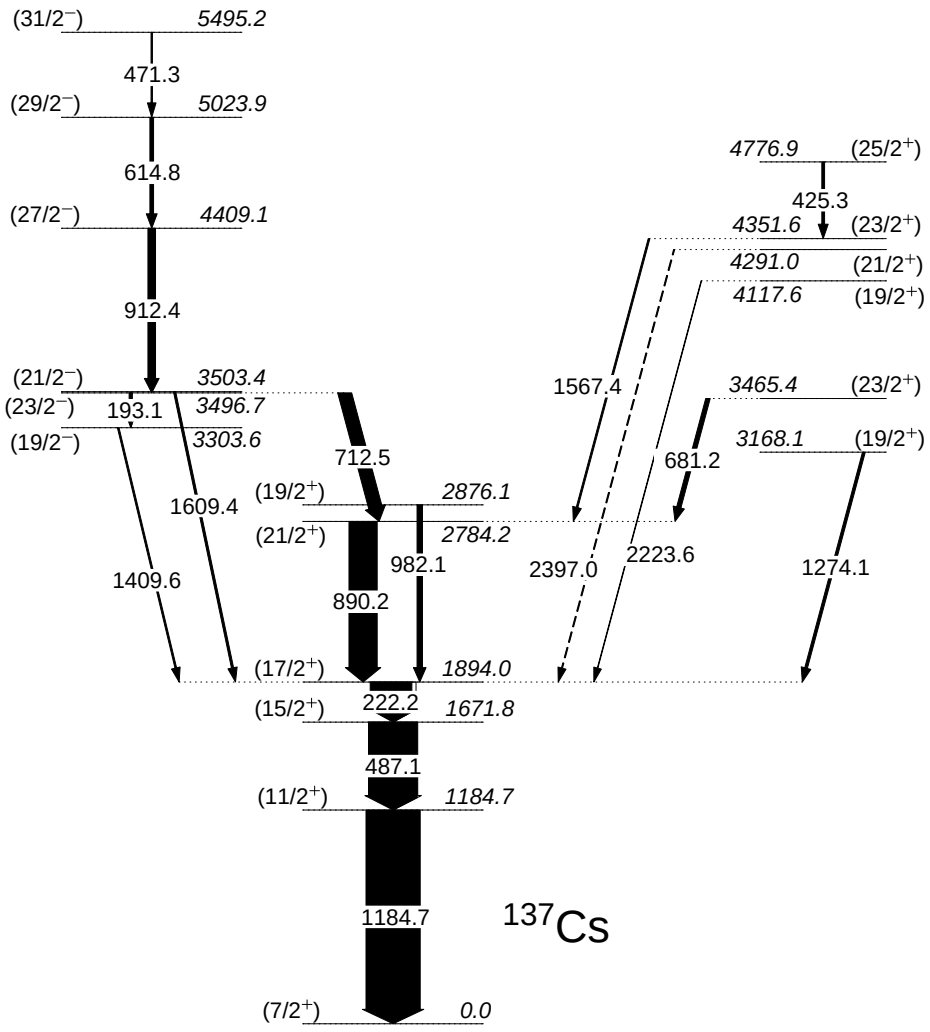

Figure 46: Level Scheme of ^{137}Cs. Energies are in keV.

the single-particle energies taken from experiment and the two-body effective interaction derived from the CD-Bonn free nucleon-nucleon potential [Mac01]. The same Hamiltonian was used in the recent studies of ^{134}Sn, ^{134}Sb, and ^{135}Sb, producing very good results [Cor05] [Cor06] [Cov07]. The values of the proton and neutron SP energies as well as a brief discussion of the derivation of the effective interaction can be found in [Cor05]. Comparisons of the experimental level energies with the shell-model calculations for ^{137}Cs and ^{138}Cs are shown in Table 5 and Table 6, respectively.

The level scheme of ^{138}Cs is built on the isomeric state at 79.9 keV which has been assigned 6^- [LCC71]. The spins, parities, and dominant configurations are assigned by comparing the experimental level energies with the calculated ones which are given in Table 6. The levels in ^{138}Cs can be interpreted by coupling one $f_{7/2}$ neutron to the levels in ^{137}Cs. Based on the shell-model calculations and the above-mentioned multipolarity determinations of low-energy transitions, (7^-), (9^-), (10^-), (11^-) and (12^-) are assigned to the 254.4-, 1411.3-, 1596.8-, 1832.8-, and 1917.5-keV levels, respectively. Note that a (7^-) state and a low-energy transition from (7^-) to (6^-) were also reported in the neighboring $N = 83$ isotone, ^{136}I, by W. Urban *et al* . [Urb06]. In ^{138}Cs, positive parity levels should occur above the 1917.5-keV (12^-) level related to coupling an $f_{7/2}$ neutron to the proton $g_{7/2} \rightarrow h_{11/2}$ and $(g_{7/2})^2 \rightarrow d_{5/2}h_{11/2}$ negative-parity excitations found in ^{137}Cs. By considering the corresponding couplings, (11^+), (12^+), (13^+), (14^+), and (16^+) are tentatively assigned to the 2813.0-, 3260.5-, 3348.8-, 4164.5-, and 4626.1-keV levels, respectively.

The angular correlation coefficients A_2^{exp} and A_4^{exp} for the 174.5- and 1156.9-keV cascade were measured to be -0.07(1) and -0.02(2), as described in [Dan07]. They are consistent with the theoretical coefficients of $A_2^{the} = -0.071$ and $A_4^{the} = 0.0$ [Tay71], for pure quadruple and pure dipole transitions and for the proposed spin assignments of (9^-) and (7^-) to the 1411.3 and 254.4 keV levels. This measurement also indicates that the 174.5-keV transition has M1 character while the 1156.9-keV transitions has E2 character.

The shell-model calculations indicate an important role played by the coupling of

Table 5: Comparison of the experimental level energies of ^{137}Cs with those calculated by the shell-model. Deviations between the theory and experiment are shown in the table. Energies are in MeV.

I^π	E_{exp}	E_{the}	$\Delta = E_{the} - E_{exp}$	Leading component
$7/2^+$	0.00	0.00	0.00	$\pi g_{7/2}^5$
$(11/2^+)$	1.18	1.35	0.17	$\pi g_{7/2}^5$
$(15/2^+)$	1.67	1.68	0.01	$\pi g_{7/2}^5$
$(17/2^+)$	1.89	2.02	0.13	$\pi g_{7/2}^4 d_{5/2}$
$(21/2^+)$	2.78	3.01	0.23	$\pi g_{7/2}^4 d_{5/2}$
$(19/2^+)$	2.88	3.07	0.19	$\pi g_{7/2}^4 d_{5/2}$
$(19/2^+)$	3.17	3.51	0.34	$\pi g_{7/2}^3 d_{5/2}^2$
$(23/2^+)$	3.47	3.75	0.28	$\pi g_{7/2}^3 d_{11/2}^2$
$(19/2^-)$	3.30	3.29	-0.01	$\pi g_{7/2}^4 h_{11/2}$
$(23/2^-)$	3.50	3.40	-0.10	$\pi g_{7/2}^4 h_{11/2}$
$(21/2^-)$	3.50	3.40	-0.10	$\pi g_{7/2}^4 h_{11/2}$
$(27/2^-)$	4.41	4.40	-0.01	$\pi g_{7/2}^4 h_{11/2}$
$(29/2^-)$	5.02	5.22	0.20	$\pi g_{7/2}^3 d_{5/2} h_{11/2}$
$(31/2^-)$	5.50	5.36	-0.14	$\pi g_{7/2}^3 d_{5/2} h_{11/2}$
$(19/2^+)$	4.12			$\pi g_{7/2}^5 \nu f_{7/2} h^{-1}{}_{11/2}$
$(21/2^+)$	4.29			$\pi g_{7/2}^5 \nu f_{7/2} h^{-1}{}_{11/2}$
$(23/2^+)$	4.35			$\pi g_{7/2}^5 \nu f_{7/2} h^{-1}{}_{11/2}$
$(25/2^+)$	4.78			$\pi g_{7/2}^5 \nu f_{7/2} h^{-1}{}_{11/2}$

Table 6: Comparison of the experimental level energies of ^{138}Cs with those calculated by the shell-model. Both experimental and calculated energies are relative to the 6^- state. Deviations between the theory and experiment are shown. Energies are in MeV.

I^π	E_{exp}	E_{the}	$\Delta = E_{the} - E_{exp}$	Leading component	percentage
6^-	0.0	0.0	0	$\pi g_{7/2}^5 \nu f_{7/2}$	46
7^-	0.17	0.15	-0.02	$\pi g_{7/2}^5 \nu f_{7/2}$	41
9^-	1.33	1.55	0.22	$\pi g_{7/2}^5 \nu f_{7/2}$	51
10^-	1.52	1.75	0.23	$\pi g_{7/2}^4 d_{5/2} \nu f_{7/2}$	80
11^-	1.75	1.89	0.14	$\pi g_{7/2}^4 d_{5/2} \nu f_{7/2}$	57
12^-	1.84	1.98	0.14	$\pi g_{7/2}^4 d_{5/2} \nu f_{7/2}$	77
11^+	2.73	2.79	0.06	$\pi g_{7/2}^4 h_{11/2} \nu f_{7/2}$	61
12^+	3.18	3.25	0.07	$\pi g_{7/2}^4 h_{11/2} \nu f_{7/2}$	61
13^+	3.27	3.33	0.06	$\pi g_{7/2}^4 h_{11/2} \nu f_{7/2}$	63
14^+	4.08	3.80	-0.28	$\pi g_{7/2}^3 d_{5/2} h_{11/2} \nu f_{7/2}$	81
16^+	4.55	4.63	0.08	$\pi g_{7/2}^3 d_{5/2} h_{11/2} \nu f_{7/2}$	79

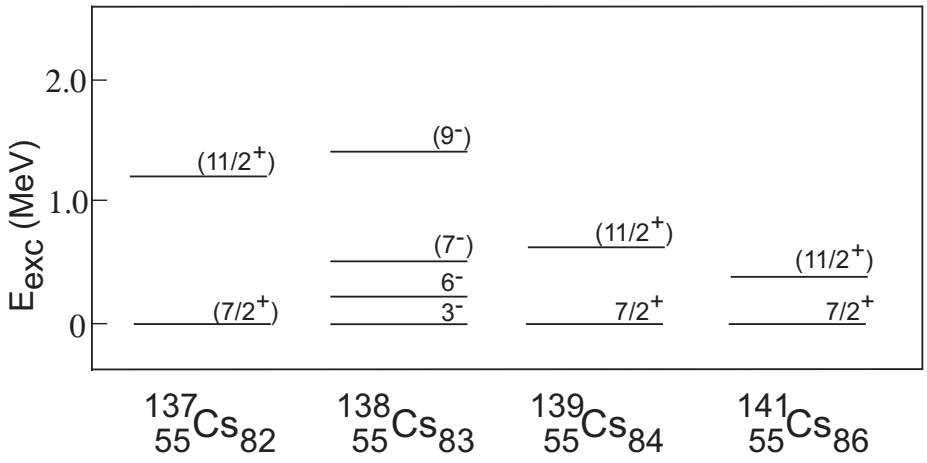

Figure 47: Yrast states of Cs isotopes.

the odd protons outside the $Z = 50$ closed shell and the $f_{7/2}$ neutron outside the $N = 82$ closed shell. It can be also noted in Table 6 that the configuration mixing in ^{138}Cs is extensive. We show only the leading components and their percentages of the total theoretical wave function.

Discussion

Figure 47 shows the yrast excitations of Cs isotopes near the $N = 82$ major shell closure. The level spacings exhibit strong shell effects of the $N = 82$ neutron major shell. The level schemes of ^{140,142}Cs are not included since the spins and parities of their yrast states are not available.

Figure 48 shows the yrast excitations of the $N = 82$ and $N = 83$ isotones with a few valence protons outside the $Z = 50$ major shell closure. A similarity is seen in the yrast level patterns between ^{137}Cs ($Z = 55$) and its neighboring $N = 82$ isotone ^{135}I ($Z = 53$) [Sah01]. For the $N = 83$ isotones ^{138}Cs and ^{136}I [Bha97] [Luo02] [Urb06], a similar cascade pattern is observed. However, one more yrast state, the 10^- state, is identified in ^{138}Cs but not reported in ^{136}I. For the ^{136}I nucleus, the 47s 6^- isomeric state was assigned a configuration of $\pi g_{7/2}^2 d_{5/2} \nu f_{7/2}$ by Urban *et al* [Urb06]. The assignment was supported by shell model calculations of the SMPN(400) set of two-body matrix, in which

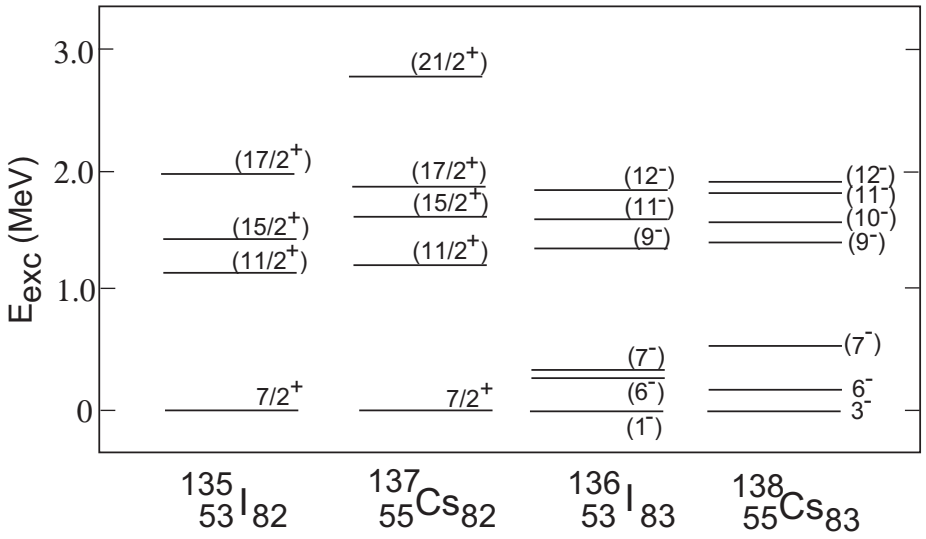

Figure 48: Yrast states of $N = 82$ and $N = 83$ isotones.

the position of the $\pi d_{5/2}$ orbital was lowered by 400 keV. In our shell-model calculations of ^{138}Cs, we predict a yrast 6^- state in ^{138}Cs arising from the $\pi g_{7/2}^5 \nu f_{7/2}$ configuration while a second 6^- state predicted at 185 keV higher is dominated by the $\pi g_{7/2}^4 d_{5/2} \nu f_{7/2}$ configuration. When we similarly lower the $\pi d_{5/2}$ orbital energy, we observe a reordering of the two 6^- states. However, the level ordering of the 9^-, 10^-, 11^-, 12^- levels change too, resulting in significant disagreement between the calculated and experimental level energies. Based on this disagreement, we assigned the 6^- state in ^{138}Cs with a configuration of $\pi g_{7/2}^5 \nu f_{7/2}$. Note that the shell-model calculations on ^{136}I by the Covello group predict a same $\pi g_{7/2}^3 \nu f_{7/2}$ dominant configuration for the lowest 6^- state and the existence of a 10^- state at about the same energy as that calculated for ^{138}Cs. Further studies are needed to verify these predictions.

The variations of the excitation energies of the $11/2^+$ state in even-N Cs isotopes versus the excitation energies of the first 2^+ state in the corresponding even-even Xe core are shown in Figure 49. They change very rapidly in the region of $N = 82$ major shell, with an almost linear relationship. The $N = 83$ Cs isotone ^{138}Cs is also shown in the figure by assuming that the 9^- state can be attributed to the coupling between the lowest yrast

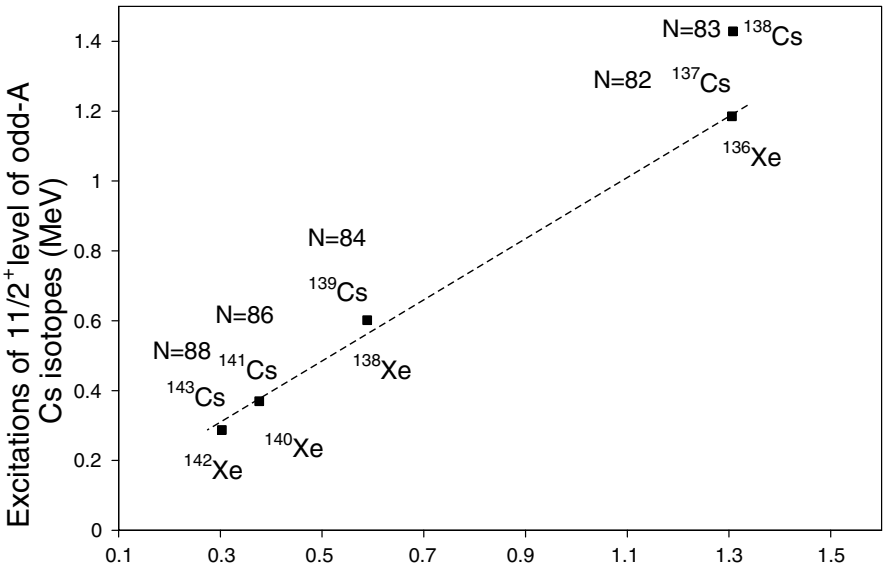

Figure 49: Variations of excitation energies of the $11/2^+$ states in the even-N Cs isotopes versus the excitations of the first 2^+ state in the corresponding even-even Xe core. The 9^- state energy in ^{138}Cs is also shown.

excitation of the even-even core ^{136}Xe with one $g_{7/2}$ valence proton and one $f_{7/2}$ valence neutron. For ^{138}Cs, the coupling does not significantly reduce the excitation energy of the corresponding 9^- state.

Conclusions

In this chapter, by analyzing our 2000 binary fission data, structure of several neutron-rich nuclei were studied. The level scheme of ^{88}Kr was extended to a 7169.4-keV state, with spins and parities assigned by the systematics in comparing with its neighboring $N = 52$ isotones, ^{86}Se and ^{90}Sr. The level scheme of ^{90}Kr was extended, with several new transitions and states identified. Angular correlation measurements confirmed the 3^- assignment to the 1506.7-keV level in ^{90}Kr, in agreement with [RU00]. The lack of systematics in the $N = 54$ isotones, ^{90}Kr and ^{92}Sr, provides insight into this region and indicates the requirement of further experimental and theoretical investigation. A few new transitions were observed in ^{92}Kr as well. No new transition or state was identified in ^{94}Kr, due

to its low yield. In ^{102}Zr, three new collective band structures were identified. Angular correlation measurements were performed to assign spins and parities. In the neutron-rich ^{114}Ru, the ground-state band and γ-band were extended. A new band was identified and proposed as a two-phonon γ-band, by comparing band-head energies with its neighboring even-even Ru isotopes. Cranked Shell Model calculations indicate that the band-crossing of the ground-state band in ^{114}Ru is from the alignment of two $g_{9/2}$ protons, instead of alignment of two $h_{11/2}$ neutrons as found in $^{108-112}$Ru. The staggering pattern of the γ-band indicates a rigid triaxial shape in ^{114}Ru. The level scheme of ^{138}Cs was constructed for the first time in this work, with that of ^{137}Cs extended with several new transitions. Spins, parities and configurations were assigned to the levels of ^{138}Cs based on total internal conversion coefficient measurements of the low-energy transitions, shell-model calculations, angular correlation measurements and level systematics. Shell Model calculations were performed with results in agreement with experimental data. Similarities were observed for the $N = 82$ isotones, ^{137}Cs and ^{135}I as well as the $N = 83$ isotones, ^{138}Cs and ^{136}I. The Shell-Model calculations indicate the important role played by the coupling between the excitation of the fifth proton outside the $Z = 50$ major shell and the $f_{7/2}$ neutron outside the $N = 82$ major shell.

CHAPTER IV

GAMMA-RAY ANGULAR CORRELATION AND G-FACTOR MEASUREMENTS

Measurement of the angular correlations between successive nuclear de-excitations can be used to determine certain properties of the nuclear structure. From angular correlations of prompt cascade, one can extract information on the spins of the energy levels and the multipole mixing ratios of the transitions. Another important property that can be measured with angular correlations is the g-factor of an excited state, with external applied magnetic field or hyperfine field. The g-factors of excited states in even-even nuclei (and their deviation from Z/A) give some sense of their degree of collectivity; for odd A nuclei, the g-factor is related to the purity of the single particle state that characterizes the level.

The analysis of γ-ray angular correlations and g-factor measurements were based on our 2000 binary fission data. The ^{252}Cf source were sandwiched between two Fe foils, which were used to stop fission fragments. Angular correlations of γ-rays in delayed cascade are perturbed, with attenuation factors which are related to the magnetic moments of the intermediate states. No attenuation would be observed for prompt cascades. The Gammasphere detector array, consists of 110 detectors at full capacity, supplies a great opportunity to perform angular correlation measurements and g-factor measurements. A new technique has been developed to identify transitions in nuclei of interest and measure angular correlations of prompt and delayed cascades [Dan07].

Theoretical Predictions of g-factors

The Nuclear Shell Model

The Nuclear Shell Model was introduced in the mid twentieth century by Mayer and Jensen [May55]. In this model, the particles move in a collective central potential

generated by themselves. One of the most realistic potentials is the central Woods-Saxon potential

$$V(r) = -\frac{V_0}{1 + exp(\frac{r-R}{a})}, \tag{1}$$

where V_0 is the depth of the potential well ($\sim$ 50 MeV), R is the mean radius ($R = 1.25A^{1/3}fm$), r is the radial distance and a the diffusivity parameter (0.524 fm). An alternative description can be obtained by using the harmonic oscillator potential with a finite boundary at the nuclear radius and with the inclusion of a centrifugal term proportional to l^2. Both potentials predict discrete shells holding only a finite number of nucleons, but to reproduce the shell number inferred from experimental evidence, the inclusion of a spin-orbit interaction is required, which is in the form of

$$V_{so} = -V_0(r)\boldsymbol{l} \cdot \boldsymbol{s}, \tag{2}$$

where V_0 is the central nuclear potential, ***l*** is the orbital angular momentum and ***s*** is the spin. The spin-orbit interaction causes the individual energy levels to split in a way that the nuclear numbers 2, 8, 20, 28, 50, 82, 126, referred to as *"magic numbers"*, are all reproduced. Figure 50 shows the standard shell model energy levels and orbitals. Shell Model has proven very successful in describing the properties of magic nuclei with few valence nucleons lying outside major shell closures, such as energy levels, electromagnetic transition probabilities and moments, beta-decay rates and reaction cross sections.

The calculation of magnetic moments in the shell model can be greatly simplified for certain nuclei. The paring force, which has a tendency to couple pairs of neutrons and pairs of protons, can be used to described an odd-A nucleus as an inert "core" with one valence nucleon. Therefore, the A-1 nucleons of the core couple into zero-spin combinations that do not contribute to the magnetic moment. So the magnetic moment of the entire nucleus is given by the single, valence nucleon. The only non-zero contribution comes from the single valence nucleon. Equation 7 thus is reduced to either $I = l + \frac{1}{2}$ or $I = l - \frac{1}{2}$, to reflect the two available intrinsic-spin states of the unpaired nucleon. The g-factors for

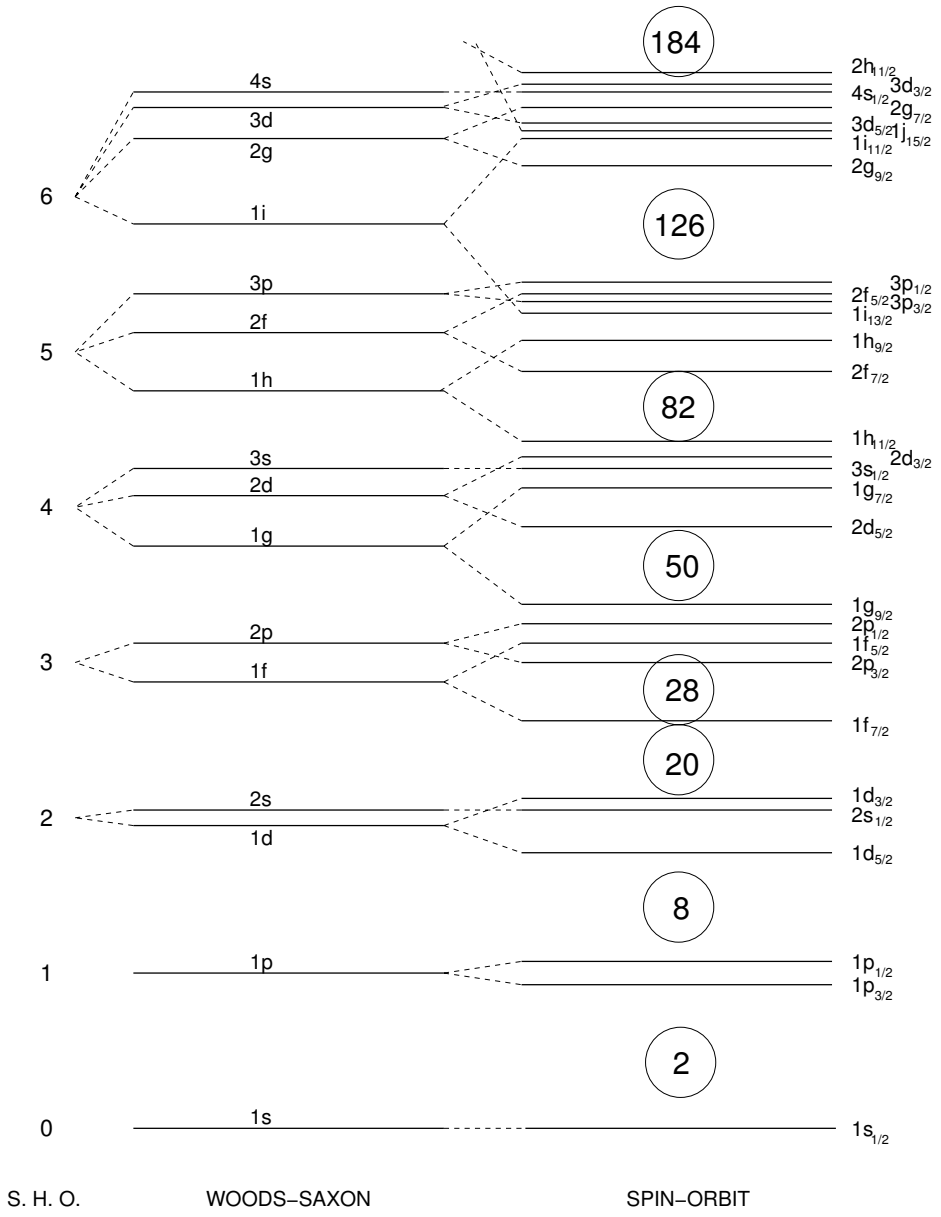

Figure 50: The orbitals generated by the simple Harmonic Oscillator, simple Wood-Saxon and corrected Wood-Saxon potentials. The split induced by the spin-orbit correction is necessary to generate the appropriate shell-model magic numbers.

these two possible states can be written as

$$g = \frac{g_s + (2I-1)g_l}{2I} \quad for \quad I = l + \frac{1}{2}$$
$$g = \frac{-g_s + (2I+3)g_l}{2I+1} \quad for \quad I = l - \frac{1}{2} \tag{3}$$

and are commonly referred as Schmidt g-factors [Sch37]. For nuclei far from the major shell closures, the magnetic effects of the core cannot be ignored and the magnetic moment is written as

$$\mu = [g_c J_c + \sum_i (g_{l_i} l_i + g_{s_i} s_i)] \frac{\mu_N}{\hbar} \tag{4}$$

where g_c, J_c are properties of the core and the many-body problem is thus reduced to a sum over a small number, i, of valence particles. With the introduction of residual interactions, it is necessary to acknowledge contributions from many coupled states and this requires calculations that involve the correct vector coupling of different spins and angular momenta.

Qualitative arguments based on simple shell theory also explain the origin of g-factors in even-even nuclei. One example is the experimentally measured g-factors in Zr isotopes beyond the $N = 50$ shell closure. If $Z = 40$ is taken to be a strong sub-shell closure, $^{90}_{40}\mathrm{Zr}_{50}$ is then a doubly-magic nucleus. Therefore, even-even Zr isotopes just beyond this double shell should be dominated by neutron orbitals. Since neutrons produce a measurable negative magnetic moment, the g-factors are expected to be take on negative values. This has been confirmed by the negative measured $g(2^+)$ values of ^{92}Zr and ^{94}Zr [Smi04].

A successful extension to the shell model is the Nilson Model which describes single particle states in a deformed nuclear potential as opposed to the spherically symmetric formulations of the conventional shell model. Nuclear shape deformation is an intrinsic assumption made in collective nuclear models.

The Collective Model

Collective excitations originate from the co-operative behavior of all or at least a large fraction of the nucleons. Nearly all nuclei with neutron number at mid shell between two major magic numbers show some degree of collective behavior. In even-even nuclei, strong indicators are, for example, the ratios of the lowest 4^+- to 2^+-state energies and 2^+ state electric quadrupole moments. They are both linked to one of the most common forms of collectivity, rotational nuclear motion.

Evidence of rotational and vibrational collectivity is shown in Figure 51, where the ratios of the energies of the first 4^+ and 2^+ are shown. The classical kinetic energy of a rotating object is

$$E = \frac{1}{2}\mathcal{I}\omega^2 \tag{5}$$

where $\mathcal{I}$ is the moment of inertia and the angular momentum is given by $l = \mathcal{I}\omega$. Using the appropriate quantum mechanical values for the angular momentum, the rotational energy is given by

$$E = \frac{\hbar^2}{2\mathcal{I}}I^2 \tag{6}$$

where I is the angular momentum quantum number in $\sqrt{(I(I+1))}$. Thus, successive states in the rotational ground-state band of an even-even nucleus have energies given by

$$E(2^+) = 6\frac{\hbar^2}{2\mathcal{I}} \tag{7}$$

$$E(4^+) = 20\frac{\hbar^2}{2\mathcal{I}} \tag{8}$$

$$E(6^+) = 42\frac{\hbar^2}{2\mathcal{I}} \tag{9}$$

and so on. Note that the ratio of the energies of the first 4^+ and 2^+ states is 20/6 = 3:33. The E(4^+) : E(2^+) ratios very rarely become exactly 3.33 because real nuclear systems are not perfect rigid rotors with a fixed moment of inertia. They are better described as being composed of a fluid of nucleons which can experience some centrifugal stretching. Collective properties vary slowly and smoothly with nucleon number, and to a first approximation are independent of the number of valence nucleons outside the filled sub-shells.

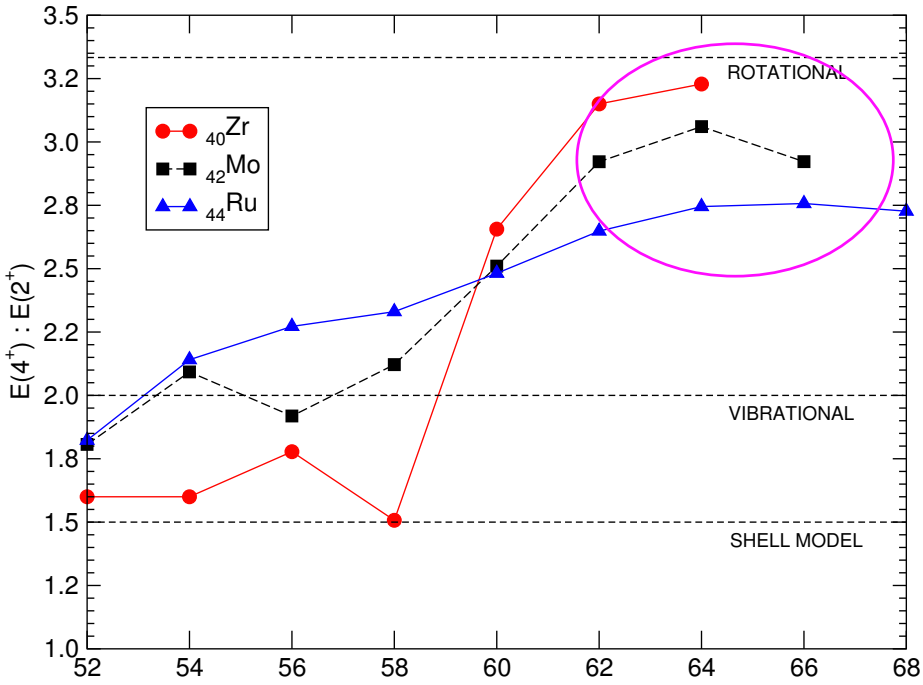

Figure 51: E(4^+):E(2^+) ratios of ground state rotational bands in neutron rich Zr, Mo and Ru nuclei.

The g-factors of excited states in even-even nuclei can also be predicted. For example, the collective rotation of protons can be regarded as an electric current responsible for a corresponding magnetic moment. For a state with angular momentum, I, the contribution made from protons to this angular momentum is equal to Z/A. If we assume that the neutrons make no contribution to the magnetic moment and that each pair of protons/neutrons are coupled in a spin-zero configuration, the g-factor of this state is simply given by

$$g = \frac{Z}{A}. \tag{10}$$

More refined models allow for non-rigid collectivity by reducing g-factor by a uniform factor. For example, Greiner [Gre66] assumed that the distribution of protons within the nucleus is less deformed than that of neutrons due to the fact that protons are known to be subject to a slightly greater pairing force. Hence the neutrons are assumed to contribute slightly more to the collective motion of the nucleus than the protons. This imbalance is

expressed as

$$g = \frac{Z}{A}(1 - 2f) \tag{11}$$

where

$$f = \frac{N}{A}[(\frac{G_n}{G_p})^{\frac{1}{2}}) - 1] \tag{12}$$

and the proton and neutron pairing strength parameters are given by G_p and G_n, respectively.

The Interacting Boson Models

The Interacting Boson Models (IBM) was first introduced by Arima and Iachello [Ari75] as an alternative description of the collective properties of nuclei. Essentially, there are two models: IBM1, treats protons and neutrons equally and is similar to the collective model; IBM2, treats protons and neutrons separately and is more like a shell model description of the nuclear system.

The most fundamental assumption of the IBM is that the low-lying collective states of even-even nuclei are governed by the interactions of a fixed number, N of bosons. These bosons are either particulate pairs of protons and neutrons or pairs of proton- and neutron-holes. The bosons exist around the known shell closures and it is only these valence bosons that contribute to nuclear structure as opposed to the total number of bosons.

The IBM bosons exist in configurations where the constituent particles (protons or neutrons) are coupled into one of two possible states: those with angular momentum $l = 0$ (s-boson) and those with $l = 2$ (d-bosons). A boson vacuum corresponds to a doubly-magic nucleus and the energy levels and properties of more complicated nuclei are built on the individual bosons present in the system as well as the interactions between them.

For the investigation of magnetic moments and g-factors, the IBM2 model was adopted [Sam84]. Since the proton (π) and neutron (ν) bosons are treated separately, the total number of bosons is given by

$$N_t = N_\pi + N_\nu \tag{13}$$

where N_π and N_ν are the separate proton- and neutron-boson numbers. The magnetic dipole moment operator in IBM2 is given by

$$\hat{\mu} = \sqrt{\frac{3}{4\pi}}(g_\pi \hat{L}_\pi + g_\nu \hat{L}_\nu) \tag{14}$$

where g_π, g_ν are the proton- and neutron-boson *g*-factors, respectively, and $\hat{L}_\pi$, $\hat{L}_\nu$ are the proton- and neutron-boson angular momentum operators, respectively. Since $L_\mu = L_\pi + L_\nu$, Equation 14 is rearranged to

$$\hat{\mu} = \sqrt{\frac{3}{4\pi}}[\frac{1}{2}(g_\pi + g_\nu)L_\mu + \frac{1}{2}(g_\pi - g_\nu)(L_\pi - L_\mu)] \tag{15}$$

The first term is diagonal, so in IBM2, only the second term contributes. The g-factor of the $I^\pi = 2^+$ state is then given by

$$g = \frac{N_\pi}{N_t} g_\pi + \frac{N_\nu}{N_t} g_\nu \tag{16}$$

Equation 16 is valid only if the 2^+ state is F-spin symmetric. F-spin is a new quantum number in IBM2 which is used to describe proton and neutron bosons [Sam84]. Note that with $g_\pi = 1$ and $g_\nu = 0$, this equation reduces to the collective model, $g = Z/A$, but only if Z and A are taken to be the number of valence nucleons as opposed to the total number of nucleons.

Gamma-Ray Angular Correlation

A two-component γ-ray cascade involving nuclear states with spins I_1, I_2 and I_3 may be described with Figure 52. The L_1 and L_2 define the multipole orders of the first and second transitions, respectively, and are the minimum values obtained from

$$|I_1 - I_2| \leq L_1 \leq |I_1 + I_2|$$
$$|I_2 - I_3| \leq L_2 \leq |I_2 + I_3| \tag{17}$$

The $L_1' = L_1 + 1$ and $L_2' = L_2 + 1$ describe possible multipole mixtures in γ_1 and γ_2. The mixing ratio is defined as the ratio of reduced γ-ray matrix elements, such as for γ_1,

$$\delta_1 = \frac{< I_2 \| L_1' \| I_1 >}{< I_2 \| L_1 \| I_1 >} = \frac{< I_2 \| L_1 + 1 \| I_1 >}{< I_2 \| L_1 \| I_1 >}. \tag{18}$$

Thus, the ratio of the intensities of the $L_1 + 1$ and L_1 components is given by δ_1^2. A similar parameter may be defined for γ_2 if it should also be mixed.

The theory of gamma-ray angular correlations has been treated in great details [Rac51] [Ham75] [Sie65]. For a two-component cascade, the angular correlation $W(\theta)$ has the form

$$W(\theta) = \sum_{k=even} A_k(\gamma_1) A_k(\gamma_2) P_k(\cos\theta) \tag{19}$$

where k = 0, 2, 4, ..., θ is the angle between the propagation vectors of the two γ-rays, and $P_k(\cos\theta)$ are normalized Legendre polynomials. If we assume that each transitions is a mixture of no more than two multipole, the maximum value of $k = Min(2L_1', 2L_2', 2I_2)$. Then $A_k(\gamma_1)$ and $A_k(\gamma_2)$ are determined by the parameters of γ_1 and γ_2, respectively. With normalized $A_0(\gamma_1) = A_0(\gamma_2) = 1$, $W(\theta)$ becomes,

$$W(\theta) = 1 + \sum_{k=even} A_k P_k(\cos\theta). \tag{20}$$

The most general form for A_k occurs when both radiations are mixed,

$$\begin{aligned} A_k &= \frac{1}{1+\delta_1^2}\{F_k(L_1 L_1 I_1 I_2) + (-1)^{L_1 - L_1'} 2\delta_1 F_k(L_1 L_1' I_1 I_2) + \delta_1^2 F_k(L_1' L_1' I_1 I_2)\} \\ &\times \frac{1}{1+\delta_2^2}\{F_k(L_2 L_2 I_3 I_2) + 2\delta_2 F_k(L_2 L_2' I_3 I_2) + \delta_2^2 F_k(L_2' L_2' I_3 I_2)\} \end{aligned} \tag{21}$$

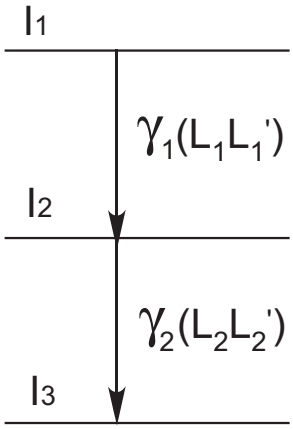

Figure 52: A gamma-ray cascade.

The F-coefficients are given by

$$\begin{aligned} F_k(L_1 L_1' I_1 I_2) &= (-1)^{I_1+I_2-1}(2L_1+1)(2I_2+1)^{1/2}(2k+1)^{1/2} \\ &\times \begin{pmatrix} L_1 & L_1' & k \\ 1 & -1 & 0 \end{pmatrix} \begin{Bmatrix} L_1 & L_1' & k \\ I_2 & I_2 & I_1 \end{Bmatrix} \end{aligned} \tag{22}$$

and similarly for $F_k(L_2 L_2' I_2 I_3)$.

As for Equation 20, it is usually sufficient to consider only the A_2 and A_4 parameters in $\gamma - \gamma$ angular correlations, thus we have

$$W(\theta) = 1 + A_2 P_2(\cos\theta) + A_4 P_4(\cos\theta). \tag{23}$$

with

$$\begin{aligned} P_2(\cos\theta) &= \frac{1}{2}(3\cos^2\theta - 1) \\ P_4(\cos\theta) &= \frac{1}{8}(35\cos^4\theta - 30\cos^2\theta + 3). \end{aligned} \tag{24}$$

Theoretical A_2 and A_4 coefficients are tabulated in [Tay71]. We have developed a program to calculate the theoretical angular correlation coefficients as well.

Perturbed Angular Correlation

To measure the magnetic moments of short-lived states, the perturbed angular correlation/distribution (IPAC/D) technique is required to be employed with the intense hyperfine fields present at dilute impurities implanted into ferromagnetic hosts. Usually heavy-ion beams are used to create and excite the nuclei of interest and implant them during recoil into a ferromagnetic host placed behind a target foil [Stu01]. Another important class of measurements is to use spontaneous fission sources to populate excited states and ferromagnetic materials to provide hyperfine fields [Smi99] [Pat02].

In general, the measurements of g-factors require that the precession of nuclear state in the hyperfine field to be extracted from the perturbed angular correlation/distribution. Once the precession angle has been measured, the effective magnetic field at the nucleus, B_{eff}, and the effective interaction time of the nuclear state with the field, t_{eff}, must be known to extract the g-factor value, since

$$\phi = -g\frac{\mu_N B_{eff} t_{eff}}{\hbar} \tag{25}$$

Perturbation From a Static Magnetic Field

A general scheme of perturbation from an external magnetic field is shown in Figure 53. If we take the alignment axis to be the direction of the feeding γ-ray, the angle between γ_1 and γ_2 is given by

$$\cos\Theta_{12}(\theta_1, \theta_2, \phi, t) = \cos\theta_1 \cos\theta_2 + \sin\theta_1 \sin\theta_2 \cos(\phi - \omega t) \tag{26}$$

Therefore, the angular correlation of these two γ-rays, Equation 23, can be re-arranged and gives the time-dependent, perturbed angular correlation function,

$$W(\theta_1, \theta_2, \phi, t) = \sum_{n=0}^{n=4} f_n(\theta_1, \theta_2) \cos(n(\phi - \omega t)) \tag{27}$$

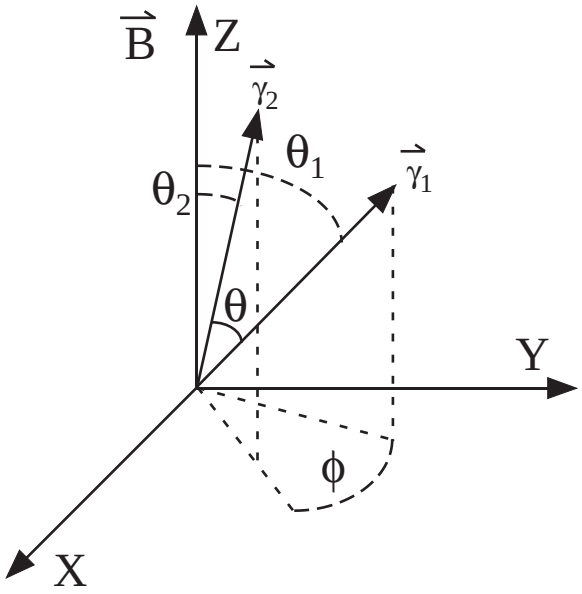

Figure 53: A geometry used in discussion of perturbed angular correlations.

where the coefficients are given by

$$\begin{aligned}
f_0 &= 1 + A_2(\frac{3}{2}A^2 + \frac{1}{2}B^2 - \frac{1}{2}) \\
&+ A_4(\frac{3}{8} + \frac{105}{8}A^2B^2 + \frac{35}{8}A^4 + \frac{105}{64}B^4 - \frac{15}{4}A^2 - \frac{15}{8}B^2), \\
f_1 &= A_2(3AB) + A)4(\frac{105}{8}B^3A + \frac{35}{8}A^3B - \frac{15}{2}AB), \\
f_2 &= A_2(\frac{3}{4}B^2) + A_4(\frac{35}{16}B^4 + \frac{105}{8}A^2B^2 - \frac{15}{8}B^2), \\
f_3 &= A_4(\frac{35}{8}AB^3), \\
f_4 &= A_4(\frac{35}{64}B^4).
\end{aligned} \tag{28}$$

The two constants, A and B, are given by $A = \cos\theta_1 \cos\theta_2$ and $B = \sin\theta_1 \sin\theta_2$, respectively. The time integral perturbed angular correlation becomes

$$W(\theta_1, \theta_2, \phi) = \frac{1}{\tau} \sum_{n=0}^{n=4} f_n(\theta_1, \theta_2) \int_0^\infty e^{-\frac{t}{\tau}} \cos(n(\phi - \omega t))dt \tag{29}$$

The integration over the mean lifetime of the state, τ, allows the perturbed angular correlation function to be dependent on the average precession angle, $\phi_p = \omega\tau$,

$$W_p(\phi_p) = \sum_{n=0}^{n=4} \frac{f_n(\theta_1, \theta_2)}{(1 + n^2\phi_p^2)^{1/2}} [\cos(n\phi) + n\phi_p \sin(n\phi)] \tag{30}$$

This is a 3-dimensional description of perturbed angular correlation from an aligned **B** field, given by D. Patel *et al.*[Pat02]. In their work, the double ratio is defined and interpreted as

$$\rho_{12}(\phi_p) = \frac{W_p(\theta_1, \theta_2, \phi, +\phi_p)}{W_p(\theta_1, \theta_2, \phi, -\phi_p)}. \tag{31}$$

These double ratios can allow a non-linear, least squares fit analysis in order to extract the precession angle, ϕ. By using this technique, g-factors of many excited states populated from spontaneous fission have been determined. More details are given in [Pat02].

Perturbation From Randomly Oriented Magnetic Field

The perturbation from a randomly oriented classical magnetic field B of constant magnitude (e.g. magnetic fields in randomly oriented ferromagnetic domains) is a more complicated case and has been discussed in details in [Mat65] and [Ham75]. The perturbed angular correlation is described by

$$W(\theta) = 1 + A_2^{the} G_2 P_2(\cos\theta) + A_4^{the} G_4 P_4(\cos\theta) \tag{32}$$

where G_2 and G_4 are the attenuation factors, defined as

$$G_k = \frac{A_k^{exp}}{A_k^{the}}. \tag{33}$$

The attenuation factor G_k is related to the precession angle ϕ in Equation 25 as

$$G_k = \frac{1}{2k+1}(1 + 2\sum_{q>0}^{k} \frac{1}{1+q^2\phi^2}). \tag{34}$$

In our 2000 binary fission experiment, the Californium source was sandwiched between two Fe foils, with no external magnetic field, as shown in Figure 54. The recoiling fission fragments are implanted into the un-magnetized iron foils. We have also assumed that the domains in the foil are randomly oriented and small enough that there is no preferential direction in the foil. With a large set of statistical events collected, we are able to measure g-factors of excited states in neutron-rich nuclei. If the state of interest interacts

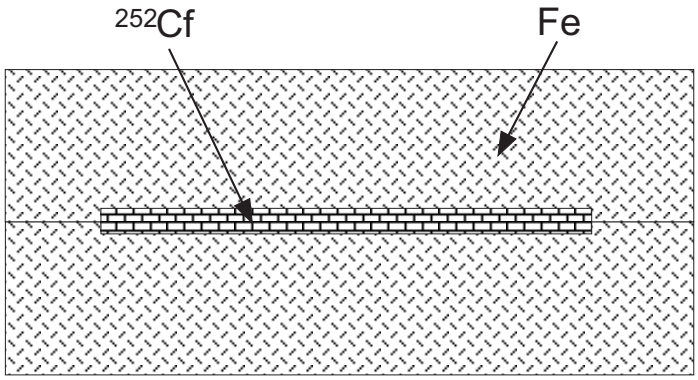

Figure 54: A scheme of experimental setup of our 2000 binary fission experiment. The ^{252}Cf source was sandwiched between two Fe foils.

with a magnetic field of sufficient strength for a sufficient length of time, which means, in Equation 25, the τ is much longer than the stopping time, the attenuation in Equation 32 will be measurable. Typically, the error is small for states with lifetimes between a few hundred picoseconds and a few nanoseconds and for magnetic fields between 10 and 100 Tesla. For the excited states with very short lifetimes, but longer than the stopping time ($\sim$ few picoseconds), it is assumed that the angular correlation for γ-rays connecting this state will not be perturbed. Otherwise, the observed angular correlations will be affected by transient field effect. But for longer lifetimes, the nucleus will be subject to a hyperfine field (HFF) and precess about this field. It's assumed that the HFFs are those of an ion implanted in a substitutional site in the lattice [Rao79], as shown in Figure 55.

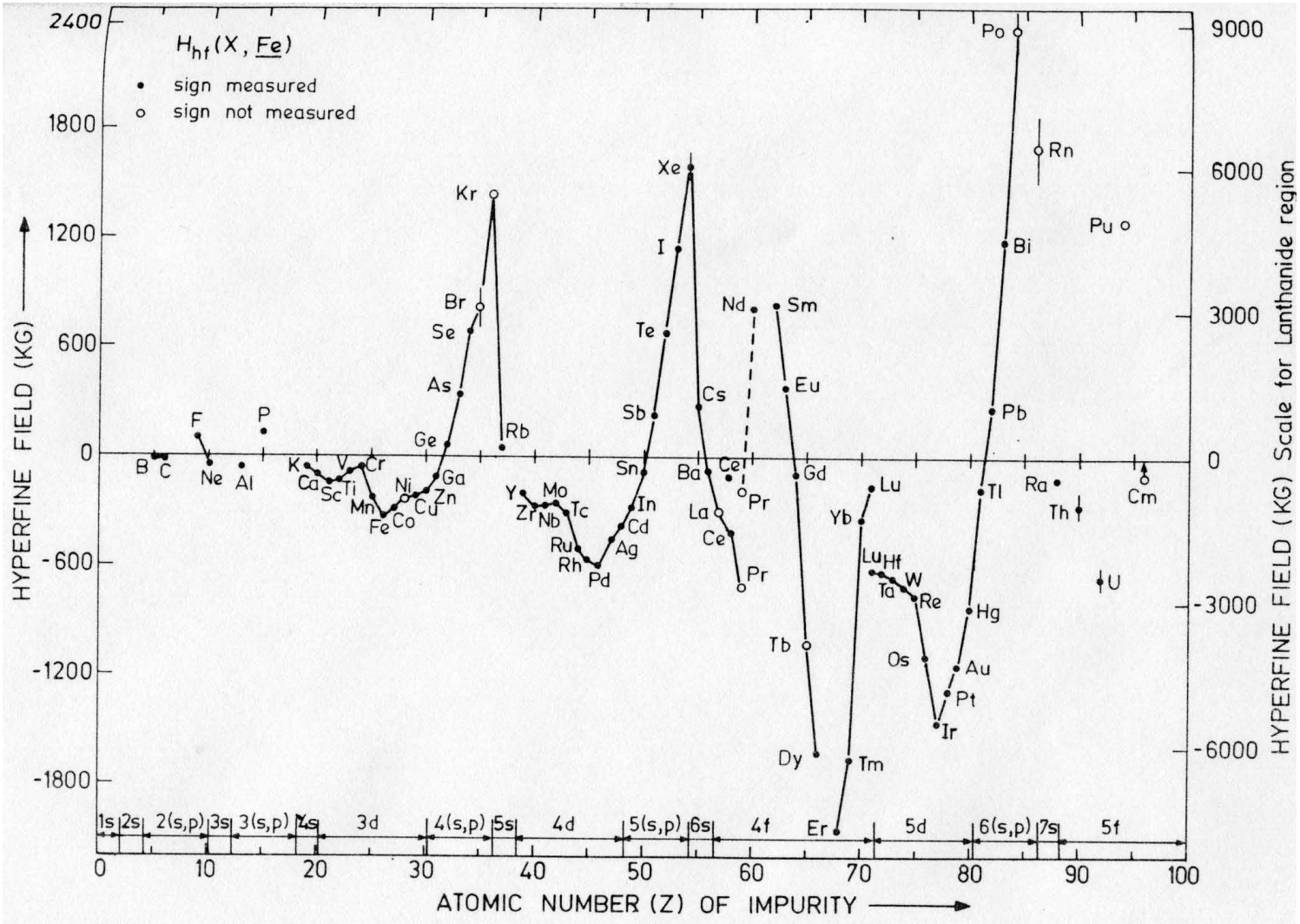

Figure 55: Calculated impurity hyperfine field for isotopes in Fe lattice [Rao79].

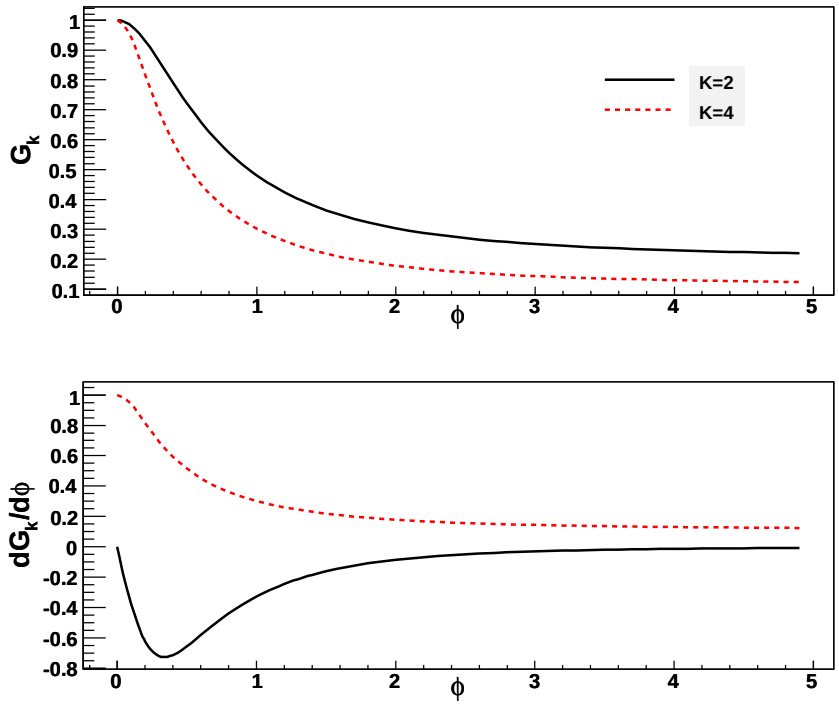

Figure 56: Dependence of $G_{2,4}$ and $|\frac{dG_{2,4}}{d\phi}|$ on the precession angle ϕ.

The dependence of G_k and the its derivative on the precession angle ϕ is shown in Figure 56. As ϕ gets large, the uncertainty in our measurement, which depends on $|dG_{2,4}/d\phi|$, also gets very large. The same is true if ϕ is very small. This places a fundamental limitation on the sensitivity of our method of measuring a perturbed angular correlation (PAC) to deduce the g-factor of an excited state. Also, it is clear from Equation 34 that the PAC method can only determine the magnitude, and not the sign of the g-factor. This is in contrast to the method employed by [Pat02], in which the HFFs were aligned by an external magnetic field. Despite the limitations in our measurement, there are still many cases where this method can be applied with useful accuracy.

In practice, the experimental angular distribution function is given by

$$N(\theta_n) = A_0^{exp}(1 + A_2^{exp}P_2(\cos\theta_n) + A_4^{exp}P_4(\cos\theta_n)) \tag{35}$$

for some set of discrete angles, θ_n.

Angular Properties of Gammasphere

The 110 Ge detectors in the Gammasphere array are arranged in 17 concentric rings of constant angle θ relative to the beamline axis. For example, the 10 detectors located at $\theta_i = 90^\circ$ make up the central ring which occupies the $z = 0, x - y$ plane.

Figure 57 shows the polar and azimuthal positions of each Gammasphere detector with respect to the center of the array. To create angle bins, all possible detector pairs were considered. The 110 detectors create 110$\times$109/2=5995 number of pairings. For detector i and detector j, the angle between them is,

$$\begin{aligned} \cos\theta_{ij} &= \hat{\theta}_i \cdot \hat{\theta}_j \\ &= \sin\theta_i \cos\phi_i \sin\theta_j \cos\phi_j + \sin\theta_i \sin\phi_i \sin\theta_j \sin\phi_j + \cos\theta_i \cos\theta_j \end{aligned} \quad (36)$$

Since these detectors were symmetrically arranged on the Gammasphere support cage, we are able to reduce the angle bins to 64 discrete values. Each angle bin has many detectors, generally between 55 and 120. For our experiment, only 101 detectors were present, so the number of detectors in each bin is slightly different from that of Gammasphere at full capacity. The angle bin information is given in Table 7.

Table 7: Angle bins in Gammasphere. (101 detectors).

N_{bin}	Cos(θ)	N_{pairs}	N_{bin}	Cos(θ)	N_{pairs}
1	0.939	203	2	0.934	58
3	0.840	47	4	0.823	45
5	0.815	104	6	0.809	56
7	0.764	100	8	0.762	45
9	0.755	50	10	0.745	30
11	0.656	50	12	0.613	104
13	0.594	88	14	0.580	100
15	0.577	116	16	0.500	56
17	0.495	88	18	0.471	52
19	0.391	91	20	0.357	58
21	0.333	60	22	0.327	44

Continued on next page

Table 7 – continued from previous page

N_{bin}	Cos(θ)	N_{pairs}	N_{bin}	Cos(θ)	N_{pairs}
23	0.309	56	24	0.298	100
24	0.282	101	26	0.269	104
27	0.175	100	28	0.168	44
29	0.139	23	30	0.064	92
31	0.057	104	32	0.000	273
33	-0.057	104	34	-0.064	90
35	-0.139	23	36	-0.168	44
37	-0.175	101	38	-0.269	104
39	-0.282	101	40	-0.298	100
41	-0.309	56	42	-0.327	46
43	-0.333	60	44	-0.357	58
45	-0.391	90	46	-0.471	52
47	-0.495	89	48	-0.500	56
49	-0.577	116	50	-0.580	101
51	-0.594	90	52	-0.613	104
53	-0.656	50	54	-0.745	30
55	-0.755	50	56	-0.762	45
57	-0.764	100	58	-0.809	56
59	-0.815	104	60	-0.823	44
61	-0.840	44	62	-0.934	58
63	-0.939	196	64	-1.000	46

Solid Angle Correction and Response Function

In practice, the extended size of the detectors must be taken into consideration in angular correlation measurements. For our 2000 binary fission experiment with the Gammasphere detector array, the ^{252}Cf source can be taken to be point-like, but each HPGe detector has an opening angle of 7° which is not negligible. Therefore, A_2 and A_4 need to be corrected by multiplying solid angle correction factors, which can be theoretically calculated [Ham75].

$$Q_\lambda = J_\lambda / J_0. \tag{37}$$

The J_λ coefficients are evaluated from the solid angle subtended by the detector on the source and

$$J_\lambda = \int_0^\gamma P_\lambda \varepsilon(\alpha) \sin\alpha d\alpha \tag{38}$$

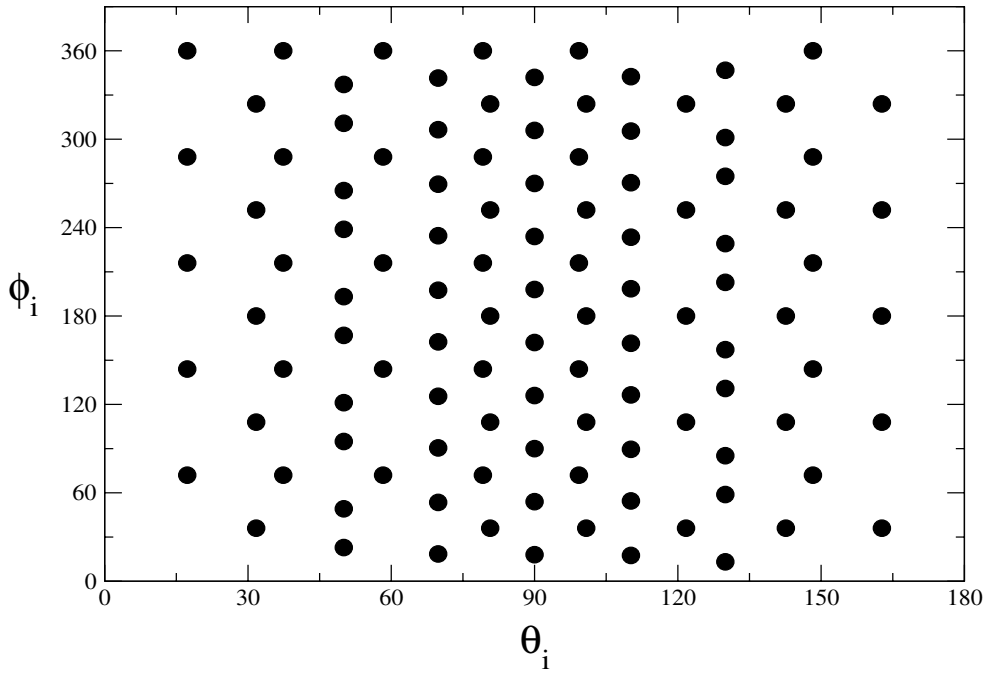

Figure 57: The polar (θ_i) and azimuthal (ϕ_i) positions of each detector within the Gammasphere array.

where α is the angle between the photon direction and the detector-source axis. If it is assumed that the detector response is uniform across its front face and the detection efficiency, ϵ, is independent of the angle at which the photon enters the detectors, then

$$J_\lambda = \varepsilon \int_{\cos\gamma}^{1} P_\lambda(x)dx \tag{39}$$

with

$$\begin{aligned} J_0 &= \varepsilon(1-\cos\gamma) \\ J_2 &= \frac{1}{2}\varepsilon\cos\gamma(1-\cos^2\gamma) \\ J_3 &= \frac{1}{8}(-3\cos\gamma+10\cos^3\gamma-7\cos^5\gamma) \end{aligned} \tag{40}$$

For Gammasphere detectors, Q_2 and Q_4 are calculated to be

$$\begin{aligned} Q_2 &= 0.9779, \\ Q_4 &= 0.9278. \end{aligned} \tag{41}$$

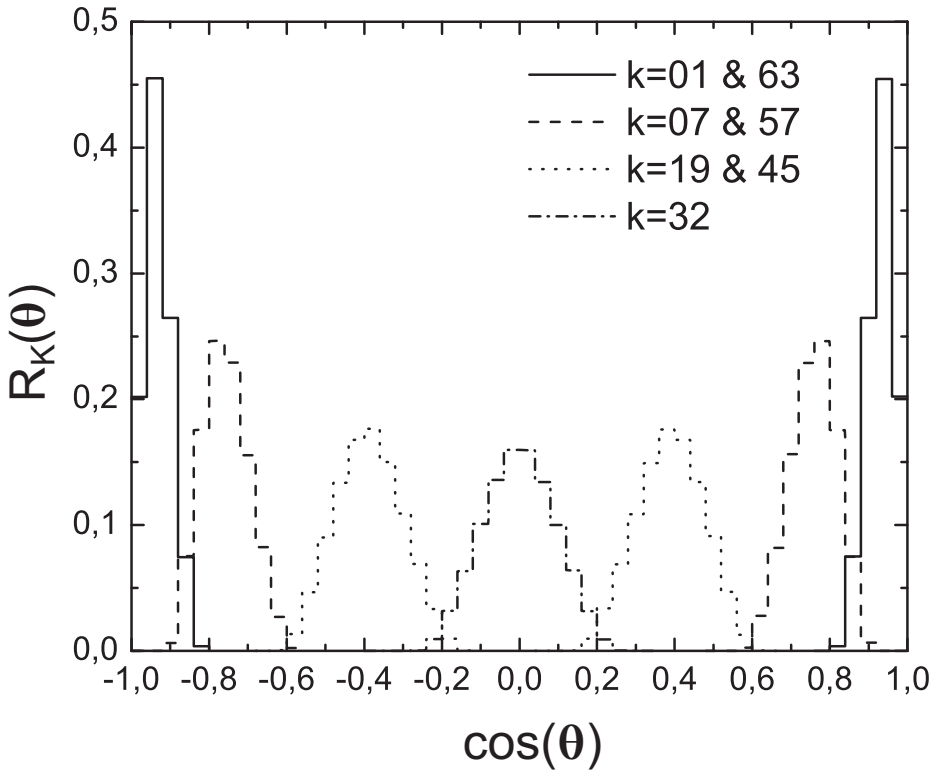

Figure 58: The response functions of five of the 64 angle bins.

For a typical angular correlation measurement, it is necessary to calculate a solid angle correction factor Q_k for each parameter A_k. However, for very low intensity transitions, the sensitivity of the angular correlation measurement can be improved by determining the detector response function $R_n(\theta, E_1, E_2)$ for each pair of detectors. For a given detector pair, the response function describes the distribution of possible angles about the central angle of the pair as a function of energy. The response functions for each pair can then be summed to find the response function of each angle bin.

We calculated the response function using a simple Monte Carlo simulation, with the γ ray transport simulated up to the first collision. This is equivalent to the traditional calculation of Q_k. The mean free path, $\lambda(E)$, of γ-rays was calculated using the known Gammasphere detector properties. The energy dependence of $R_n(\theta, E_1, E_2)$ is negligible, and so only $R_n(\theta)$ was calculated. Examples of response functions for a few bins are shown in Figure 58.

Data Sorting and Fragment Identification

In the November, 2000 run, 182 tapes of data was recorded, with 1.1×10^{11} triple- and higher-fold coincidence events, which is effectively 6.6×10^{11} pure triple coincidence events. For the angular correlation measurements, the data were sorted into 64 two dimensional histograms corresponding to the 64 angle bins, as defined in Table 7. The histograms were produced by reading the data files event by event. For each $\gamma - \gamma$ coincidence, the angle between the detectors was calculated and the event was added to the corresponding histogram. For each angle bin, the histogram was fit to find the coincidence counts for a given γ-ray cascade. For each bin, n, the histogram was then fit to find the number of coincidences of the cascade of interest, N_n. This N_n must be corrected for the detector response functions, relative detector efficiency, and the number of detectors in the particular. The value for the corrected N_n is given by

$$N_n = \varepsilon_n(E_1, E_2) \times \int_0^{\pi} W(\theta) R_n(\theta, E_1, E_2) \sin(\theta) d\theta \tag{42}$$

where $\varepsilon_n(E_1, E_2)$ is the relative efficiency of the pair and $R_n(\theta, E_1, E_2)$ is the response function of the pair. As an example, the coincidence peaks of 171.8- and 350.8-keV transitions in ^{106}Mo in angle bin 1 and 61 matrices are shown in Figure 59.

Transitions in high-yield fragments from the SF of ^{252}Cf can be easily identified. In the 64 matrices created with full energy ranges, many angular correlations can be measured directly. However, in some cases, additional gating γ-rays are required to resolve transitions in nuclei of interest and reduce contamination from γ-rays with similar energies. One example is to measure angular correlations in the ground bands of ^{104}Mo and ^{108}Mo nuclei. Partial level scheme of these two nuclei are shown in Figure 60. The 368.6-192.4 keV cascade in ^{104}Mo and 371.0-192.7 keV cascade in ^{108}Mo have very similar energies. In the full two-dimensional matrices, it is hard to resolve correlation peaks in these two nuclei, as shown in Figure 61. Our solution is to add additional gating γ-rays to increase selectivity. The gating γ-rays come from upper transitions in the nucleus of interest or from its fission

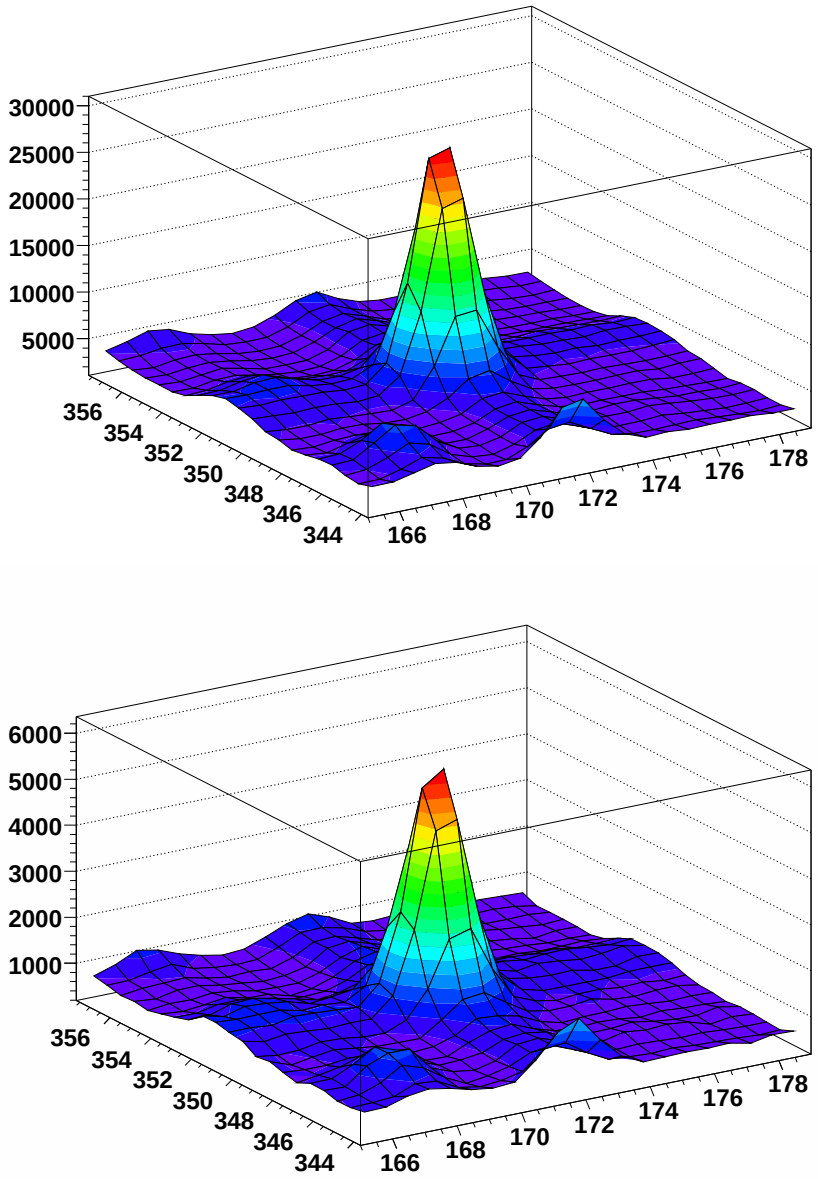

Figure 59: Coincidence peak of 171.8- and 350.8-keV transitions in ^{106}Mo in angle bin number 1 (top) and 61 (bottom).

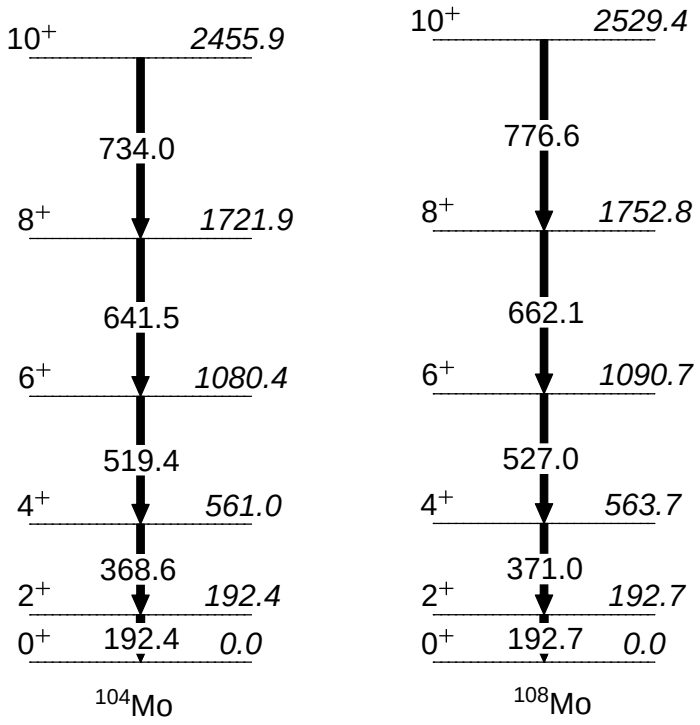

Figure 60: Partial ground bands of ^{104,108}Mo.

partners. For example, by taking 519.4- and 641.5-keV transition gates in ^{104}Mo to measure angular correlation between 368.6- and 192.4-keV transitions, and 527.0- and 662.1-keV transition gates to measure angular correlation between 192.7- and 371.0-keV transitions in ^{108}Mo, we would have much better peak resolutions, as shown in Figure 62. For some cases to measure weak cascades in these nuclei, we can use additional gates from partner nuclei. Recall that in SF of ^{252}Cf, prompt transitions in complementary nuclei are in coincidence. Study of binary fission [TA97] [Fon06] [Goo06] have shown that the neutron channels lead to different yield ratios, and generally the $4n$ channel is the strongest channel. For ^{104}Mo, ^{108}Mo, their strongest partners are ^{144}Ba and ^{140}Ba, respectively. Therefore, for ^{104}Mo and ^{108}Mo, transitions in ^{144}Ba and ^{140}Ba can also be used as additional gates. Software have been developed to create the 64 histograms with additional gating γ-rays. Fitting procedures are same as the measurement from those full matrices.

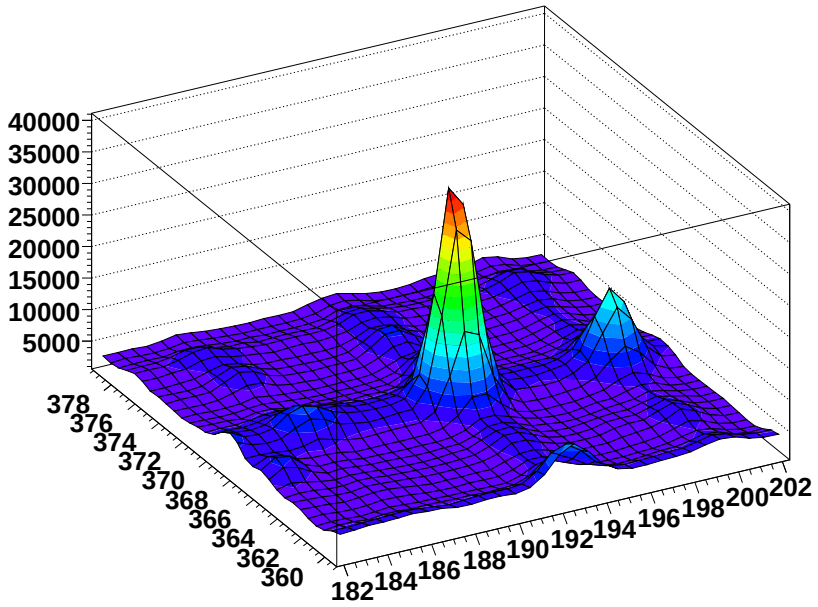

Figure 61: In the full matrix, the correlation peaks of 192.4–368.6 keV in ^{104}Mo and 192.7–371.0 keV in ^{108}Mo overlap.

Relative Efficiency Correction

After matrices are created, the next step is to fit each matrix to find correlations counts and fit with Equation 32 to find out those attenuation factors. However, it has been shown [Pat02] that the efficiencies of the individual detectors of Gammasphere may vary greatly compared to the mean efficiency.

We have scanned the projection spectrum of each detector. For each one detector, its normalized detector efficiency curve is calculated by dividing the sum of all detectors. Two efficiency curves are shown in Figure 63, which shows how the relative efficiency varies greatly for some detectors. Actually most detectors have similar curves as detector 5. However, some detectors have efficiency curves which vary a lot. This may be related with the experimental setup. Therefore, for an angle bin, the efficiency is given by

$$\varepsilon_n(E_1, E_2) = \frac{1}{2}\sum_{i,j}[\varepsilon_i(E_1)\varepsilon_j(E_2) + \varepsilon_i(E_2)\varepsilon_j(E_1)], \tag{43}$$

which is a sum of all detector pairs belonging to this bin. Equation 43 also works as a smoothing procedure of statistical errors.

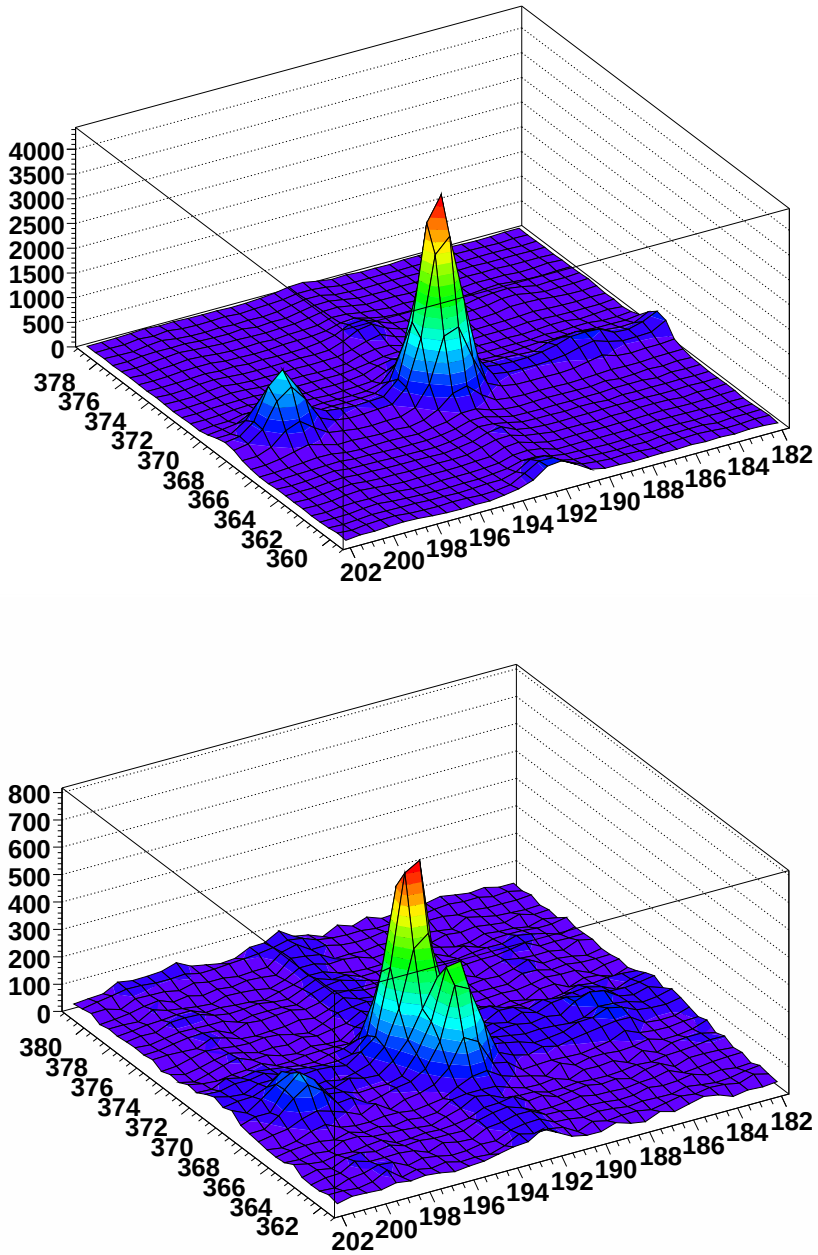

Figure 62: (Top)Correlation peak 192.4–368.6 keV cascade in ^{104}Mo gated by 519.4 and 641.5 keV transitions. (Bottom)Correlation peak of 192.7–371.0 keV cascade in ^{108}Mo gated by 527.0 and 662.1 keV transitions.

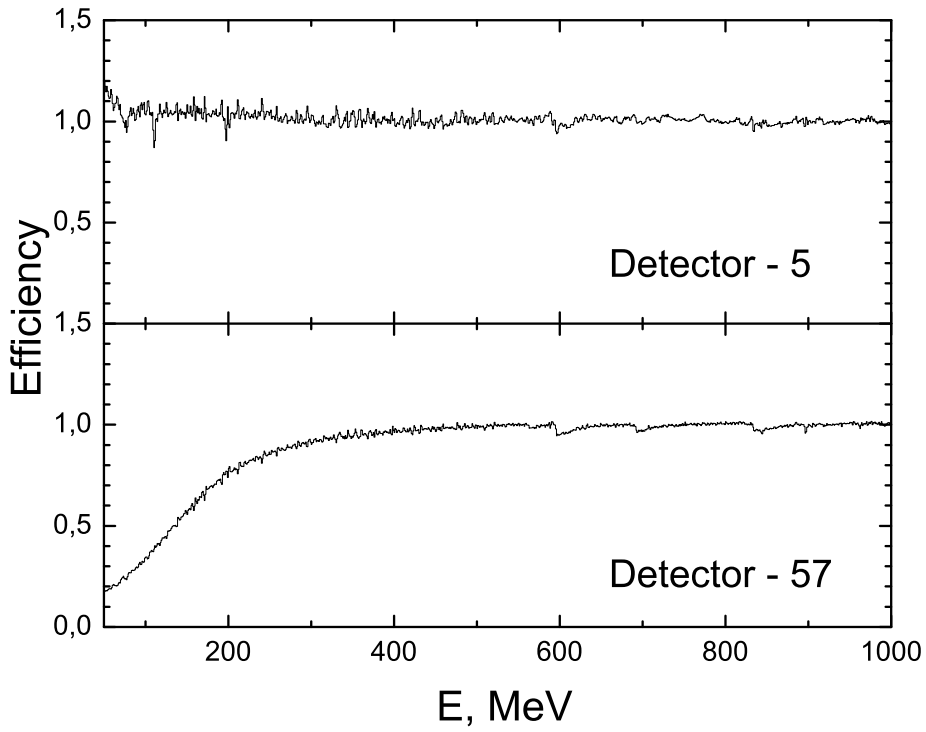

Figure 63: Relative efficiencies of detectors 5 and 57.

Fitting Procedure

To determine the angular correlation, each of the 64 histograms was fit to find the intensity of the peak of interest, N_n. Our method is based on the analysis of two dimensional $\gamma - \gamma$ coincidence spectra given in [TA97]. To fit a given histogram, a window within the histogram is selected. Within this window, the positions of the peaks are defined by using projections of the histogram on the two axes. The surface is then approximated by three types of background and the sum of the two dimensional γ peaks found in the projections. The three types of background consist of a smooth background and two series of ridges parallel to the axes corresponding to γ lines in the x and y direction. The last part of the fitting procedure is to solve a well known NNLS (Non-Negative Least Square) problem [Law74].

Using the N_n^{exp} found from fitting the histograms,we can estimate the two parame-

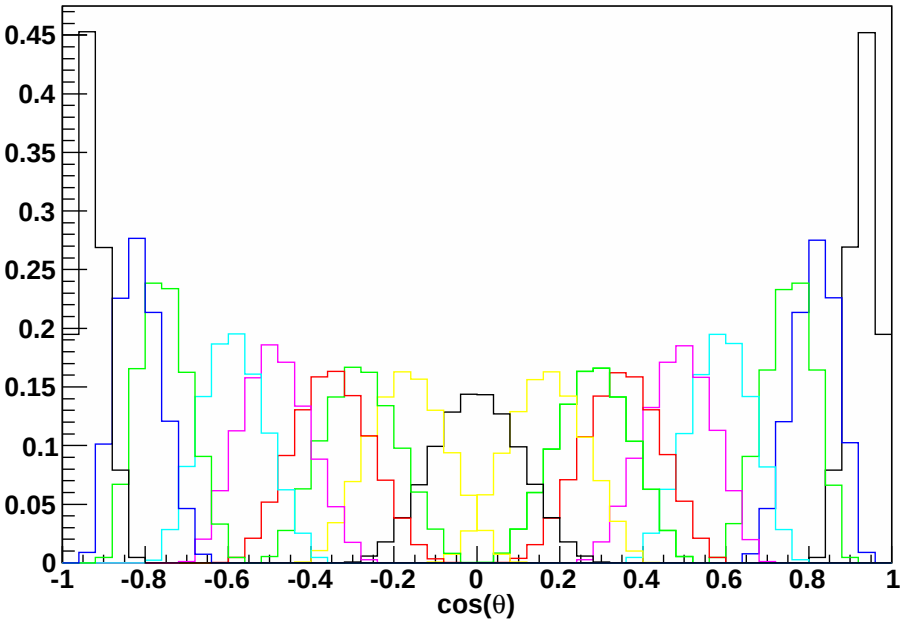

Figure 64: The response functions of the 17 groups in the ideal case when all 110 detectors are present and have the same efficiency.

ters A_2^{exp} and A_4^{exp} using the minimization expression

$$min \sum_n \frac{(N^{exp}(\theta_n) - N(\theta_n))^2}{\delta_{n,exp}^2 + \delta_{n,model}^2} \tag{44}$$

The experimental uncertainty in the γ peak intensity is always much greater than the model error, so δ_{model} was neglected. Once the experimental A_2 and A_4 are found, the g-factor can be calculated by using the procedure outlined in the previous sections.

In practice, a set of 64 experimental points is more than adequate to estimate the three parameters in Equation 35, and it is therefore convenient to further combine angle bins, thereby increasing the statistics of each bin. Note that the minimization approach did not assume that all the pairs of a group must have the same angle. This means we can group the angle bins into even larger groups by using the equation

$$N_{gr_\alpha} = \sum_n \epsilon_n(E_1, E_2) \times \int_0^\pi W(\theta) \sum_n R_n(\theta) sin(\theta) d\theta \tag{45}$$

The N_{gr_α} can be obtained in two different ways. The most straightforward way is to sum the N_n values given by Equation 42 for some grouping. Another way is to sum the two-dimensional histograms by this grouping and then fit the histograms in the same way as N_n to find N_{gr_α}. The results of the two methods are nearly identical in most cases. However, for very weakly populated decays, it is necessary to use the second method to better resolve the peak of interest. In both cases, we grouped the 64 angle bins into 17 larger bins. The response function for each of the 17 groups is presented in Figure 64, which shows the angular position and resolution of the bins.

Several cases have been shown in Chapter. 3 for spin/parity assignments using this technique. For a given cascade, if the lifetime of the intermediate state is much less than the order of *nanosecond*, the perturbation effect, or the attenuation of the angular correlation, will be very small. The measured angular correlation coefficients will be same as theoretical values. By comparing measured angular correlation coefficients with theoretical predictions [Tay71], we can get evidence to support spin/parity assignments, as we have shown in the previous chapter. Here one strong cascade is given to show the validity of this technique. For the $6^+ \rightarrow 4^+ \rightarrow 2^+$, 486.6 – 326.5 keV cascade in the ground-state band of ^{102}Zr , the lifetime of the 4^+ state in the ground band of ^{102}Zr is around 30 $\sim$ 50 ps. So the attenuation of angular correlations of the 486.6 – 326.5 keV cascade should be very small. Matrices were created for this cascade by gating on other γ-rays in this band. The fitting curve is shown in Figure 65. The experimental angular correlation coefficients are $A_2^{exp} = 0.099(7)$ and $A_4^{exp} = 0.004(10)$, which are consistent with the theoretical values of $A_2^{the} = 0.102$ and $A_4^{the} = 0.009$ for a quadrupole – quadrupole cascade within error bar [Tay71]. More measurements of similar "prompt" cascades confirmed this technique as well.

A set of $\Delta I = 1$ doublet bands recently observed in ^{106}Mo were proposed as chiral doublets, but the spins and parities were assigned tentatively. With the technique developed, we are able to measure angular correlations of some cascades involved with these bands. A partial level scheme of ^{106}Mo is shown in Figure 66. Relative intensities of γ-ray transitions in ^{106}Mo have been measured. We will measure some cases which have relatively high intensities.

The first cascade we measured is the 517.5 – 724.4 keV cascade, proposed with a $5^- \rightarrow 4^+ \rightarrow 2^+$ spin configuration. Therefore, a dipole-quadrupole correlation is expected, with theoretical coefficients of $A_2^{the} = -0.07$ and $A_4^{the} = 0$. As shown in Figure 67, the measured angular correlation coefficients are $A_2^{exp} = -0.088(17)$, and $A_4^{exp} = -0.004(25)$.

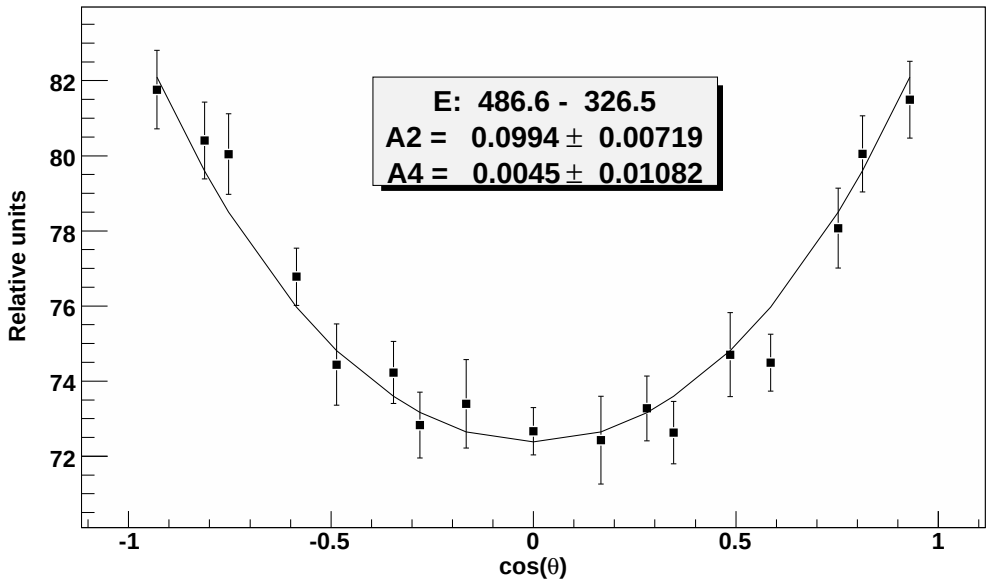

Figure 65: Angular correlation curve of 486.6 and 326.5 keV transitions in the ground-state band of ^{102}Zr.

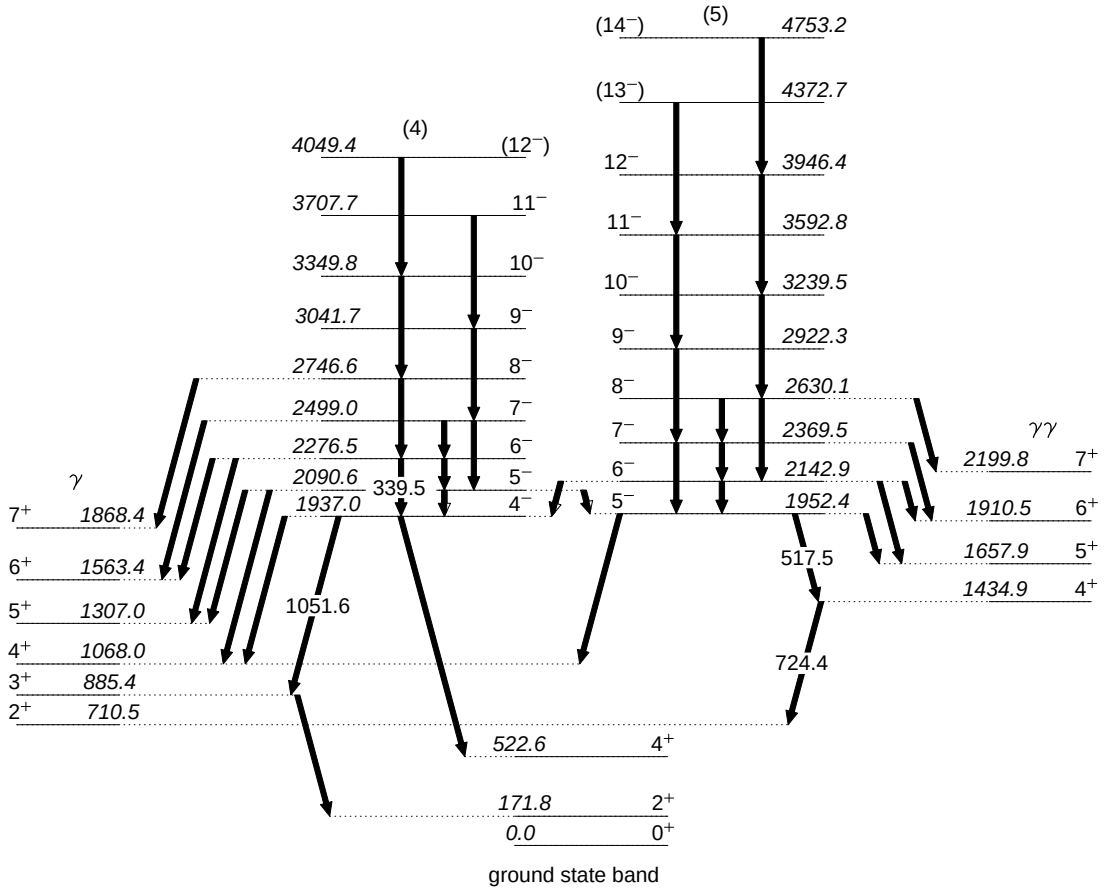

Figure 66: Partial level scheme of ^{106}Mo to show the decay patterns of chiral bands into γ and $\gamma\gamma$ bands.

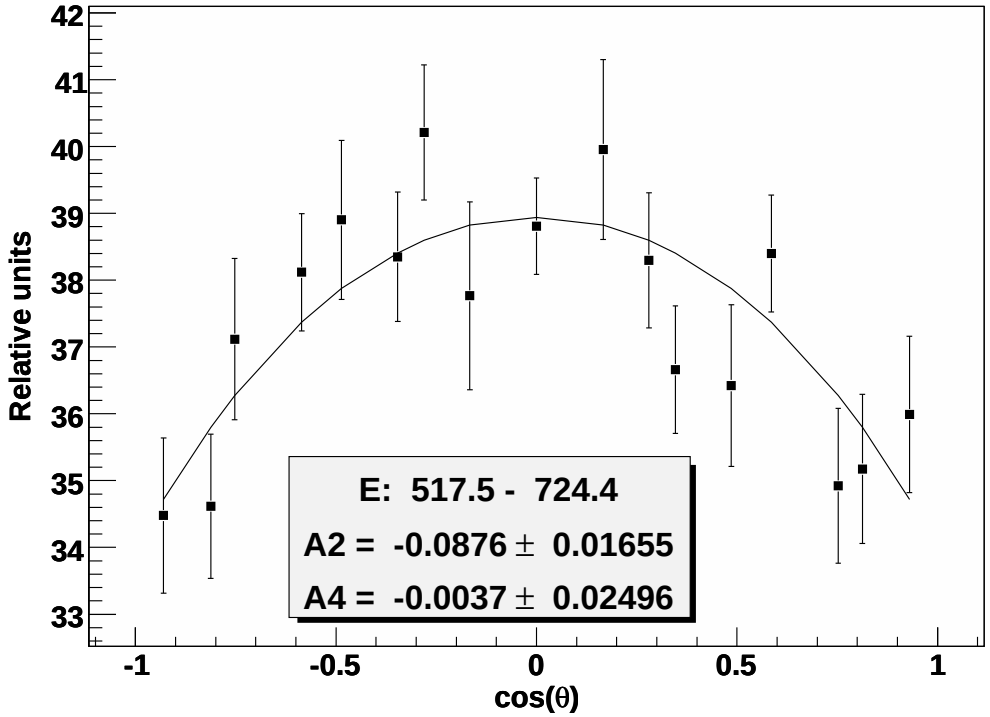

Figure 67: Angular correlations of 517.5 and 724.4 keV transitions in ^{106}Mo.

Compared with theoretical values, this result confirms the spin and parity of the 1952.4 keV state to be 5^-, since the 517.5-keV transition shows property of a dipole transition. Therefore, we have determined the spins and parities of states in band (5).

Angular correlation of the 339.5 – 1051.5 keV cascade has been measured as well, as shown in Figure 68. However, this cascade is relatively weaker, which leads to a result of $A_2^{exp} = -0.066(47)$, and $A_4^{exp} = -0.024(70)$. Different gating γ-rays were used to measure this angular correlation, and we have found that all yielded $A_2^{exp} \approx -0.07$ to -0.13 and $A_4^{exp} \approx 0$. This negative A_2^{exp} indicates the spin/parity of this cascade to be $6^-(Q)4^-(D)3^+$, to be consistent with the theoretical $A_2^{the} = -0.07$ and $A_4^{the} = 0$ for this kind of sequence. Attempts to assign other different spin/parity configurations would lead to disagreement between experimental and theoretical values.

The proposal of chiral vibrational bands for band (4) and in ^{106}Mo is also supported by theoretical calculations, which are not going to be discussed in this dissertation. Now with angular correlation measurements, we are more convinced that these bands are the

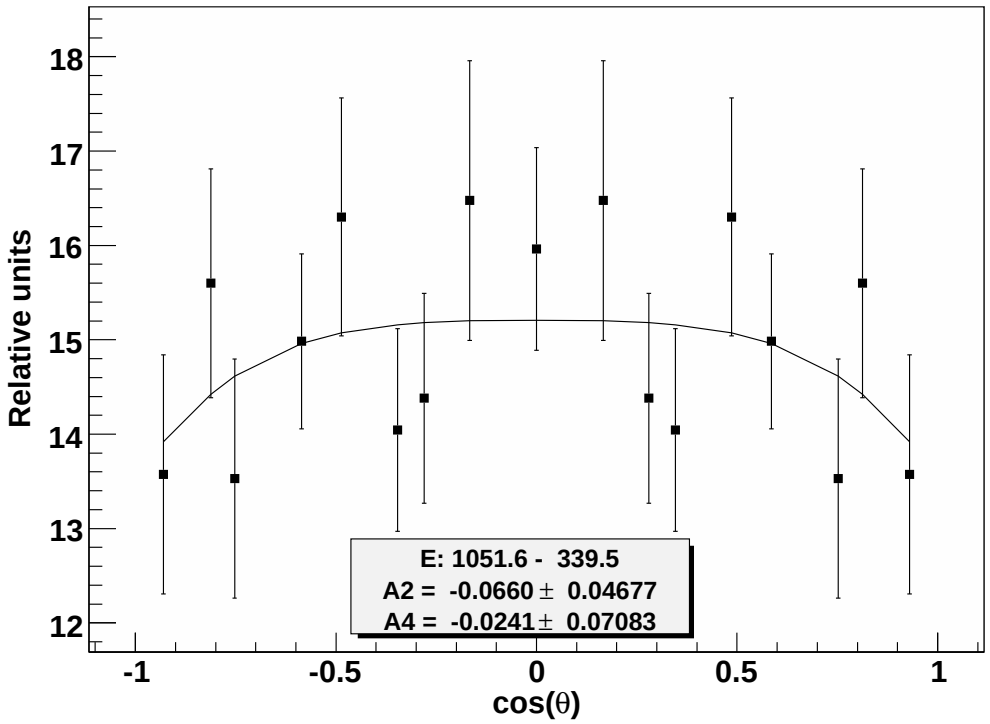

Figure 68: Angular correlations of 339.5 and 1051.2 keV transitions in ^{106}Mo.

first chiral vibrational bands in an even-even nucleus.

The g-factor Measurements

The g-factor values are extracted from measured delayed angular correlations , using techniques discussed above. These measurements were performed by scanning the November run experimental data. To increase the selectivity, matrices were created with additional γ gates. For each nucleus, different sets of gating γ-rays were compared to get a best selectivity. We assumed that the HFFs are those of an ion implanted in a substitutional site in the lattice [Rao79], shown in Figure 55. Lifetimes of the nuclei of interest were quoted in different references, most of which can be found on National Nuclear Data Center website.

From Equation 34, we have found out the solutions of the precession angles in the form of

$$\phi = \pm\sqrt{\frac{15 - 25G_2 \pm \sqrt{145 - 270G_2 + 45 * G_2^2}}{8(5G_2 - 1)}} \tag{46}$$

where G_2 is the attenuation factor. There are four solutions of ϕ. We take the rational positive solutions to calculate the average precession angles. Once the precession angle is determined, the magnitude of g-factor values are given by

$$|g| = \frac{\phi\hbar}{\mu_N B\tau} \tag{47}$$

The g-factor values of several 2^+ states in even-even neutron-rich nuclei from spontaneous fission of ^{252}Cf have been studied using the technique discussed above. In these data analysis, the gating γ-rays were selected carefully, to gain best statistics with least contaminations. Different gates were used to confirm the results.

The fitting results of delayed cascades in some even-even nuclei are listed in Figure 69, 70, 71, 72, 73, 74, 75, 76, 77, 78, 79, 80. Gating γ-rays for each case are listed in Table 8. As shown in Table 8, for most cases, transitions from the same cascades are enough to generate enough statistical data for angular correlation measurements. For the ^{102}Zr case, transitions from its partner isotopes were used.

Table 8: List of cascades and gating gamma-rays to measure g-factor values.

Nucleus	I^{π}	Cascade (keV)	Gating γ-rays (keV)
^{100}Zr	2^+	352.0–212.6	497.2, 625.4
^{102}Zr	2^+	326.5–151.8	486.6, 630.5 (^{102}Zr)
			158.5, 295.0, 386.2 (^{148}Ce)
			117.6, 283.5 (^{147}Ce)
			258.3, 409.7 (^{146}Ce)
^{104}Mo	2^+	368.6–192.4	519.4, 641.7
^{106}Mo	2^+	350.8–171.8	511.0, 654.9, 784.0
^{108}Mo	2^+	371.0–192.7	527.0, 662.1
^{108}Ru	2^+	422.3–242.1	574.6, 701.7
^{110}Ru	2^+	422.2–240.7	575.9, 705.4
^{112}Ru	2^+	408.4–236.6	544.9, 705.4
^{144}Ba	2^+	330.8–199.0	431.4, 509.3
^{146}Ba	2^+	332.6–181.3	444.6, 524.3
^{146}Ce	2^+	409.6–258.3	503.2, 565.2, 515.0
^{148}Ce	2^+	294.9–158.5	386.2, 450.8, 501.3

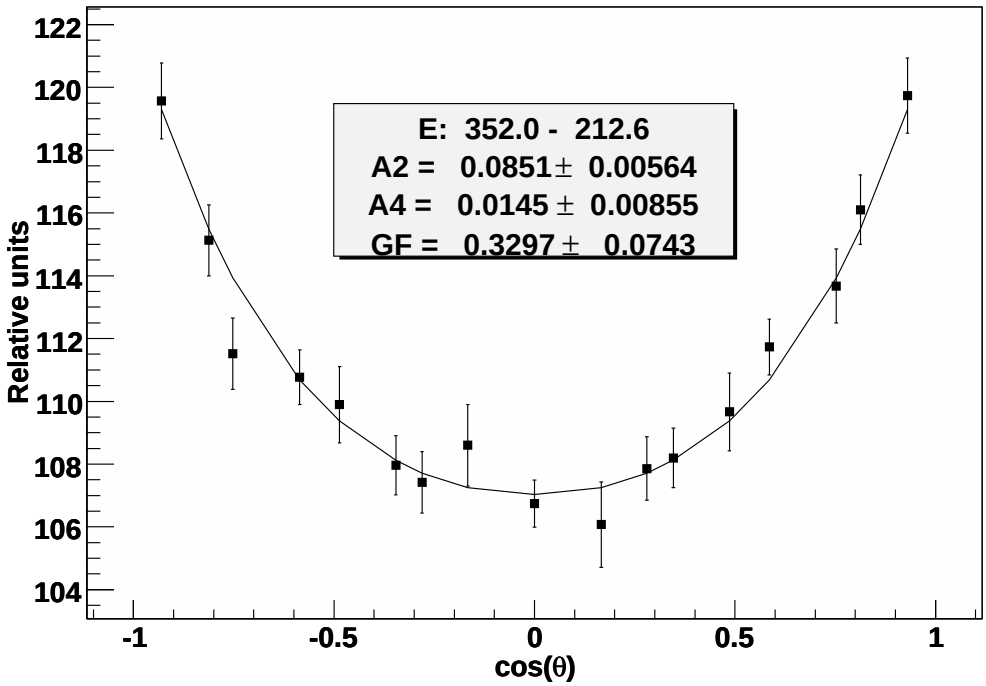

Figure 69: Angular correlations of 352.0-212.6 keV cascade in ^{100}Zr.

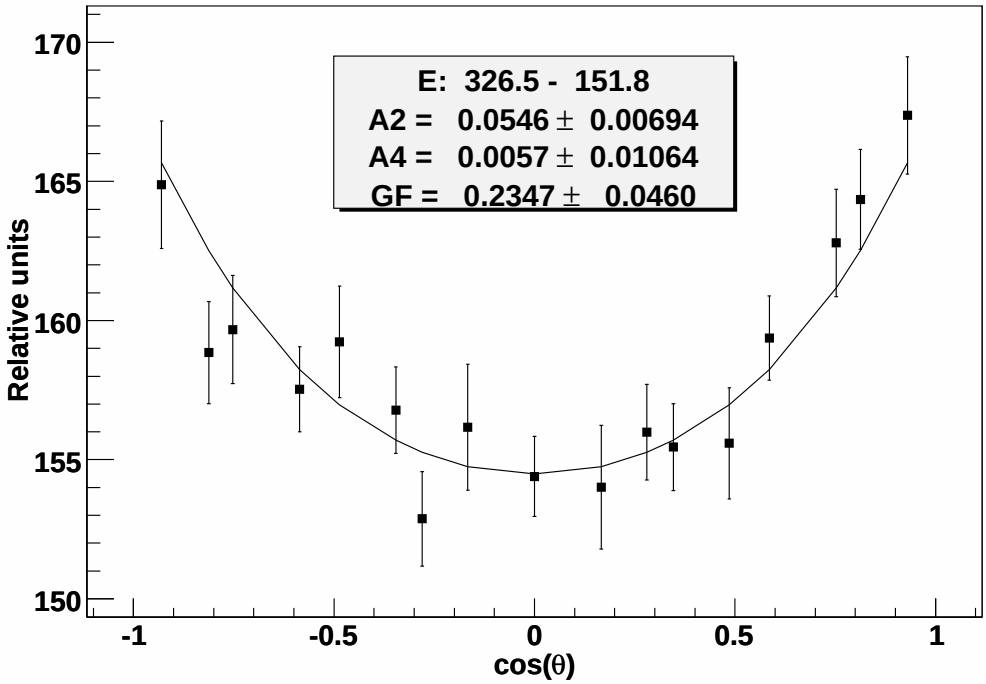

Figure 70: Angular correlations of 326.5- and 151.8-keV transitions in ^{102}Zr.

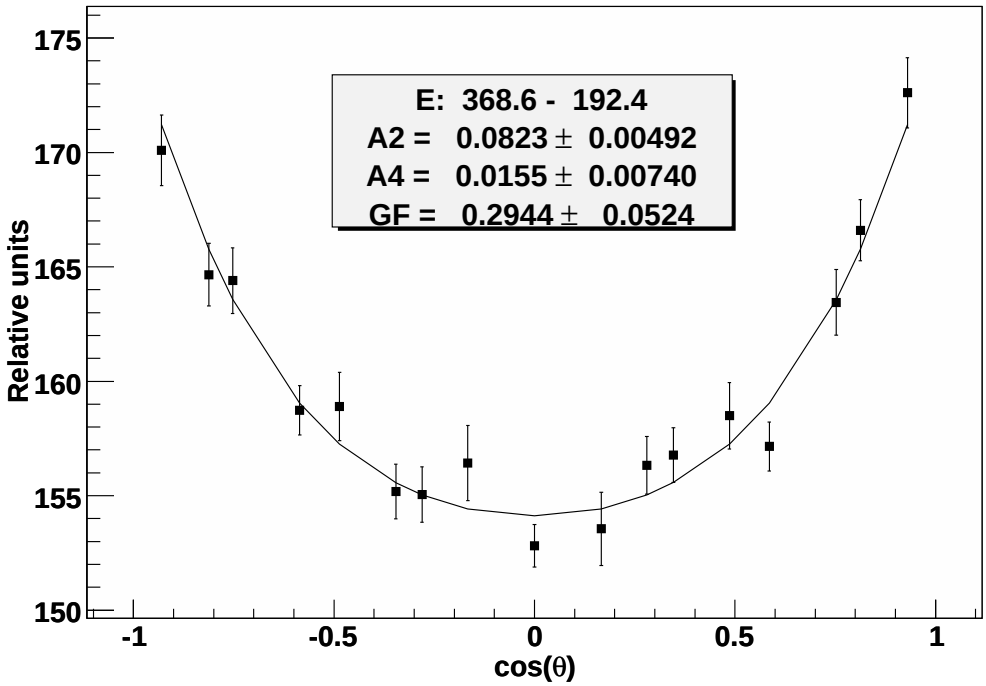

Figure 71: Angular correlations of 368.6- and 192.4-keV transitions in ^{104}Mo.

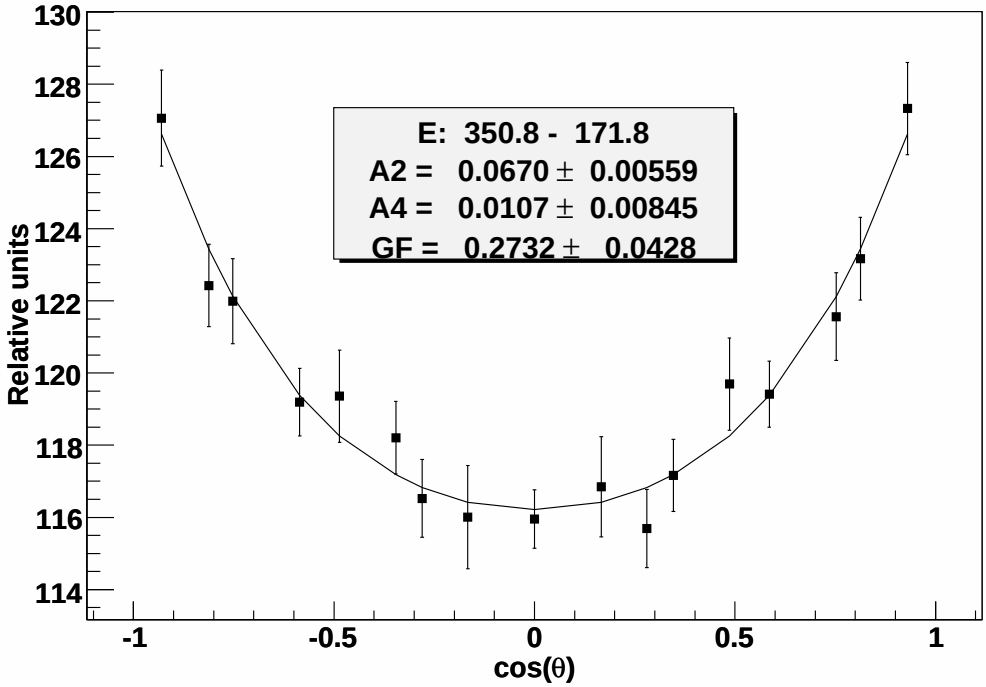

Figure 72: Angular correlations of 350.8- and 171.8-keV transitions in ^{106}Mo.

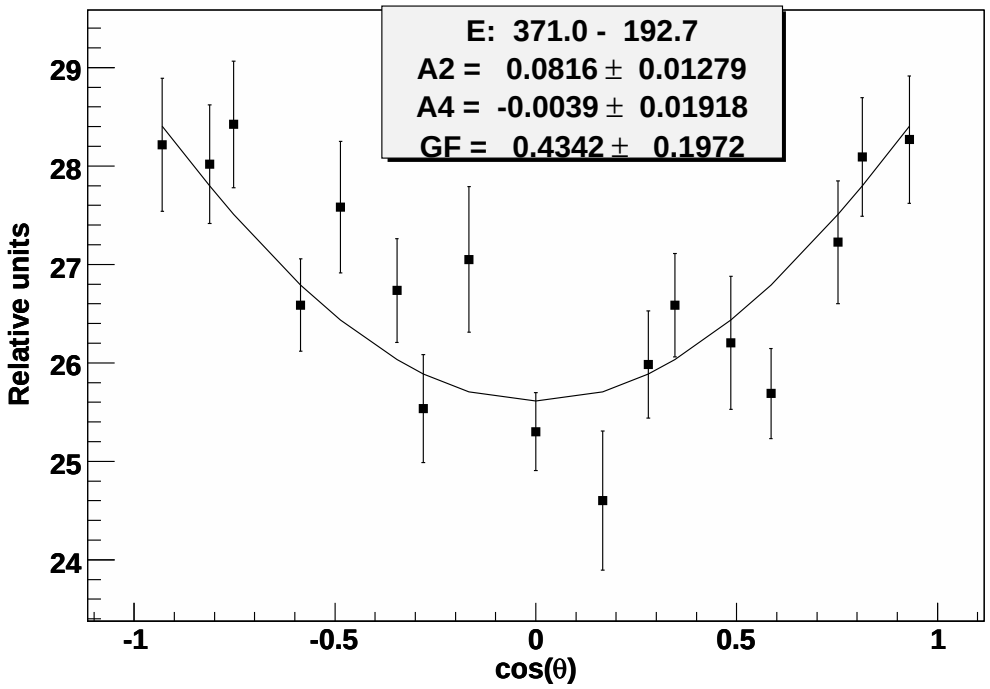

Figure 73: Angular correlations of 371.0- and 192.7-keV transitions in ^{108}Mo.

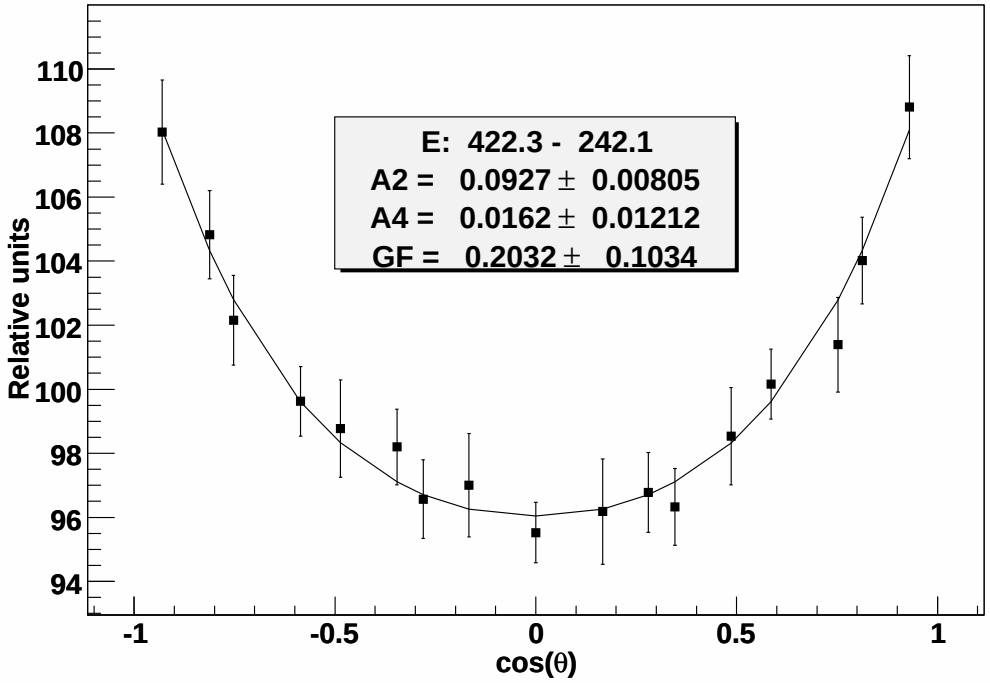

Figure 74: Angular correlations of 422.3- and 242.1-keV transitions in ^{108}Ru.

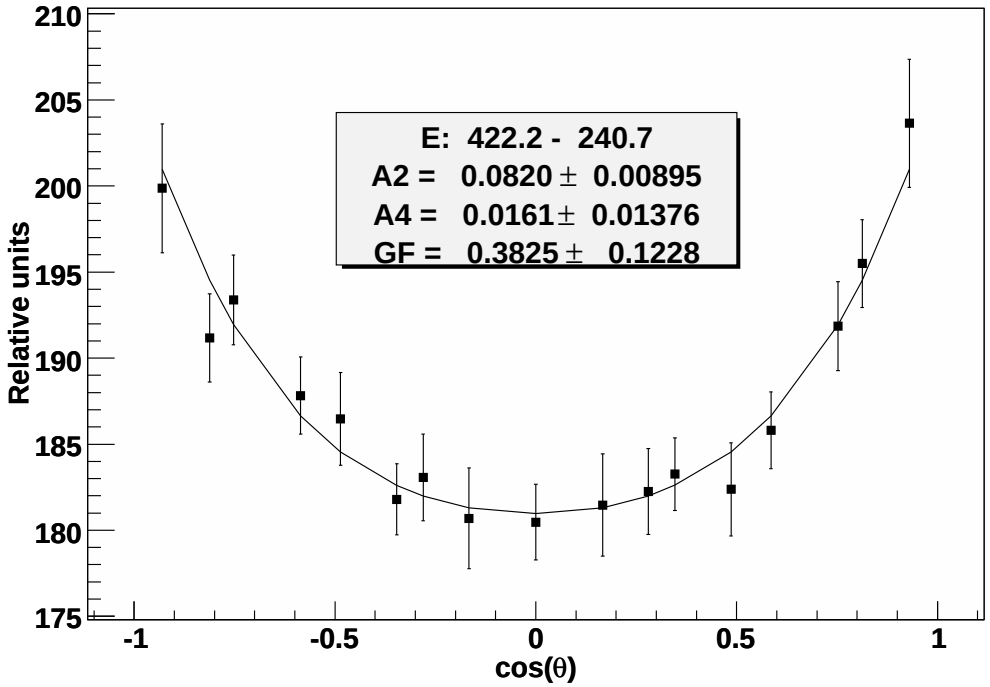

Figure 75: Angular correlations of 422.2- and 240.7-keV transitions in ^{110}Ru.

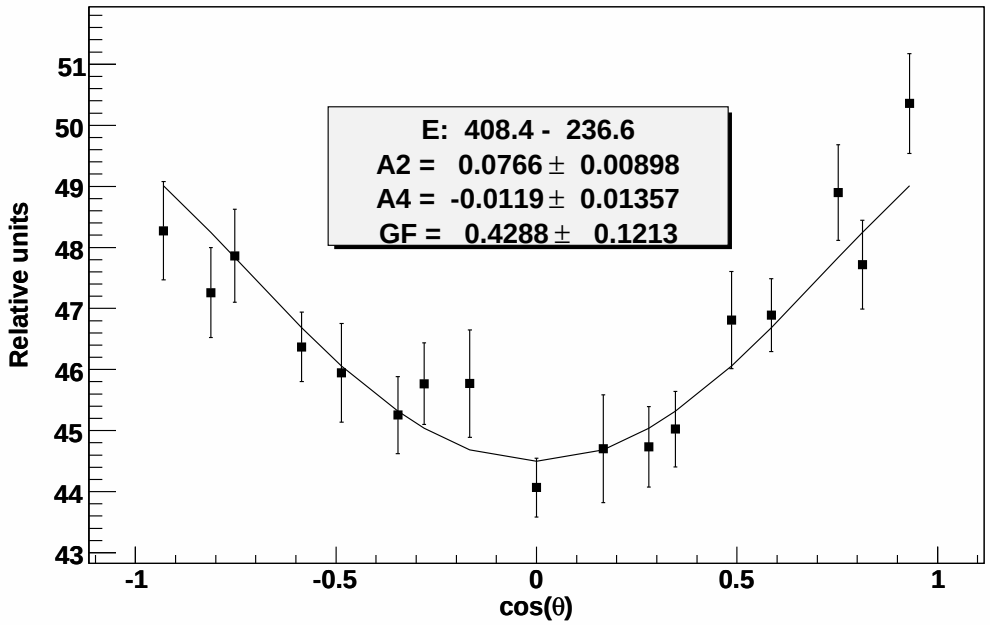

Figure 76: Angular correlations of 408.4- and 226.6-keV transitions in ^{112}Ru.

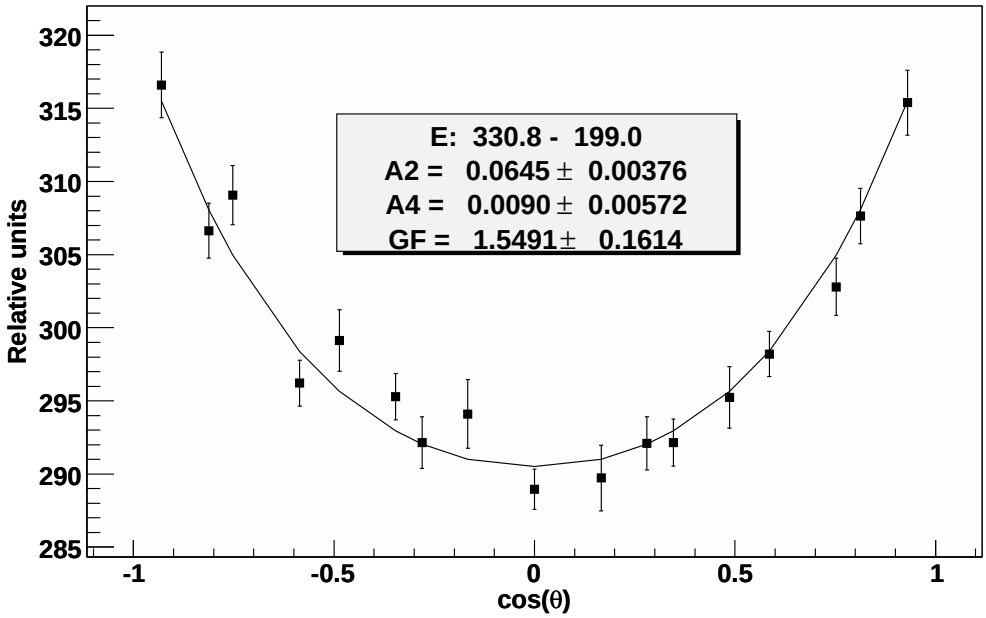

Figure 77: Angular correlations of 330.8- and 199.0-keV transitions in ^{144}Ba.

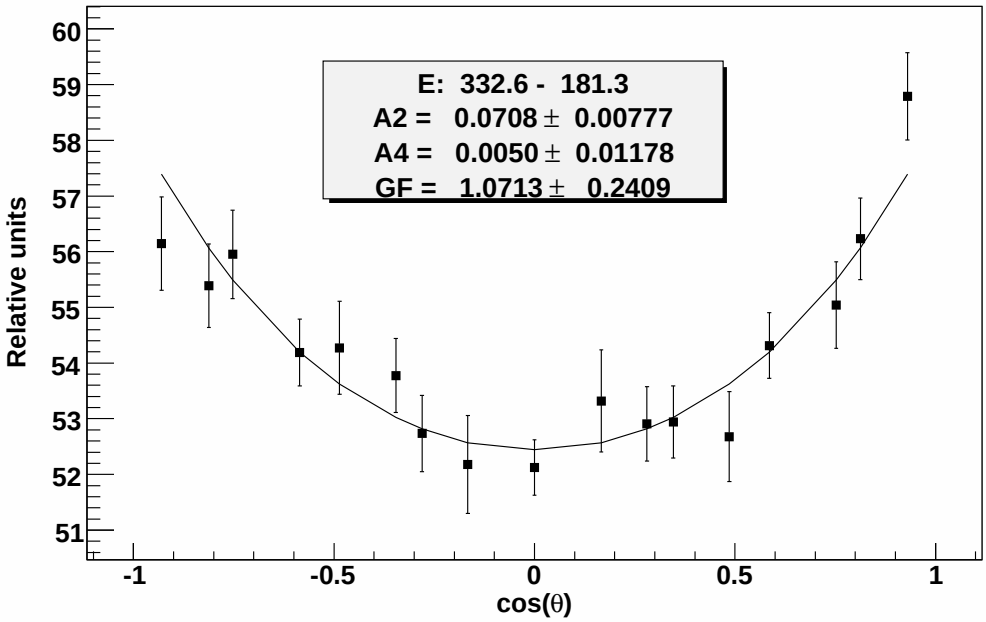

Figure 78: Angular correlations of 332.6- and 181.3-keV transitions in ^{146}Ba.

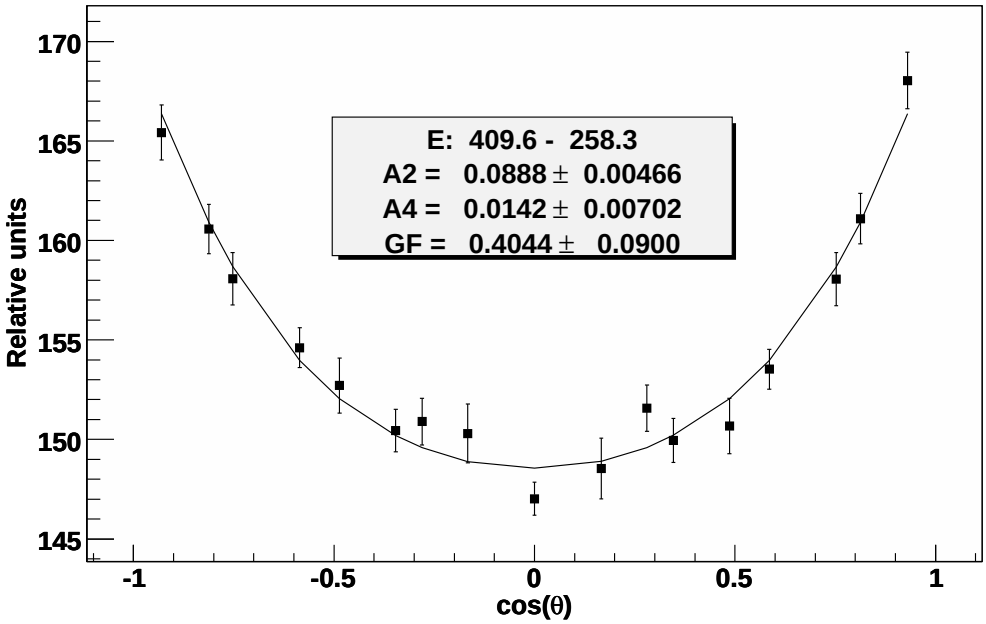

Figure 79: Angular correlations of 409.6- and 258.3-keV transitions in ^{146}Ce.

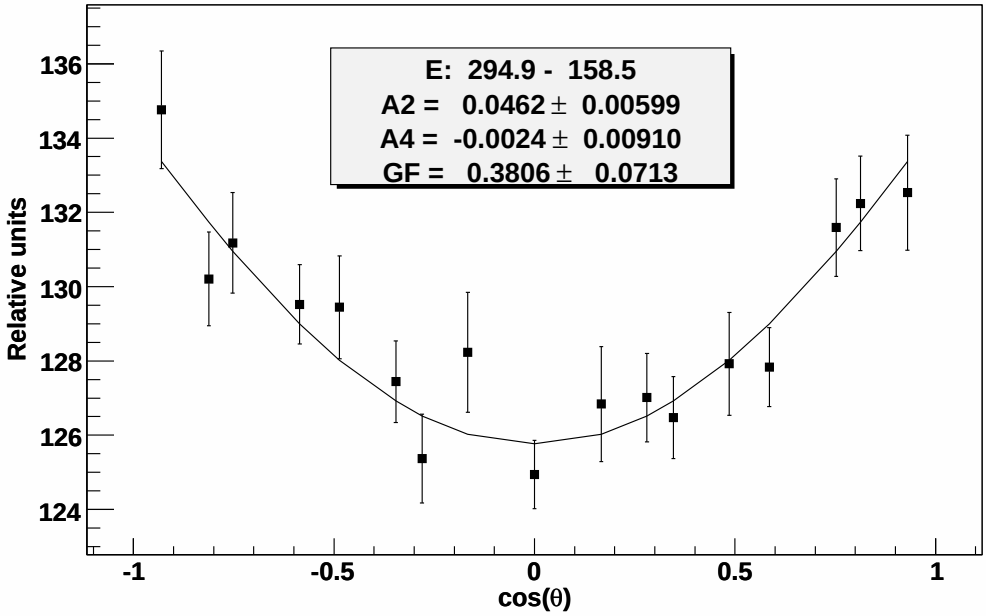

Figure 80: Angular correlations of 294.5- and 158.5-keV transitions in ^{148}Ce.

Table 9: Measured g-factors of excited states in neutron-rich nuclei produced from spontaneous fission of ^{252}Cf.

Nucleus	I(π)	τ (ns)	B (T)	g	g_{ref}
^{100}Zr	2^+	0.78(3)	27.4(4)	0.33(7)	0.30(3)[a] 0.26(6)[b]
^{102}Zr	2^+	2.76(36)	27.4(4)	0.23(5)	0.22(5)[a]
^{104}Mo	2^+	1.040(59)	25.6(1)	0.29(5)	0.27(2)[a]
^{106}Mo	2^+	1.803(43)	25.6(1)	0.27(4)	0.21(2)[a]
^{108}Mo	2^+	0.721(433)	25.6(1)	0.43(20)	0.5(3)[a]
^{108}Ru	2^+	0.498(43)	47.8(1)	0.20(10)	0.23(4)[a]
^{110}Ru	2^+	0.433(29)	47.8(1)	0.38(12)	0.44(7)[a]
^{112}Ru	2^+	0.462(43)	47.8(1)	0.43(12)	0.44(9)[a]
^{144}Ba	2^+	1.024(29)	8.5(14)	1.55(16)	0.34(5)[c] 0.34(5)[d]
^{146}Ba	2^+	1.241(43)	8.5(14)	1.07(24)	0.20(10)[c] 0.28(7)[d]
^{146}Ce	2^+	0.361(43)	41.0(2)	0.40(9)	0.46(34)[c] 0.24(5)[e]
^{148}Ce	2^+	1.457(87)	41.0(2)	0.38(7)	0.37(6)[c] 0.37(6)[e]

[a][Smi04] [b][Wol89] [c][Smi99] [d][Wol83] [e][Gil86]

From the perturbed angular correlation measurements, we are able to find out the precession angles. And if we have determined lifetimes of the excited states and hyperfine field strengths for these isotopes, we can solve out the g-factors from Equation 47. The measured g-factor values are tabulated in Table 9. Previously reported g-factor values are listed as well. The hyperfine field taken to calculate g-factors are same as [Smi04] and related references. We noticed a large discrepancy for Ba isotopes. This is an evidence that the hyperfine field for Barium implanted in iron might be quite different from that given in [Pat02] and [Smi04].

Discussion

Zr isotopes

For the measurement of the g-factor of the 2^+ state in ^{100}Zr, we took the lifetime as 0.78(3)ns [Fir96] and hyperfine field of Zr in iron as -27.4(4)T [Are79]. The measured $g(2^+)$ of ^{100}Zr, 034(7), is consistent with reported values [Wol89] [Smi04]. For ^{102}Zr, we took the lifetime of 2^+ state as 2.76(36) ns [Fir96] and the $g(2^+)$ is measured as 0.23(5), which is consistent with [Smi04]. A comparison of these measurements with previous measurements is plotted in Figure 81.

In A $\sim$ 100 region, Zr isotopes exhibit a subshell closure at $N = 56, 58$ [Ham95], with a sudden onset of deformation at $N = 60$. This is reflected in the ratios of the energies of the first 4^+ and 2^+ states, which are close to a rotating, charged object. As shown in Figure 81, the $g(2^+)$ values are close, but do not overlap the liquid-drop model prediction of Z/A, which are 0.40 and 0.39 for ^{100,102}Zr, respectively.

Wolf et al. [Wol89] interpreted the $g(2^+)$ values of $N = 60$ isotones, ^{98}Sr, ^{100}Zr and ^{102}Mo in terms of bother the hydrodynamic model and the IBA-2 model. They suggested that $N_\pi = 0$ for ^{100}Zr, which means that the $Z = 40$ sub-shell closure was still active for ^{100}Zr. Zhao et al. [Zha95] calculated the effective boson numbers, N_π and N_ν, according to experimental data on energy spectra and electromagnetic transitions probabilities. They found $N_\pi = 1$, $N_\nu = 4$ for ^{98}Zr but $N_\pi = 3$, $N_\nu = 5, 6$ for ^{100,102}Zr. The conclusion was that the $Z = 40$ sub-shell closure was destroyed at $N = 60$. This is due to the transition from spherical to deformed shapes around $N = 60$ for Zr isotopes.

Mo isotopes

As shown in Figure 82, the measured g-factor values of 2^+ states in ^{104,106,108}Mo isotopes are in excellent agreement with previous measurements [Smi04]. Located above the $Z = 40$ and N = 56, 58 sub-shell closures, and at the middle of major shells, we would

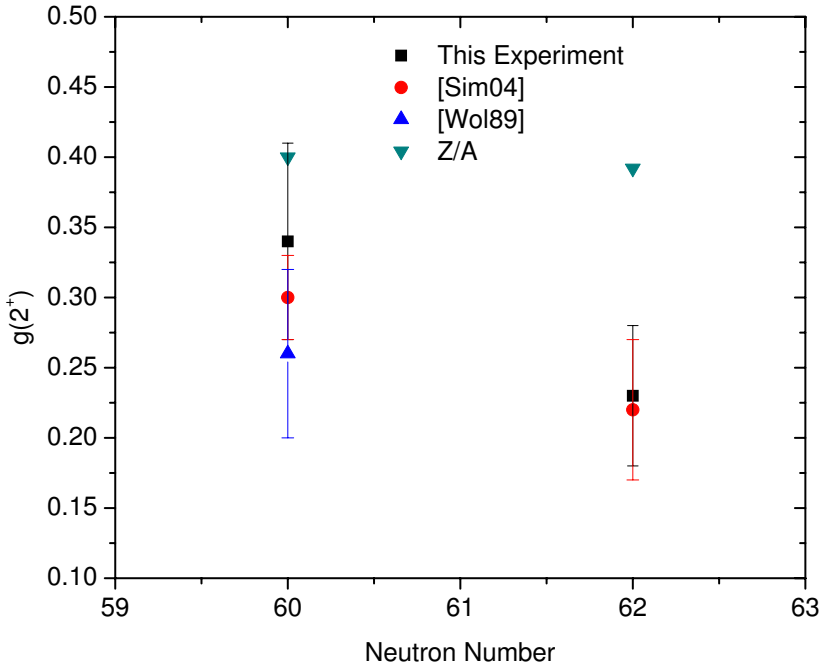

Figure 81: Measured $g(2^+)$ in Zr nuclei in this experiment, with comparison of previous data and Z/A.

expect collective properties in these nuclei, with g-factors of 2^+ states approaching Z/A. However, the measured $g(2^+)$ in ^{104,106}Mo are apparently lower than Z/A. And at $N = 64$, the sub-shell closure seems to be very significant for neutron-rich Mo isotopes. These Mo nuclei are widely accepted as γ-soft rotors, which are not quite fully collective rotational nuclei. Another explanation for this fall in $g(2^+)$ is contributions from the $h_{11/2}$ intruder orbital [Smi04].

Ru isotopes

The measured 2^+ state g-factors for Ru isotopes are plotted in Figure 83. The new measurements are in good agreement with previous results [Smi04]. We have confirmed that the $g(2^+)$ drop at the $N = 64$ sub-shell closure, as well as observed in Mo isotopes.

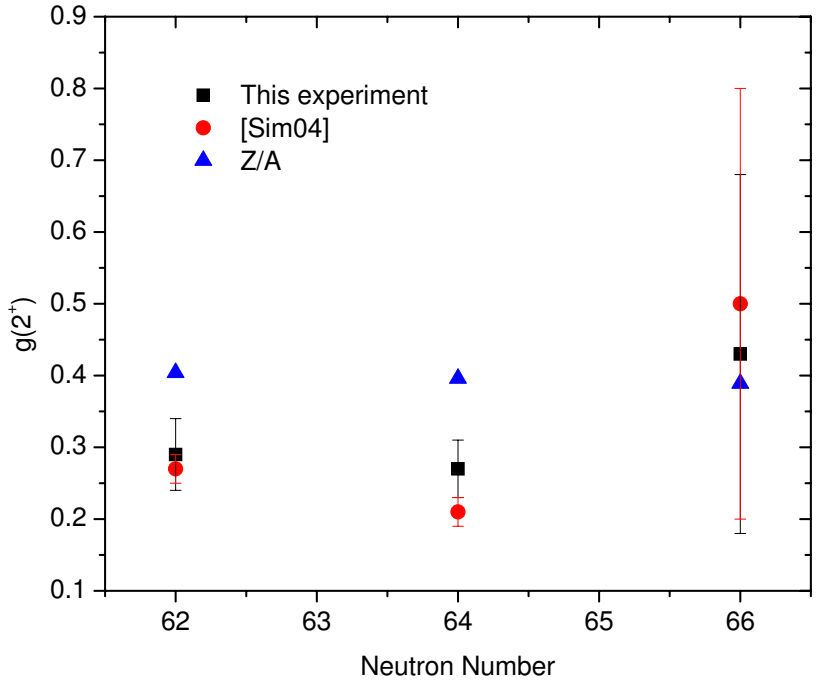

Figure 82: Measured $g(2^+)$ in Mo nuclei in this experiment, with comparison of previous data and Z/A.

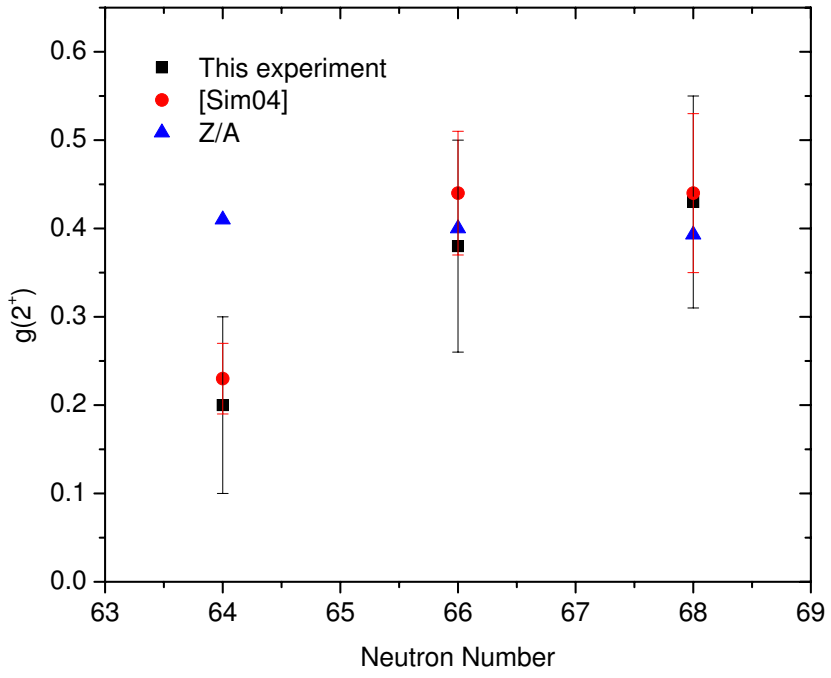

Figure 83: Measured $g(2^+)$ in Ru nuclei in this experiment, with comparison of previous data and Z/A.

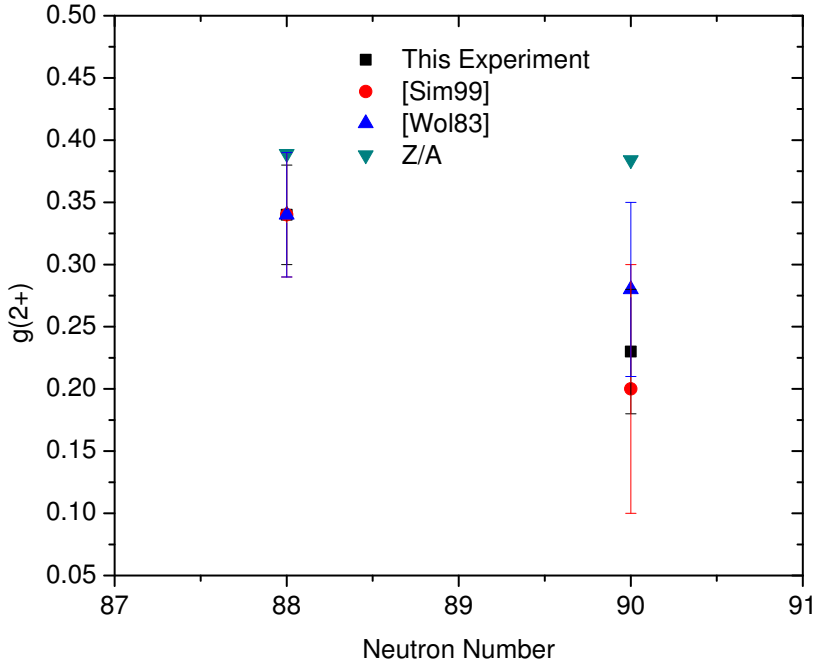

Figure 84: Measured $g(2^+)$ in Ba nuclei in this experiment, with comparison of previous data and Z/A.

Ba isotopes

As shown in Table 9, the measured 2^+-state g-factors for ^{144,146}Ba are about 5 times larger than reported values in [Wol83] and [Smi99]. The impurity hyperfine field for Barium in iron was measured to be 8.5T [Kug70] [Rao79]. This value is used to measure g-factors in [Smi04]. Since this technique has been approved by several measurements, the only explanation is that the hyperfine field for Barium in iron is much larger than it was taken. Both [Wol83] and [Smi99] measured the 2^+-state g-factor of ^{144}Ba to be 0.34(5). Therefore, this value is used to calibrate our data, with the 2^+-state g-factors of ^{144,146}Ba to be 0.34(4) and 0.23(5). The corrected g-factor of ^{146}Ba agrees well with previous measurements in [Wol83] and [Smi99]. A comparison of these results is shown in Figure 84. The hyperfine field for Ba in iron becomes $\sim$38.8T. These results raise questions for future theoretical and experimental work.

In Wolf et al's work [Wol83], they combined $g(2^+)$ of ^{144,146}Ba with neighboring

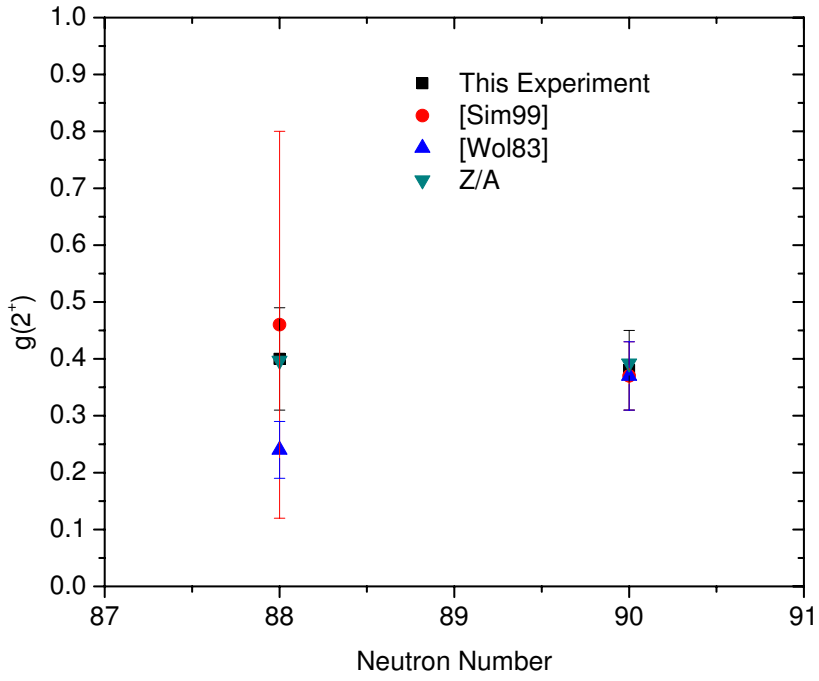

Figure 85: Measured $g(2^+)$ in Ce nuclei in this experiment, with comparison of previous data and Z/A.

Nd, Sm and Gd isotopes in order to investigate the IBM model in this region. They deduced that $g_\pi = +0.76(10)$ and $g_\nu = +0.20(11)$ only after allowing for a sharp change in N_π at $N = 90$. This change is due to the $Z = 64$ sub-shell closure at $N = 90$. But Barium isotopes are closer to the $Z = 50$ shell closure, with no affect from the $Z = 64$ sub-shell closure effect.

Ce isotopes

The measurements of 2^+-state g-factors of ^{146,148}Ce are in good agreement with previous results. Our data for ^{146}Ce is more close to [Smi04], as plotted in Figure 85. Our data agree perfectly with collective model predictions, since the even-even Cerium isotopes undergo a transition from vibrational to rotational-like structure as the number of neutrons change from $N = 86$ to 92 [Cas81]. This transition is attributed to neutron-proton interaction between spin-orbit partner states, which causes protons to occupy the

$h_{11/2}$ orbitals when the $h_{9/2}$ neutron orbit begins to be filled near $N = 90$. The resulting $\pi h_{11/2} - \nu h_{9/2}$ interaction induces a rapid onset of deformation, similar to the situation in the $A \sim 100$ region.

In Gill *et al.*'s work, they fit with the IBA-2 model with $g_\pi = -0.64 \pm 0.04$ and $g_\nu = 0.05 \pm 0.05$. They assumed N_ν = 3 and 4 for ^{146}Ce and ^{148}Ce, respectively and obtained $N_\pi^{eff} = 1.5 \pm 0.6$ for ^{146}Ce and $N_\pi^{eff} = 4.9 \pm 2.1$ for ^{148}Ce. These values are consistent with Casten *et al.* [Cas81], who proposed the abrupt eradication of the $Z = 64$ sub-shell for N $\geq$ 90.

Conclusion

In this chapter, we introduced the theoretical background, technical details and recent results to measure γ-ray angular correlations and g-factors in neutron-rich nuclei produced from the spontaneous fission of ^{252}Cf. The theoretical prediction of nuclear g-factors from different nuclear models were given. The angular correlation theory was described. For the measurement of g-factors, perturbed angular correlation techniques were introduced. The angular properties, response functions and relative efficiencies of Gammasphere detectors were investigated in details. The technique to increment and fit angular correlation matrices were described.

The angular correlations of two prompt cascades in the chiral bands of ^{106}Mo were investigated. The measured angular correlation coefficients supported the proposed spin and parity assignments. The 2^+-state g-factors in several neutron-rich nuclei, ^{100,120}Zr, ^{104,106,108}Mo, ^{108,110,112}Ru, ^{144,146}Ba, and ^{146,148}Ce, were measured. For Zr, Mo, Ru, and Ce isotopes, the measured 2^+-state g-factors are consistent with previous data. For Ba isotopes, the g-factors were calibrated, and a new value of the impurity hyperfine field for Ba isotopes in Fe host was proposed. The measured g-factors were compared with collective model predictions as well as other nuclear models.

CHAPTER V

SUMMARY

This dissertation is mainly based on 2000 binary fission experimental data. With the Gammasphere detector array, we accumulated a large amount of data for detailed nuclear structure analysis, γ-ray angular correlation measurements and g-factor measurements.

By analyzing our 2000 binary fission data, structure of several neutron-rich nuclei were studied. The level scheme of ^{88}Kr was extended to a 7169.4-keV state, spins and parities were assigned by following the level systematics in the $N = 52$ isotones, ^{86}Se and ^{90}Sr. The level scheme of ^{90}Kr was extended, with several new transitions and states identified. Angular correlation measurements confirmed the 3^- assignment to the 1506.7-keV level in ^{90}Kr, in agreement with reported data. The lack of systematics in the $N = 54$ isotones, ^{90}Kr and ^{92}Sr, provides insight into this region and indicates the requirement of further experimental and theoretical investigation. A few new transitions were observed in ^{92}Kr as well. No new transition or state was identified in ^{94}Kr, due to its low yield. In ^{102}Zr, three new collective band structures were identified. Angular correlation measurements were performed to assign spins and parities. In the neutron-rich ^{114}Ru, the ground-state band and γ-band were extended. A new band was identified and proposed as a two-phonon γ-band, by comparing band-head energies with its neighboring even-even Ru isotopes. Cranked Shell Model calculations indicate that the band-crossing of ground-state band in ^{114}Ru is from alignment of two $g_{9/2}$ protons, instead of alignment of two $h_{11/2}$ neutrons as found in $^{108-112}$Ru. The staggering pattern of the γ-band indicates a rigid triaxial shape in ^{114}Ru. The level scheme of ^{138}Cs was constructed for the first time in this work, with that of ^{137}Cs extended with several new transitions. Spins, parities and configurations were assigned to the levels of ^{138}Cs based on total internal conversion coefficient measurements of the low-energy transitions, shell-model calculations, angular correlation measurements

and level systematics. Shell Model calculations were performed with results in agreement with experimental data. Similarities were observed for the $N = 82$ isotones, ^{137}Cs and ^{135}I as well as the $N = 83$ isotones, ^{138}Cs and ^{136}I. The Shell-Model calculations indicate the important role played by the coupling between the excitation of the fifth proton outside the $Z = 50$ major shell and the $f_{7/2}$ neutron outside the $N = 82$ major shell.

In our 2000 binary fission experiment, the ^{252}Cf source was sandwiched between Fe foils. For prompt cascades, we are able to measure angular correlations. The comparison between the measured angular correlation coefficients with theoretical values help us to assign spin/parity configurations. The angular correlations of two prompt cascades in the chiral bands of ^{106}Mo were investigated. The measured angular correlation coefficients supported the proposed spin and parity assignments. For delayed cascades, γ-ray angular correlations are perturbed, which is described by the attenuation factors. The attenuation factors are used to extract the g-factors of the intermediate state. By measuring perturbed angular correlations, the 2^+-state g-factors of several neutron-rich nuclei, ^{100,120}Zr, ^{104,106,108}Mo, ^{108,110,112}Ru, ^{144,146}Ba, and ^{146,148}Ce, were measured. For Zr, Mo, Ru, and Ce isotopes, the measured 2^+-state g-factors are consistent with previous data. For Ba isotopes, the g-factors were calibrated, and a new value of the impurity hyperfine field for Ba isotopes in Fe host was proposed. The measured g-factors were compared with collective model predictions as well as other nuclear models.

BIBLIOGRAPHY

[Are79] Arends, A. R. and Pleiter, F., *Hyp. Int.*, vol. 7(1), (1979) 361.

[Ari75] Arima, A. and Iachello, F., *Phys. Rev. Lett.*, vol. 35(16), (1975) 1069.

[Bha97] Bhattacharyya, P., Zhang, C. T., Fornal, B. *et al.*, *Phys. Rev. C*, vol. 56(5), (1997) R2363.

[Bro99] Broda, R., Fornal, B., Daly, P. J. *et al.*, *Phys. Rev. C*, vol. 59(6), (1999) 3071.

[Car74] Carlson, G. H., Talbert, W. L., and McConnell, J. R., *Phys. Rev. C*, vol. 9(1), (1974) 283.

[Cas81] Casten, R. F., Warner, D. D., Brenner, D. S. *et al.*, *Phys. Rev. Lett.*, vol. 47(20), (1981) 1433.

[Che70] Cheifetz, E., Jared, R., Thompson, S. *et al.*, *Phys. Rev. Lett*, vol. 25, (1970) 38.

[Che04] Che, X., Zhu, S., Hamilton, J. *et al.*, *Chin. Phys. Lett*, vol. 21, (2004) 1904.

[Che06] Che, X., Zhu, S., Hamilton, J. *et al.*, *Chin. Phys. Lett*, vol. 23, (2006) 328.

[Cor05] Coraggio, L., Covello, A., Gargano, A. *et al.*, *Phys. Rev. C*, vol. 72, (2005) 057302.

[Cor06] Coraggio, L., Covello, A., Gargano, A. *et al.*, *Phys. Rev. C*, vol. 73, (2006) 031302.

[Cov07] Covello, A., Coraggioa, L., Gargano, A. *et al.*, *Prog. Part. Nucl. Phys.*, vol. 59, (2007) 401.

[Dal99] Daly, P., Bhattacharyya, P., Zhang, C. T. *et al.*, *Phys. Rev. C*, vol. 59(6), (1999) 3066.

[Dan07] Daniel, A. V., Goodin, C., Li, K. *et al.*, *Nucl. Instrum. Methods Phys. Res. B*, vol. 262, (2007) 399.

[Dev96] Devi, R. and Khosa, S., *Phys. Rev. C*, vol. 54, (1996) 1661.

[Dur95] Durell, J., Phillips, W., Pearson, C. *et al.*, *Phys. Rev. C*, vol. 52, (1995) R2306.

[Fir96] Firestone, R. and Shirley, V., *Table of Isotopes, 8th ed.* (Wiley, 1996).

[Fon06] Fong, D., Hamilton, J. H., Ramayya, A. V. *et al.*, *Physics of Atomic Nuclei*, vol. 69(7), (2006) 1161.

[For01] Fornal, B., Broda, R., Daly, P. J. *et al.*, *Phys. Rev. C*, vol. 63(2), (2001) 024322.

[Gil86] Gill, R. L., Warner, D. D., Mach, H. *et al.*, *Phys. Rev. C*, vol. 33(3), (1986) 1030.

[Goo06] Goodin, C., Fong, D., Hwang, J. K. *et al.*, *Phys. Rev. C*, vol. 74(1), (2006) 017309.

[Gre66] Greiner, W., *Nucl. Phys.*, vol. 80, (1966) 417.

[Ham75] Hamilton, W., *The Electromagnetic Interaction in Nuclear Spectroscopy* (North-Holland, 1975).

[Ham89] Hamilton, J., *Treatise on Heavy-ion Science* (Plenum Publishing Corp., 1989), vol. 8, chap. 1, 3–98.

[Ham95] Hamilton, J., Ramayya, A., Zhu, S. *et al.*, *Prog. Part. Nucl. Phys.*, vol. 35, (1995) 635.

[Hil91] Hill, J. C., Schwellenbach, D., Wohn, F. *et al.*, *Phys. Rev. C*, vol. 43, (1991) 2591.

[Hot91] Hotchkis, M., Durell, J., Fitzgerald, J. *et al.*, *Nucl. Phys. A*, vol. 530, (1991) 111.

[Hua04] Hua, H., Wu, C., Cline, D. *et al.*, *Phys. Rev. C*, vol. 69, (2004) 014317.

[Hwa06a] Hwang, J., Ramayya, A., Hamilton, J. *et al.*, *Phys. Rev. C*, vol. 73, (2006) 044216.

[Hwa06b] Hwang, J., Ramayya, A., Hamilton, J. *et al.*, *Phys. Rev. C*, vol. 74, (2006) 017303.

[Jia03] Jiang, Z., Zhu, S., Hamilton, J. *et al.*, *Chin. Phys. Lett*, vol. 20, (2003) 350.

[Jon06] Jones, E. F., Gore, P. M., Hamilton, J. H. *et al.*, *Phys. Rev. C*, vol. 73, (2006) 017301.

[Kug70] Kugel, H. W., Polga, T., Kalish, R. *et al.*, *Phys. Lett. B*, vol. 32, (1970) 463.

[Law74] Lawson, C. and Hanson, R., *Solving Least Square Problems* (Prentice-Hall, 1974).

[LCC71] L. C. Carraz, E. M. and Moussa, A., *Nucl. Phys. A*, vol. 171, (1971) 209.

[Lee97] Lee, I. Y., *Prog. Part. Nucl. Phys.*, vol. 38, (1997) 65.

[Lhe01] Lhersonneau, G., Pfeiffer, B., Gabelmann, H. *et al.*, *Phys. Rev. C*, vol. 63, (2001) 054301.

[Luo01] Luo, Y., Rasmussen, J., Ramayya, A. *et al.*, *Phys. Rev. C*, vol. 64(5), (2001) 054306.

[Luo02] Luo, Y., Rasmussen, J., Hamilton, J. *et al.*, in *Proceedings of the Third International Conference: Fission and Properties of Neutron-rich Nuclei*, edited by Hamilton, J., Ramayya, A., and Carter, H. (2002), 310.

[Luo04] Luo, Y., Rasmussen, J. O., Hamilton, J. H. *et al.*, *Phys. Rev. C*, vol. 70(4), (2004) 044310.

[Luo05] Luo, Y., Rasmussen, J., and Stefanescu, I., *J. Phys. G: Nucl. Part. Phys.*, vol. 31.

[Luo06] Luo, Y., Hamilton, J. H., Rasmussen, J. O. *et al.*, *Phys. Rev. C*, vol. 74(2), (2006) 024308.

[Luo08] Luo, Y., Zhu, S., and Hamilton, J., *Euro. Phys. J. A. submitted*.

[Mac01] Machleidt, R., *Phys. Rev. C*, vol. 63(2), (2001) 024001.

[Mat65] Matthias, E., Rosenblum, S., and Shirley, D., *Phys. Rev. Lett*, vol. 14, (1965) 46.

[May55] Mayer, M. and Jensen, J., *Elementary Theory of Nuclear Shell Structure* (John Wiley and Sons, Inc., 1955).

[Mol95] Moller, P., Nix, J. R., Myers, W. D. *et al.*, *At. Data and Nuc. Data Tab.*, vol. 59, (1995) 185.

[Pat02] Patel, D., Smith, A., Simpson, G. *et al.*, *J. Phys. G: Nucl. Part. Phys.*, vol. 28, (2002) 649.

[Pra87] Prade, H., Enghardt, W., Dioszegi, I. *et al.*, *Nucl. Phys. A*, vol. 65(1472), (1987) 381.

[Rac51] Racah, G., *Phys. Rev.*, vol. 82, (1951) 309.

[Rad95] Radford, D., *Nucl. Instrum. Methods Phys. Res. A*, vol. 361, (1995) 297.

[Rao79] Rao, G., *Hyperfine Interactions*, vol. 7, (1979) 141.

[RU00] Rzaca-Urban, T., Urban, W., Kaczor, A. *et al.*, *Eur. Phys. J. A*, vol. 9, (2000) 165.

[Sah01] Saha, S. K., Constantinescu, C., Daly, P. J. *et al.*, *Phys. Rev. C*, vol. 65(1), (2001) 017302.

[Sam84] Sambataro, M., Scholten, O., Dieperink, A. E. L. *et al.*, *Nucl. Phys. A*, vol. 423, (1984) 333.

[Sch37] Schmidt, T., *Z. Phys.*, vol. 106, (1937) 358.

[Sha94] Shannon, J., Phillips, W., Durell, J. *et al.*, *Phys. Lett. B*, vol. 334, (1994) 136.

[Sie65] Siegbahn, K., *Apha-, Beta- and Gamma-ray Spectroscopy* (North-Holland, 1965).

[Smi99] Smith, A., Simpson, G., Billows, J. *et al.*, *Phys. Lett. B*, vol. 453, (1999) 206.

[Smi04] Smith, A., Patel, D., Simpson, G. *et al.*, *Phys. Lett. B*, vol. 591, (2004) 55.

[Ste01] Stefanova, E. A., Schwengner, R., Rainovski, G. *et al.*, *Phys. Rev. C*, vol. 63(6), (2001) 064315.

[Ste02] Stefanova, E. A., Danchev, M., Schwengner, R. *et al.*, *Phys. Rev. C*, vol. 65(3), (2002) 034323.

[Stu01] Stuchbery, A. E., *Nucl. Phys. A*, vol. 682, (2001) 470c.

[TA97] Ter-Akopian, G. M., Hamilton, J. H., Oganessian, Y. T. *et al.*, *Phys. Rev. C*, vol. 55(3), (1997) 1146.

[Tay71] Taylor, H., Singh, B., Prato, F. *et al.*, *Nuclear Data Tables*, vol. A9, (1971) 1.

[Urb01] Urban, W., Durell, J., Smith, A. *et al.*, *Nucl. Phys. A*, vol. 689, (2001) 605.

[Urb05] Urban, W., Rzaca-Urban, T., Durell, J. L. *et al.*, *Eur. Phys. J. A*, vol. 24, (2005) 161.

[Urb06] Urban, W., Sarkar, M. S., Sarkar, S. *et al.*, *Eur. Phys. J. A*, vol. 27, (2006) 257.

[Wah88] Wahl, A., *At. Data and Nuc. Data Tab.*, vol. 39, (1988) 1.

[Wol83] Wolf, A., Berant, Z., Warner, D. D. *et al.*, *Phys. Lett. B*, vol. 123, (1983) 165.

[Wol89] Wolf, A., Sistemich, K., Mach, H. *et al.*, *Phys. Rev. C*, vol. 40(2), (1989) 932.

[Zha95] Zhao, Y. M. and Chen, Y., *Phys. Rev. C*, vol. 52(3), (1995) 1453.

[Zha96] Zhang, C. T., Bhattacharyya, P., Daly, P. J. *et al.*, *Phys. Rev. Lett.*, vol. 77(18), (1996) 3743.

[Zha01] Zhang, X., *High Spin Studies of Neutron-rich Nuclei Produced in Spontaneous Fission of* ^{252}*Cf*, Ph.D. thesis, Vanderbilt University (2001).

[Zhu08] Zhu, S., Luo, Y., and Hamilton, J., *Euro. Phys. J. A. submitted*.